CNWRA 2003-06

MECHFAIL: A TOTAL-SYSTEM PERFORMANCE ASSESSMENT CODE MODULE FOR EVALUATING ENGINEERED BARRIER PERFORMANCE UNDER MECHANICAL LOADING CONDITIONS

Prepared for

U.S. Nuclear Regulatory Commission
Contract NRC-02-02-012

Prepared by

Center for Nuclear Waste Regulatory Analyses
San Antonio, Texas

May 2003

CNWRA 2003–06

MECHFAIL: A TOTAL-SYSTEM PERFORMANCE ASSESSMENT CODE MODULE FOR EVALUATING ENGINEERED BARRIER PERFORMANCE UNDER MECHANICAL LOADING CONDITIONS

Prepared for

U.S. Nuclear Regulatory Commission
Contract NRC–02–02–012

Prepared by

G. Douglas Gute, Goodluck Ofoegbu, Fernand Thomassy, Sui-Min Hsiung, George Adams, Amitava Ghosh, Biswajit Dasgupta, Asadul H. Chowdhury, and Sitakanta Mohanty

Center for Nuclear Waste Regulatory Analyses
San Antonio, Texas

May 2003

PREVIOUS REPORTS IN SERIES

Name	Date
Assessment of Mechanical Response of Drip Shields Under Repository Environment—Progress Report	May 2000
Assessment of Mechanical Response of Drip Shields Under Repository Environment—Progress Report 2	November 2001

ABSTRACT

The objective of this study was to develop an approach for stochastically estimating the number of drip shield and waste package failures attributable to rockfall and seismic events as a function of time through the 10,000-yr regulatory period of interest for the proposed geological repository for spent nuclear fuel and high-level radioactive waste at Yucca Mountain, Nevada. To meet this objective, a new Total-system Performance Assessment (TPA) code module (MECHFAIL), designed to assess the effects of mechanical loading (i.e., static and dynamic rockfall loads and seismicity) on the engineered barrier subsystem, was developed. This module includes abstractions that can be used to approximate and evaluate (i) the spatial and temporal distributions of rockfall loads, both static and dynamic; (ii) the number of seismic events expected during the regulatory period, their occurrence times, and the associated ground motion magnitudes (i.e., peak ground accelerations); (iii) the mechanical effects of rockfall and seismic loads on the drip shields; and (iv) the applicable failure mechanisms and their respective failure criteria. The abstractions have been incorporated into the MECHFAIL module so an approximation of the number of drip shield failures attributable to rockfall and seismic events as a function of time can be provided as input to the TPA code for each realization. The effects of material and structural degradation caused by various corrosion processes (including stress corrosion cracking), fabrication flaws, weld residual stresses, and hydrogen embrittlement have not been included in the abstractions.

Potential failure mechanisms of the drip shield accounted for in the MECHFAIL module include accumulated equivalent plastic strains that exceed the allowable ductility of the drip shield materials (i.e., the Titanium Grade 7 plates and Titanium Grade 24 bulkheads) resulting from dynamic rock block impacts and creep caused by static rockfall loads. Structural buckling of the drip shield under static rockfall loads and seismic excitation is accounted for as well. Although the abstractions have yet to be completed, the MECHFAIL module includes placeholders for assessing waste package damage caused by direct seismic shaking and interactions with the drip shield caused by static and dynamic rockfall loads. As with the drip shield, the damage incurred by the waste package outer barrier is characterized in terms of the accumulated equivalent plastic strain. The von Mises stress of the waste package outer barrier is also evaluated to facilitate the assessment of stress corrosion cracking as a potential failure mechanism.

Seismically induced rockfall is modeled using (i) seismic event histories calculated from an abstraction of the seismic ground motion hazard curve for Yucca Mountain, (ii) block-size distribution curves obtained through analyses of Yucca Mountain fracture data, and (iii) a relationship between drift degradation and ground motion magnitudes based on empirical data for seismically induced damage to underground openings. Nonseismic rockfall and the associated drift degradation were modeled using (i) a mass balance between the *in-situ* and rubbled states of the rock mass surrounding the drift opening and (ii) temporal degradation rates that are based on an engineering assessment of the available stand-up time data for excavations in fractured rock. Both seismic and nonseismic induced rockfall are accumulated in the model to approximate the static rockfall loads acting on the drip shield and the degraded configuration of emplacement drifts.

Rock engineering experience suggests that the degradation zone above an emplacement drift will likely follow an elliptical cross section, and the volume of rockfall rubble in a degraded drift can be related to the *in-situ* (i.e., before degradation) rock volume through the rock bulking factor. For an elliptical drift degradation geometry, values of bulking factor in the

range of 1.15 to 1.5 give values of static rockfall load acting on the drip shield in the range of 40 to 160 tonne/m [26,890 to 107,550 lb/ft] along the length of the drift. It is argued that the drifts would fully backfill themselves, and the corresponding limiting static rockfall loads would be fully attained, within the first 1,000 years after cessation of drift maintenance. This assessment is based on a consideration of the anticipated stand-up time for an unsupported opening in fractured rock and the reasonable assumption that the emplacement drifts would be maintained during the preclosure period but not thereafter.

The magnitudes of dynamic rock block impacts on the drip shield were determined using the block size distribution data for the lower lithophysal and middle nonlithophysal rock units. It was judged that formation of discrete rock blocks of any consequence in the lower lithophysal rock unit is unlikely because of its highly fractured nature. The analysis of the middle nonlithophysal rock unit, however, indicated that rock blocks of sufficient size to cause an appreciable dynamic impact on the drip shield and, potentially, the waste package (by causing the drip shield to subsequently impact the waste package) are likely. The distribution of rock block sizes within the middle nonlithophysal rock unit is such that approximately 60 percent will have a volume less than 1 m^3 [35.3 ft^3], which corresponds to a rock block mass of 2.25 tonne [4,960 lb] {for a rock mass density of 2.25 tonne/m^3 [140 lb/ft^3]}. Twenty-five percent of the rock blocks have a volume of 1 to 2 m^3 [35.3 to 70.6 ft^3] {2.25 to 4.50 tonne [4,960 to 9,920 lb]}, and the remaining 15 percent have a volume greater than 2 m^3 [70.6 ft^3] {4.50 tonne [9,920 lb]}.

The results obtained from finite element models of the drip shield subjected to static rockfall loads indicate the drip shield may buckle under loads as small as 23 tonne/m [15,460 lb/ft]. Moreover, static rockfall loads sufficient to initiate creep of the drip shield Titanium Grade 7 plate can be as low as 15 tonne/m [10,083 lb/ft] and, for the Titanium Grade 24 bulkhead, 20 tonne/m [13,444 lb/ft]. These threshold loads were found to increase significantly as the effective stiffness (i.e., structural support) of the accumulated rubble around the drip shield increased. The effective stiffness of the accumulated rubble and, therefore, the additional structural support it provides the drip shield, is highly uncertain because the rubble is not an engineered feature. Furthermore, the rubble properties are expected to vary spatially within a drift because of variations in the amount, density, packing, and previous compression of the rubble. Based on these considerations and a suite of finite-element model results discussed in this report, the drip shield buckling load was assigned using a beta distribution that has a range from 25 tonne/m [16,800 lb/ft], which corresponds to a negligible side support from rubble; to 150 tonne/m [100,800 lb/ft], which corresponds to an accumulated rubble with an effective stiffness of approximately 10 MPa [1,440 psi]. The drip shield buckling load beta distribution also has the characteristic that no more than 20 percent of the drip shields will have a buckling load threshold greater than 60 tonne/m [40,330 lb/ft]. Preliminary MECHFAIL analyses indicate that, on average, 75 percent of the drip shields fail within 500 years after cessation of maintenance of the emplacement drifts. These drip shield failures are predominantly caused by structural buckling under static rockfall loads.

The work related to the development of the MECHFAIL module is intended to facilitate the review of any information submitted to complete the various Key Technical Issue agreements between the U.S. Department of Energy (DOE) and the U.S. Nuclear Regulatory Commission (NRC) pertaining to the performance assessment of the engineered barrier subsystem when subjected to rockfall and seismic ground motions.

It is important to note that the TPA code is being developed to allow the NRC and Center for Nuclear Waste Regulatory Analyses staffs to perform interim evaluations of the DOE total system performance assessment approaches and parameter values used to estimate the performance of the proposed high-level waste geologic repository. Because investigations at the Yucca Mountain site are ongoing, the engineered barrier subsystem structure and component designs have yet to be finalized, and the analyses are iterative; the TPA code is being developed with flexibility to analyze a variety of site characteristics, designs, and compliance demonstration factors. It is also important to note that the particular conceptual models and assignment of initial model parameter values (and distributions) in this description of the MECHFAIL module of the TPA code do not constitute regulatory acceptance. It is expected that at the time of licensing, different conceptual models and parameter values and distributions will be used in performance assessments. Thus, estimates of the engineered barrier subsystem performance when subjected to mechanical loading using the MECHFAIL module do not represent a regulatory determination of total system performance for the Yucca Mountain, Nevada, site.

CONTENTS

Section Page

PREVIOUS REPORTS IN SERIES ii
ABSTRACT iii
FIGURES xi
TABLES xv
ACKNOWLEDGMENTS xvii

1 INTRODUCTION 1-1

1.1 Background 1-1
1.2 Objective and Scope 1-2

2 OVERVIEW OF THE MECHFAIL TOTAL-SYSTEM PERFORMANCE ASSESSMENT MODULE 2-1

2.1 MECHFAIL Module Design 2-1
2.2 Assumptions Used in Developing the MECHFAIL Module Abstractions 2-2

3 SEISMIC HAZARD CURVE ABSTRACTION 3-1

3.1 Seismic Hazard Curve 3-1
3.2 Sampling of Event Time 3-3
3.3 Sampling of Seismic Event Magnitude 3-3

4 APPROXIMATION OF ROCKFALL LOAD MAGNITUDES AND PROBABILITIES 4-1

4.1 Characterization of Accumulated Rockfall Static Loads 4-2
4.1.1 Accumulated Rockfall Static Load Distribution 4-5
4.1.2 Accumulated Rockfall Static Load Abstraction 4-13
4.2 Characterization of Discrete Rock Block Impact Loads 4-17
4.2.1 Discrete Rock Block Size Distribution 4-17
4.2.1.1 Joint Data Input 4-17
4.2.1.2 Generation of Fracture Surfaces in Space 4-17
4.2.1.3 Probability of Occurrence of Block Size 4-19
4.2.2 Discrete Rock Block Loads 4-21
4.2.3 Discrete Rock Block Load Abstraction 4-21

5 DRIP SHIELD AND ACCUMULATED ROCKFALL STATIC LOAD PERFORMANCE ANALYSES 5-1

5.1 Finite Element Model Description 5-1
5.1.1 Finite Element Model Geometry 5-2
5.1.2 Finite Element Model Boundary Conditions 5-6
5.1.2.1 Loads 5-6
5.1.2.2 Kinematic Constraints 5-6
5.1.3 Finite Element Model Material Properties 5-6
5.2 Summary of Analysis Results 5-10

CONTENTS (continued)

Section Page

5.2.1 Drip Shield Deflection 5-10
5.2.2 Drip Shield Component Stresses 5-11
5.3 Data Abstractions for MECHFAIL 5-15
5.3.1 Drip Shield Buckling Abstraction 5-15
5.3.2 Drip Shield Component Stress Abstraction 5-20

6 DRIP SHIELD AND WASTE PACKAGE INTERACTION CAUSED BY ACCUMULATED ROCKFALL STATIC LOADS PERFORMANCE ANALYSES 6-1

6.1 Finite Element Model Description 6-3
6.1.1 Finite Element Model Geometry 6-3
6.1.2 Finite Element Model Boundary Conditions 6-9
6.1.2.1 Loads 6-9
6.1.2.2 Kinematic Constraints 6-9
6.2 Summary of Analysis Results 6-9
6.3 Data Abstractions for MECHFAIL 6-10

7 DRIP SHIELD AND DYNAMIC ROCK BLOCK IMPACT PERFORMANCE ANALYSES 7-1

7.1 Finite Element Model Description 7-1
7.1.1 Drip Shield Finite Element Model 7-1
7.1.2 Finite Element Model of the Rock Block 7-2
7.1.3 Finite Element Model Boundary Conditions 7-3
7.1.3.1 Loads 7-3
7.1.3.2 Kinematic Constraints 7-6
7.1.4 Finite Element Model Material Properties 7-7
7.2 Summary of Analysis Results 7-7
7.2.1 Drip Shield Deflection 7-7
7.2.2 Drip Shield Component Stresses and Strains 7-7
7.3 Data Abstractions for MECHFAIL 7-10
7.3.1 Drip Shield Maximum Deflection Abstraction 7-10
7.3.2 Drip Shield Displacement and Velocity Relationship Abstraction . . . 7-13
7.3.3 Drip Shield Component Stress and Plastic Strain Abstractions 7-16

8 SEISMIC PERFORMANCE ANALYSES 8-1

8.1 Approximation of Drip Shield Natural Frequencies 8-1
8.1.1 Drip Shield Finite Element Model Description 8-1
8.1.1.1 Drip Shield Finite Element Model Geometry 8-2
8.1.1.2 Drip Shield Finite Element Model Boundary Conditions . . 8-2
8.1.1.2.1 Loads 8-2
8.1.1.2.2 Kinematic Constraints 8-2
8.1.1.3 Drip Shield Finite Element Model Material Properties 8-4
8.1.1.4 Summary of Drip Shield Natural Frequencies and Mode Shapes 8-4

CONTENTS (continued)

Section Page

8.2 Response of the Drip Shield to Seismic Excitations 8-15
8.2.1 Finite Element Model Description 8-15
8.2.2 Summary of Analysis Results 8-15
8.2.3 Data Abstractions for MECHFAIL 8-15
8.3 Approximation of Waste Package Natural Frequencies 8-15
8.3.1 Finite Element Model Description 8-15
8.3.2 Summary of Analysis Results 8-16
8.4 Response of the Waste Package to Seismic Excitations 8-16
8.4.1 Finite Element Model Description 8-16
8.4.2 Summary of Analysis Results 8-16
8.4.3 Data Abstractions for MECHFAIL 8-16

9 SUMMARY OF RESULTS 9-1

10 FUTURE WORK 10-1

11 REFERENCES 11-1

APPENDIX A

FIGURES

Figure		Page
2-1	Flowchart of the MECHFAIL Module	2-3
2-2	Flowchart of the PROCESSELEMENTS Subroutine	2-5
3-1	Seismic Hazard Curve Relating Annual Frequency of Exceedance and Return Period to Mean Peak Horizontal Ground Acceleration	3-2
3-2	Histogram Showing Convergence to Exponentially Distributed Samples of Return Periods for a Single Realization of 100,000 Years	3-4
3-3	Sampled Values of Mean Peak Horizontal Ground Acceleration as a Function of Time for a Single Realization of 100,000 Years	3-4
4-1	Illustration of the Drift Void and Drift Degradation Zone Area Parameters	4-6
4-2	Potential Drift Degradation Geometries	4-7
4-3	Parameters Used to Approximate Drip Shield Crown Pressure Loads	4-8
4-4	Maximum Static Rockfall Load Acting on the Drip Shield Crown for the Trapezoidal (+ θ) and Triangular (- θ) Drift Degradation Geometries	4-10
4-5	Maximum Drip Shield Static Rockfall Load as a Function of the Bulking Factor for the Elliptical Drift Degradation Geometry	4-10
4-6	Maximum Drift-Degradation Zone Height as a Function of the Bulking Factor for the Elliptical Drift Degradation Geometry	4-11
4-7	Variations of the Height of a Potential Drift-Degradation Zone Based on a Limit-Equilibrium Analysis of Chimney Caving Above an Emplacement Drift	4-13
4-8	Allowable Unsupported Span as a Function of Rock Mass Quality	4-15
4-9	Estimated Ranges of Drift Stand-up Time for Different Rock Mass Quality Indices and Unsupported Span Lengths	4-15
4-10	Beta Distribution Defining the Time Required for the Drifts to Backfill Themselves Completely	4-16
4-11	Normalized Histogram of Rock Block Size Distribution for the Topopah Spring Welded Tuff Middle Nonlithophysal Rock Unit	4-20
4-12	Cumulative Rock Block Size Distribution for the Topopah Spring Welded Tuff Middle Nonlithophysal Rock Unit	4-20
4-13	Characterization of Drift Damage as a Function of Ground Surface Peak Ground Accelerations	4-22
4-14	Change in the Drift Degradation Zone Height as a Function of Mean Peak Horizontal Ground Acceleration	4-23
4-15	Beta Distribution Defining the Mean Peak Horizontal Ground Acceleration Required to Cause Minor Drift Damage	4-24
4-16	Beta Distribution Defining the Mean Peak Horizontal Ground Acceleration Required to Cause Major Drift Damage	4-24
5-1	Drip Shield and Accumulated Rockfall Interaction Model	5-3
5-2	Drip Shield Components	5-4
5-3	Drip Shield and Accumulated Rockfall Rubble Interaction Model Kinematic Boundary Conditions	5-5

FIGURES (continued)

Figure		Page
5-4	Drip Shield Deflection Versus Static Rockfall Load for Varying Rock Rubble Young's Moduli	5-11
5-5	Drip Shield Deformation Under Static Rockfall Loads	5-12
5-6	Bulkhead von Mises Stress Distribution and Deformation Corresponding to Maximum Static Rockfall Loads for Different Bulking Factors	5-13
5-7	Comparison of Drip Shield Buckling Geometries With and Without Rock Rubble Lateral Support	5-14
5-8	Maximum Bulkhead von Mises Stress and Equivalent Plastic Strain Versus Static Rockfall Load With No Accumulated Rockfall Rubble Lateral Support	5-16
5-9	Maximum Bulkhead von Mises Stress and Equivalent Plastic Strain Versus Static Rockfall Load With Accumulated Rockfall Rubble Lateral Support {Effective Rock Rubble Young's Modulus = 3 MPa [4.35 × 10^2 psi]}	5-16
5-10	Maximum Bulkhead von Mises Stress and Equivalent Plastic Strain Versus Static Rockfall Load With Accumulated Rockfall Rubble Lateral Support {Effective Rock Rubble Young's Modulus = 6 MPa [8.70 × 10^2 psi]}	5-17
5-11	Maximum Bulkhead von Mises Stress and Equivalent Plastic Strain Versus Static Rockfall Load With Accumulated Rockfall Rubble Lateral Support {Effective Rock Rubble Young's Modulus = 10 MPa [1.45 × 10^3 psi]}	5-17
5-12	Maximum Bulkhead von Mises Stress and Equivalent Plastic Strain Versus Static Rockfall Load With Accumulated Rockfall Rubble Lateral Support {Effective Rock Rubble Young's Modulus = 30 MPa [4.36 × 10^3 psi]}	5-18
5-13	Drip Shield Buckling Load Versus Effective Rock Rubble Young's Modulus	5-19
5-14	Beta Distribution Defining the Drip Shield Buckling Load	5-20
6-1	Waste Package and Drip Shield Static Rockfall Load Interaction Model	6-4
6-2	Waste Package Model Components	6-5
6-3	Waste Package Inner Barrier Components	6-6
6-4	Waste Package Outer Barrier Components	6-7
6-5	Waste Package and Drip Shield Interaction Model Boundary Conditions	6-8
7-1	Schematic Illustrating the Planes of Symmetry Used to Simplify the Drip Shield and Rock Block Impact Model	7-2
7-2	Drip Shield and Rock Block Impact Finite Element Model	7-4
7-3	Drip Shield Deflection Versus Time for 0.5 tonne/m [336 lb/ft] Rock Block Impacts	7-8
7-4	Drip Shield Deflection Versus Time for 1.0 tonne/m [672 lb/ft] Rock Block Impacts	7-8
7-5	Drip Shield Deflection Versus Time for 2.0 tonne/m [1,344 lb/ft] Rock Block Impacts	7-9
7-6	Drip Shield Deflection Versus Time for 4.0 tonne/m [2,689 lb/ft] Rock Block Impacts	7-9
7-7	Drip Shield Deflection Versus Time for 8.0 tonne/m [5,378 lb/ft] Rock Block Impacts	7-10
7-8	General Locations of the Maximum Drip Shield von Mises Stress and Equivalent Plastic Strains	7-11
7-9	Maximum Drip Shield Deflection Abstraction for Rock Block Impacts	7-14
7-10	Drip Shield Velocity as a Function of Displacement Caused by Rock Block Impacts	7-15

FIGURES (continued)

Figure		Page
7-11	Maximum Drip Shield Plate von Mises Stress Abstraction by Rock Block Impacts	7-18
7-12	Maximum Drip Shield Plate Equivalent Plastic Strain Abstraction for Rock Block Impacts	7-19
7-13	Maximum Drip Shield Bulkhead von Mises Stress Abstraction for Rock Block Impacts	7-20
7-14	Maximum Drip Shield Bulkhead Equivalent Plastic Strain Abstraction for Rock Block Impacts	7-21
8-1	Model Used to Approximate the Drip Shield Natural Frequencies and Mode Shapes	8-3
8-2	Illustration of the Drip Shield Lateral Constraint Condition	8-5
8-3	Illustration of the Drip Shield Cantilevered Constraint Condition	8-6
8-4	Illustration of the Drip Shield Walking Mode Shape	8-11
8-5	Illustration of the Drip Shield Flapping Mode Shape	8-12
8-6	Illustration of the Drip Shield Lateral Wall Mode Shape	8-13
8-7	Illustration of the Drip Shield Pinch Crown Mode Shape	8-14
9-1	Mean Fraction and Standard Deviation of Drip Shield Failures as a Function of the Number of Spatial Grid Elements per Subarea	9-5
9-2	Mean Fraction and Standard Deviation of Drift Failures as a Function of the Number of Spatial Grid Elements per Subarea	9-5

TABLES

Table		Page
1-1	Related Key Technical Issue Subissues and Agreements	1-4
3-1	Seismic Hazard Curve Data Input to the TPA Code	3-2
4-1	Bulking Factors for Common Soils and Rock Types	4-4
4-2	Values of Bulking Factor for Various Coal Measure Rocks	4-4
4-3	Fracture Information for Topopah Spring Welded Tuff Middle Nonlithophysal Rock Unit	4-18
4-4	Fracture Information for Topopah Spring Welded Tuff Lower Lithophysal Rock Unit	4-18
5-1	Maximum Static Rockfall Loads for a Given Bulking Factor	5-7
5-2	Summary of Drip Shield Material Property Data at 150 °C [302 °F]	5-7
5-3	Drip Shield Component Materials	5-7
5-4	Drip Shield Material Data for Modeling Post-Yield Behavior at 150 °C [302 °F]	5-9
5-5	Case Numbers for the Assumed Rock Rubble Young's Moduli Evaluated	5-9
5-6	Total Static Rockfall Load Needed to Initiate Creep for Varying Rock Rubble Young's Moduli	5-18
7-1	Drip Shield and Rock Block Impact Scenarios Included in the Parametric Study	7-5
7-2	Elastic Material Properties Used for the Rock Block Mass	7-7
7-3	Maximum Drip Shield Plate and Bulkhead Stress and Strain Results	7-12
8-1	Mode Shapes, Natural Frequencies, and Modal Participation Factors of the Drip Shield for Free Constraint Conditions	8-7
8-2	Mode Shapes, Natural Frequencies, and Modal Participation Factors of the Drip Shield for Lateral Constraint Conditions	8-8
8-3	Mode Shapes, Natural Frequencies, and Modal Participation Factors of the Drip Shield for Cantilever Constraint Conditions	8-9

ACKNOWLEDGMENTS

This report documents work performed by the Center for Nuclear Waste Regulatory Analyses (CNWRA) for the U.S. Nuclear Regulatory Commission (NRC) under Contract No. NRC–02–02–012. The activities reported here were performed on behalf of the NRC Office of Nuclear Material Safety and Safeguards, Division of Waste Management. This report is an independent product of the CNWRA and does not necessarily reflect the views or regulatory position of the NRC.

The authors thank W. Patrick and B. Sagar for their reviews of this report. The authors also express their appreciation to the NRC staff (T. Ahn, T. Bloomer, R. Codell, A. Csontos, D. Esh, J. Firth, A. Ibrahim, B. Jagannath, Y. Kim, T. McCartin, and M. Nataraja) for their thorough technical and programmatic reviews of this report. The authors are thankful to A. Ramos for assisting with the word processing and preparation of the final report and to C. Cudd, J. Pryor, and A. Woods for the editorial review.

QUALITY OF DATA, ANALYSES, AND CODE DEVELOPMENT

DATA: All CNWRA-generated original data contained in this report meet quality assurance requirements described in the CNWRA Quality Assurance Manual. Sources for other data should be consulted for determining the level of quality for those data. The work presented in this report is documented in CNWRA Scientific Notebooks 391, 409, 410, 417, and 422.

ANALYSES AND CODES: Finite element analyses in this report were conducted by the CNWRA using the commercial computer codes ABAQUS/Standard (Hibbitt, Karlsson & Sorensen, Inc., 1998a, 2001a) and ABAQUS/Explicit (Hibbitt, Karlsson & Sorensen, Inc., 1998b) Versions 5.8–16 and 6.2. Pre- and post-processing of the finite element models were accomplished using the commercial computer codes ABAQUS/CAE (Hibbitt, Karlsson & Sorensen, Inc., 2001b) Version 6.2 and HyperMesh (Altair Engineering, Inc., 1998) Version 3.1. ABAQUS/Standard, ABAQUS/Explicit, ABAQUS/CAE, and HyperMesh are controlled under the CNWRA software Quality Assurance procedure (TOP–018, Development and Control of Scientific and Engineering Software). Spreadsheet calculations were accomplished using Microsoft® Excel 97 SR–2 (Microsoft Corporation, 1997). Additional calculations were performed using Mathcad 2000 Professional (Mathsoft Engineering & Education, Inc., 1999).

REFERENCES

Altair Engineering, Inc. "Altair HyperWorks Essentials." Troy, Michigan: Altair Engineering, Inc. 1998.

Hibbitt, Karlsson & Sorensen, Inc. "ABAQUS/Standard User's Manual, Version 5.8." Pawtucket, Rhode Island: Hibbitt, Karlsson & Sorensen, Inc. 1998a.

Hibbitt, Karlsson & Sorensen, Inc. "ABAQUS/Explicit User's Manual, Version 5.8." Pawtucket, Rhode Island: Hibbitt, Karlsson & Sorensen, Inc. 1998b.

Hibbitt, Karlsson & Sorensen, Inc. "ABAQUS/Standard User's Manual, Version 6.2." Pawtucket, Rhode Island: Hibbitt, Karlsson & Sorensen, Inc. 2001a.

Hibbitt, Karlsson & Sorensen, Inc. "ABAQUS/CAE User's Manual, Version 6.2." Pawtucket, Rhode Island: Hibbitt, Karlsson & Sorensen, Inc. 2001b.

Mathsoft Engineering & Education, Inc. "Mathcad 2000 Professional." Cambridge, Massachusetts: Mathsoft Engineering & Education, Inc. 1999.

Microsoft Corporation. "Microsoft® Excel 97 SR–2." Redmond, Washington: Microsoft Corporation. 1997.

1 INTRODUCTION

1.1 Background

The U.S. Department of Energy (DOE) has been studying the Yucca Mountain site in Nevada for more than 15 years to determine whether it is suitable for building a geologic repository for the nation's spent nuclear fuel and high-level waste (DOE, 1998a). The proposed repository design employs an engineered barrier subsystem in concert with the desert environment and geologic features of Yucca Mountain to limit water contacting the spent nuclear fuel and high-level waste for thousands of years. Two primary components of the engineered barrier subsystem are the drip shield and waste package (CRWMS M&O, 1999a). Other potential components of the engineered barrier subsystem include backfill and emplacement drift seals. The basic concept of geologic disposal at Yucca Mountain is the placement of carefully prepared and packaged nuclear waste in excavated tunnels in tuff about 350 m [1,148 ft] below the surface and 225 m [738 ft] above the water table. In this condition, the engineered barriers are intended to work with the natural barriers—the geology and climate of Yucca Mountain—to contain and isolate the nuclear waste for thousands of years. For example, the evolving engineered barrier component designs include materials chosen to be compatible with the underground thermal and geochemical environment, and the layout of tunnels takes into consideration the geology of the mountain (DOE, 1998a).

Through successive evaluations, the repository design evolved to the Viability Assessment reference design (DOE, 1998a,b). This reference design represented a snapshot of the ongoing design process, thus providing a frame of reference to describe how the proposed repository at Yucca Mountain could work. Following the presentation of the Viability Assessment reference design for the proposed repository to the U.S. Congress, the License Application Design Selection was completed by the DOE (CRWMS M&O, 1999a,b,c). The goal of the License Application Design Selection was to develop and evaluate a diverse range of conceptual repository designs that would be compatible with the geologic attributes of the Yucca Mountain site and to recommend an initial design concept for the possible Site Recommendation and License Application documents. Ultimately, the potential benefits of five variations of the Viability Assessment reference design were studied to identify design attributes that could improve the functional characteristics of the proposed repository. A new repository reference design has been adopted by the DOE as a consequence. This new design, referred to as Enhanced Design Alternative II, uses more extensive thermal management techniques than the Viability Assessment design to redirect water flow through the rock mass between the emplacement drifts (CRWMS M&O, 1999b). The new Enhanced Design Alternative II design also differs from the Viability Assessment design in that steel structural materials are now primarily used in the drifts instead of concrete to avoid possible adverse chemical reactions pertaining to corrosion, as well as mobilization and movement of radionuclides.

The repository design strategy has been brought further into focus by the Yucca Mountain Science and Engineering Report (CRWMS M&O, 2001). For example, the initial intent and design functionality of the drip shield was limited to protecting the waste package from dripping water originating from the drift roof. As documented in the Yucca Mountain Science and Engineering Report, however, DOE is currently attempting to design the drip shield to protect the waste package from all potential rockfall loads (i.e., both static and dynamic) and, as a result, limit the potential number of waste packages that may be breached because of this form of mechanical disruption (CRWMS M&O, 2001). Static rockfall loads are caused by the

accumulation of discrete rock blocks and rubble that have fallen from the emplacement drift roof over time. Dynamic rockfall loads occur when individual discrete rock blocks are dislodged from the drift roof and free fall until impacting the drip shield. The seismic hazard curve is an important input parameter for approximating the occurrence of rockfall in the emplacement drifts because of earthquake-induced ground shaking.

In addition to rockfall, other credible mechanically disruptive events include seismicity, faulting, and igneous activity. With regard to seismic effects alone, two potential failure mechanisms have been identified. Depending on the peak ground acceleration of the seismic event and the concomitant dynamic response of the drip shield and waste package, stresses sufficient to cause localized plastic deformations may occur. The occurrence of plastic deformations implies the existence of residual stresses that are sufficient for stress corrosion cracking of the engineered barrier materials to occur. It has not been definitively established, however, whether the environment within the emplacement drifts is conducive to stress corrosion cracking. Accumulated plastic strains caused by repeated seismic events represents the other potential failure mechanism.

Even though the presence of engineered or naturally occurring backfill (i.e., accumulated rockfall rubble) significantly reduces the fault displacement magnitude needed to exert loads on the drip shield and waste package, the expected magnitudes of fault displacement are not likely to cause significant drip shield or waste package damage (Waiting, et al., 2003). In addition, as an extra mitigative design feature, no waste packages will be emplaced near any known faults. The closest a waste package can be emplaced to a known fault is called the fault-setback distance. Moreover, the potential effect of faulting on the drip shield is likely to be limited to the misalignment of adjacent drip shield units. The extent of the water infiltration pathways created from this misalignment is expected to be small and, given the limited spatial occurrence of faulting and the aforementioned fault-setback requirement, the potential effects of fault slip on drip shield and waste package performance are considered to be negligible at this time.

Igneous intrusion is a mechanically disruptive event that is addressed separately and is outside the scope of work addressed in this report.

1.2 Objective and Scope

The objective of this study was to develop an approach for stochastically estimating the number of drip shield and waste package failures attributable to rockfall and seismic events as a function of time during the 10,000-yr regulatory period of interest for the proposed geological repository for spent nuclear fuel and high-level radioactive waste at Yucca Mountain, Nevada. Meeting this objective requires the development of quantitative functions, commonly referred to as abstractions, that can be used to approximate and evaluate (i) the spatial and temporal distributions of rockfall loads, both static and dynamic; (ii) the number of seismic events expected during the regulatory period, their occurrence times, and the associated ground motion magnitudes (i.e., peak ground accelerations, peak ground velocities, frequency response spectrums, energy density functions); (iii) the mechanical effects of these rockfall and seismic loads on the drip shields and waste packages; and (iv) the applicable failure mechanisms and their respective failure criteria. The abstractions will be incorporated into the MECHFAIL module so an approximation of the number of drip shield and waste package failures attributable to rockfall and seismic events as a function of time can be provided as input to the Total-system Performance Assessment code. It is important to note that the effects of

material and structural degradation caused by various corrosion processes (including stress corrosion cracking), fabrication flaws, weld residual stresses, and hydrogen embrittlement have not been included in the abstractions.

The scope of this report encompasses the following:

- Overview of the conceptual design of the MECHFAIL program module
- The technical basis and abstraction methodology for approximating the number of seismic events and their respective peak ground accelerations during the 10,000-yr regulatory period
- The development of the abstractions used to approximate the spatial and temporal distributions of static and dynamic rockfall loads
- Performance analyses of the drip shield subjected to static rockfall loads (process level model results and abstractions)
- Performance analyses of the drip shield and waste package interaction caused by static rockfall loads (process level model development)
- Performance analyses of the drip shield subjected to dynamic rockfall loads (process level model results and abstractions)
- Natural frequency and mode shape analyses for the drip shield

The scope of the work is sufficient to facilitate reviewing information submitted to complete many of the Key Technical Issue agreements that have been made between the DOE and U.S. Nuclear Regulatory Commission pertaining to the performance assessment of the engineered barrier subsystem when subjected to rockfall and seismic ground motions. The specific key technical issue agreements relevant to the work documented in this report are identified in Table 1-1. The full text of the agreements identified in Table 1-1 can be found in Appendix A.

Table 1-1. Related Key Technical Issue Subissues and Agreements			
Key Technical Issue	**Subissue**	**Status**	**Related Agreements***
Container Life and Source Term	Subissue 1—Effects of Corrosion Processes on the Lifetime of the Containers	Closed-Pending	CLST.1.14
	Subissue 2—Effects of Phase Instability of Materials and Initial Defects on the Mechanical Failure and Lifetime of the Containers	Closed-Pending	CLST.2.02 CLST.2.06 CLST.2.08
	Subissue 3—The Rate at Which Radionuclides in Spent Nuclear Fuel Are Released from the Engineered Barrier Subsystem Through the Oxidation and Dissolution of Spent Nuclear Fuel	Closed-Pending	CLST.3.10
Repository Design and Thermal-Mechanical Effects	Subissue 3—Thermal-Mechanical Effects	Closed-Pending	RDTME.3.17 RDTME.3.19
Structural Deformation and Seismicity	Subissue 2—Seismicity	Closed-Pending	SDS.2.04
Total System Performance Assessment and Integration	Subissue 2—Scenario Analysis and Event Probability	Closed-Pending	TSPAI.2.02 (Comments 34, 35, 37, 39, 78, and 79)
	Subissue 3—Model Abstraction	Closed-Pending	TSPAI.3.06

*Key Technical Issue Agreement GEN.1.01 (Comment 3) pertains to multiple integrated subissues, as well as some specific issues related to this integrated subissue.

2 OVERVIEW OF THE MECHFAIL TOTAL-SYSTEM PERFORMANCE ASSESSMENT MODULE

2.1 MECHFAIL Module Design

The MECHFAIL Total-system Performance Assessment (TPA) code module is organized on a spatial grid element basis. The spatial grid elements are discrete subdivisions of the repository footprint. For the TPA code Version 5.0 beta, each of the 10 standard subareas utilized within the code have been further divided within MECHFAIL using two spatial grid elements per subarea. Each grid element within a given subarea represents the spatial volume percentage of lithophysal and nonlithophysal rock units. Therefore, MECHFAIL is comprised of 20 spatial grid elements with each grid element assigned various properties and parameters consistent with the rock unit it is intended to represent as described in subsequent chapters of this report.

In a given time increment, each spatial grid element will experience some amount of rockfall resulting from nonseismic (i.e., thermal, mechanical, hydrological, and chemical) drift degradation processes. The specific amount of rockfall that occurs over the time increment is determined by the nonseismic drift degradation rate of the spatial grid element. As explained in more detail in Section 4.1, the drift degradation rate of each spatial grid element depends on the drift degradation time and the maximum drift degradation zone height assigned to the spatial grid element. Additional rockfall attributed to discrete seismic events is also accounted for (see Section 4.2). Dynamic rock block impact loading of the drip shield or waste package may result only from seismically induced rockfall (i.e., nonseismic rockfall contributes only to static loads). This simplification was necessary to facilitate the analysis of discrete rock block impact events. Both seismically induced and nonseismic rockfall, however, are accumulated to determine the amount of rockfall rubble for a grid element (i.e., the total static rockfall load). The effects of any dynamic rock block impact are assumed to be fully mitigated if the drip shield crown is overlain by 0.5 m [1.6 ft] or more of rockfall rubble. Analyses have yet to be performed to justify the assumed value of 0.5 m [1.6 ft] for the minimum impact-mitigation depth, however. Although the effects of dynamic rock block loads on the engineered barrier subsystem are no longer assessed once the accumulated rockfall rubble exceeds this threshold, its contribution to the static rockfall load is still taken into account. The drift degradation zone height that corresponds to the amount of rockfall needed to mitigate the effects of dynamic rock block impact loads is referred to as the impact mitigation height. Lastly, each grid element is assigned a maximum drift degradation-zone height based on the analysis discussed in Section 4.1. Both seismic and nonseismic rockfall are terminated after the maximum degradation-zone height is attained. In other words, static rockfall loads are bounded using the conservation of mass principle described in Section 4.1.

Failure of the individual components of the engineered barrier subsystem (i.e., drip shield and waste package) caused by static and dynamic rockfall loads and direct seismic shaking is achieved when the accumulated equivalent plastic strains for a given material exceeds the minimum allowable percentage of elongation as defined by the appropriate ASTM International Standard or, in the case of the drip shield, when structural buckling occurs. Equivalent plastic strain is analogous to von Mises stress in that it is the uniaxial equivalent of a three-dimensional state of plastic strain. Total equivalent plastic strain was chosen as the failure parameter because it facilitates the accumulation of damage created by discrete events. For example, discrete rock block impacts with the drip shield will cause large variations in stress (i.e., the

stress at the maximum displacement relative to the residual stress level after elastic recovery within the drip shield components). The total strain (i.e., the sum of elastic and plastic strain) within the drip shield, however, is dominated by the plastic strain. Any reduction in total strain attributable to elastic recovery is, from a practical engineering point of view, negligible. Furthermore, because the effects of strain hardening (i.e., increases in yield stress) are not accounted for in the drip shield or waste package material damage abstractions from one event to the next, any potential errors or uncertainties should be adequately bounded. A more refined approach for assessing the accumulated damage to the drip shield created by dynamic rock block impacts and creep can be developed if it is found that the current method results in these particular failure mechanisms being risk significant.

Figure 2-1 is a flow chart illustrating the overall functionality of the MECHFAIL module. As can be seen, the framework for evaluating the effects of both static and dynamic rockfall and direct seismic shaking on the engineered barrier subsystem has been completed. Abstractions for assessing the potential damage to the drip shield from both static and dynamic rockfall loads have been completed and implemented within the MECHFAIL Module subroutine PROCESSELEMENTS (see Figure 2-2). These abstractions include the effective increase in static rockfall loads that occur during a seismic event (see Section 5.3.1). Abstractions of potential drip shield and waste package interactions from both static and dynamic rockfall loads have yet to be completed, however. The abstraction of the effects of direct seismic shaking of the waste package for varying earthquake magnitudes is still under development as well. Creep of the various titanium alloys used in the construction of the drip shield is evaluated if the stress within the individual drip shield components from static rockfall loads exceed the requisite threshold (see Section 5.3.2).

The MECHFAIL module interfaces to the TPA code through the executive module (EXEC). MECHFAIL receives the TPA time steps and the distribution of seismic events throughout these time steps from the executive module. The MECHFAIL module also receives a drip shield thickness versus time distribution by way of the executive module, but this distribution is not used within MECHFAIL at the present time. Additional analyses of the drip shield in various stages of material degradation are required before relationships correlating rockfall loads and drip shield thickness with drip shield failures can be formulated. MECHFAIL returns information to the executive module that corresponds to the TPA code time steps it received. The results returned to the TPA code via the executive module are the fraction of drip shields, waste packages, and drifts that have failed and the waste package outer barrier stress. The waste package outer barrier stress may be used in future revisions of the TPA code to assess the potential effects of stress corrosion cracking. Similarly, the percentage of drift failures can be used to assess its potential effects on drift seepage and engineered barrier subsystem component temperature.

2.2 Assumptions Used in Developing the MECHFAIL Module Abstractions

The following assumptions were used in the development of the abstractions that estimate the spatial and temporal variations of static and dynamic rockfall loads and the corresponding response of the drip shield to these loads.

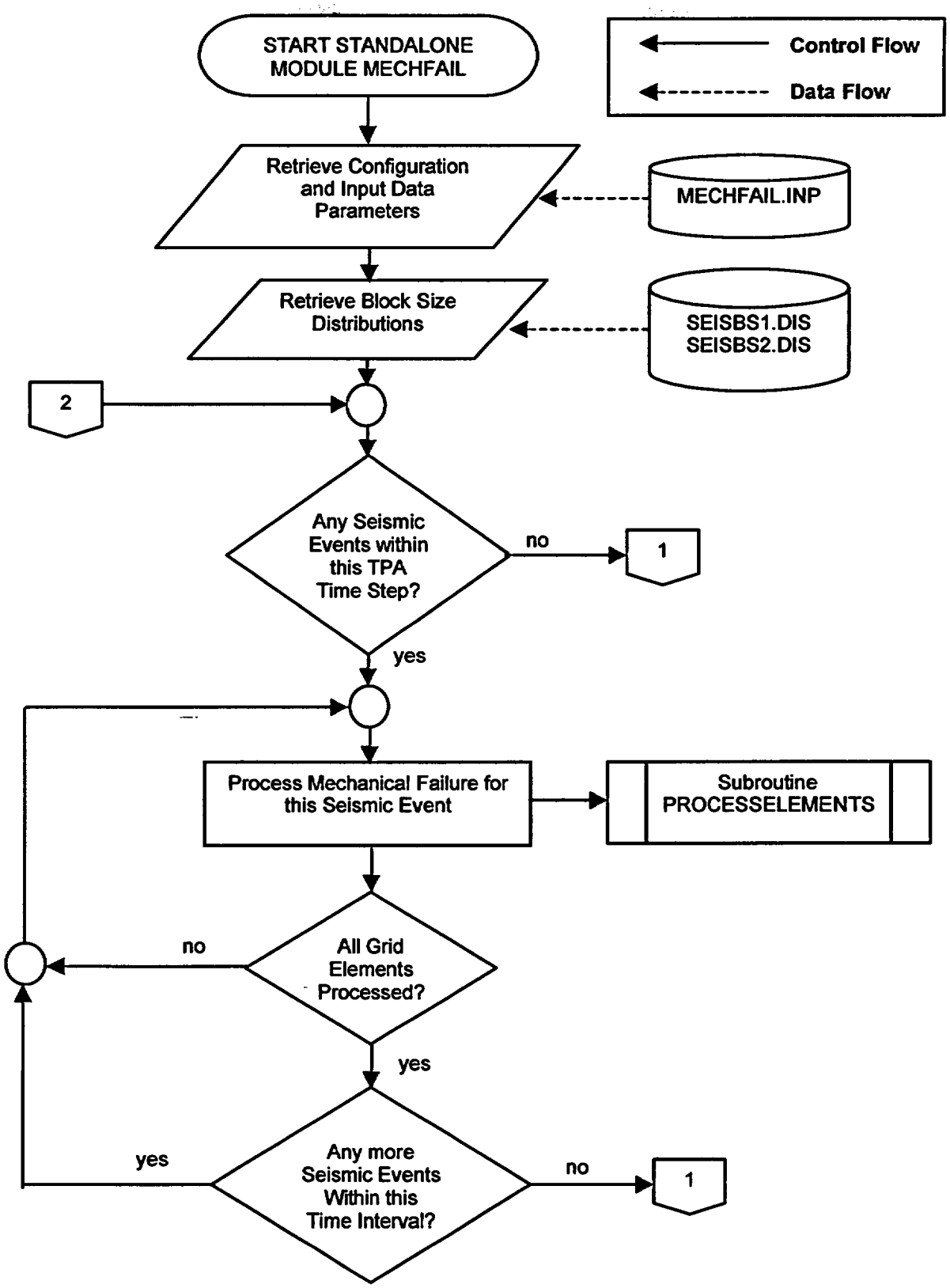

Figure 2-1. Flowchart of the MECHFAIL Module

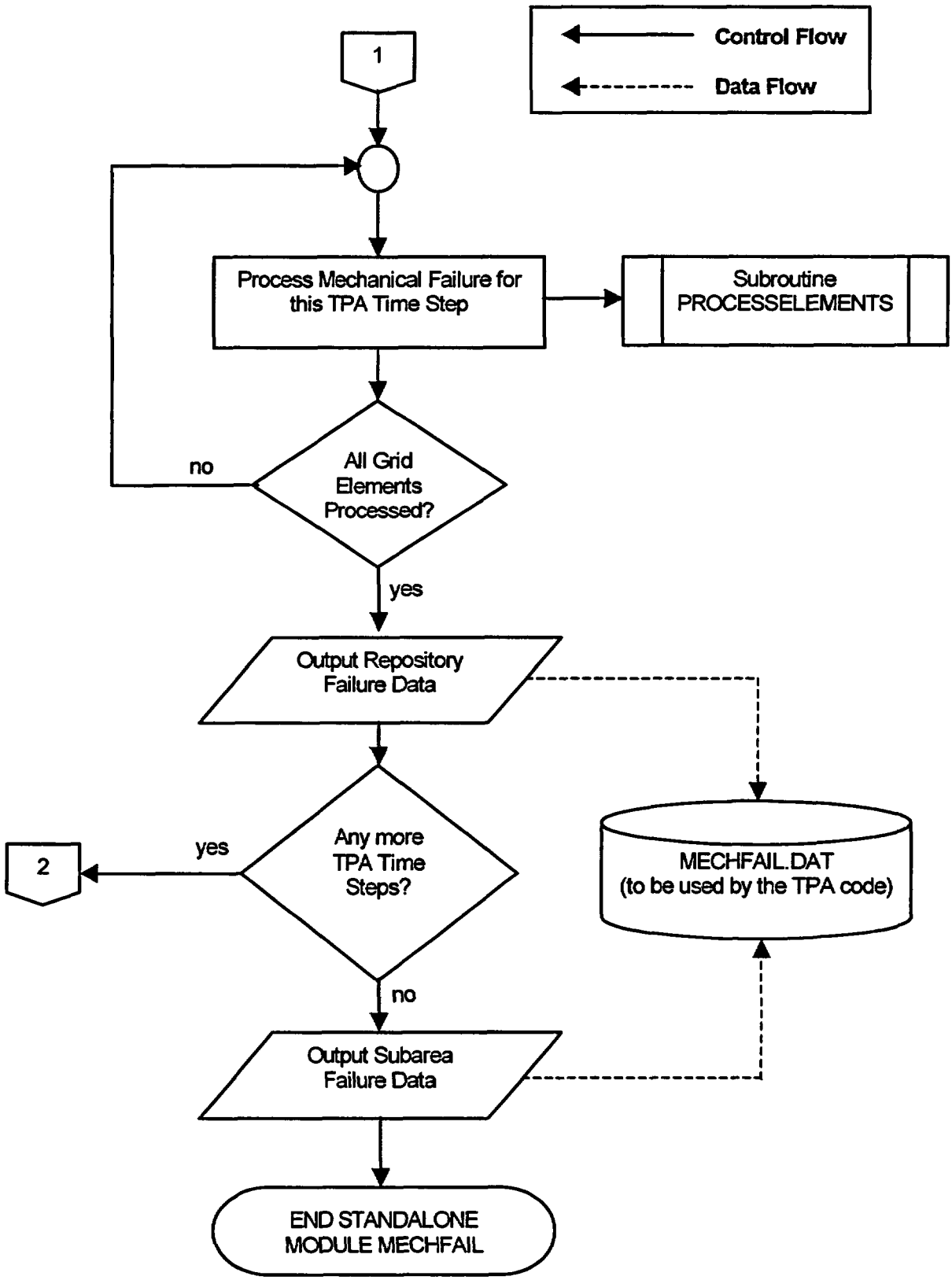

Figure 2-1. Flowchart of the MECHFAIL Module (continued)

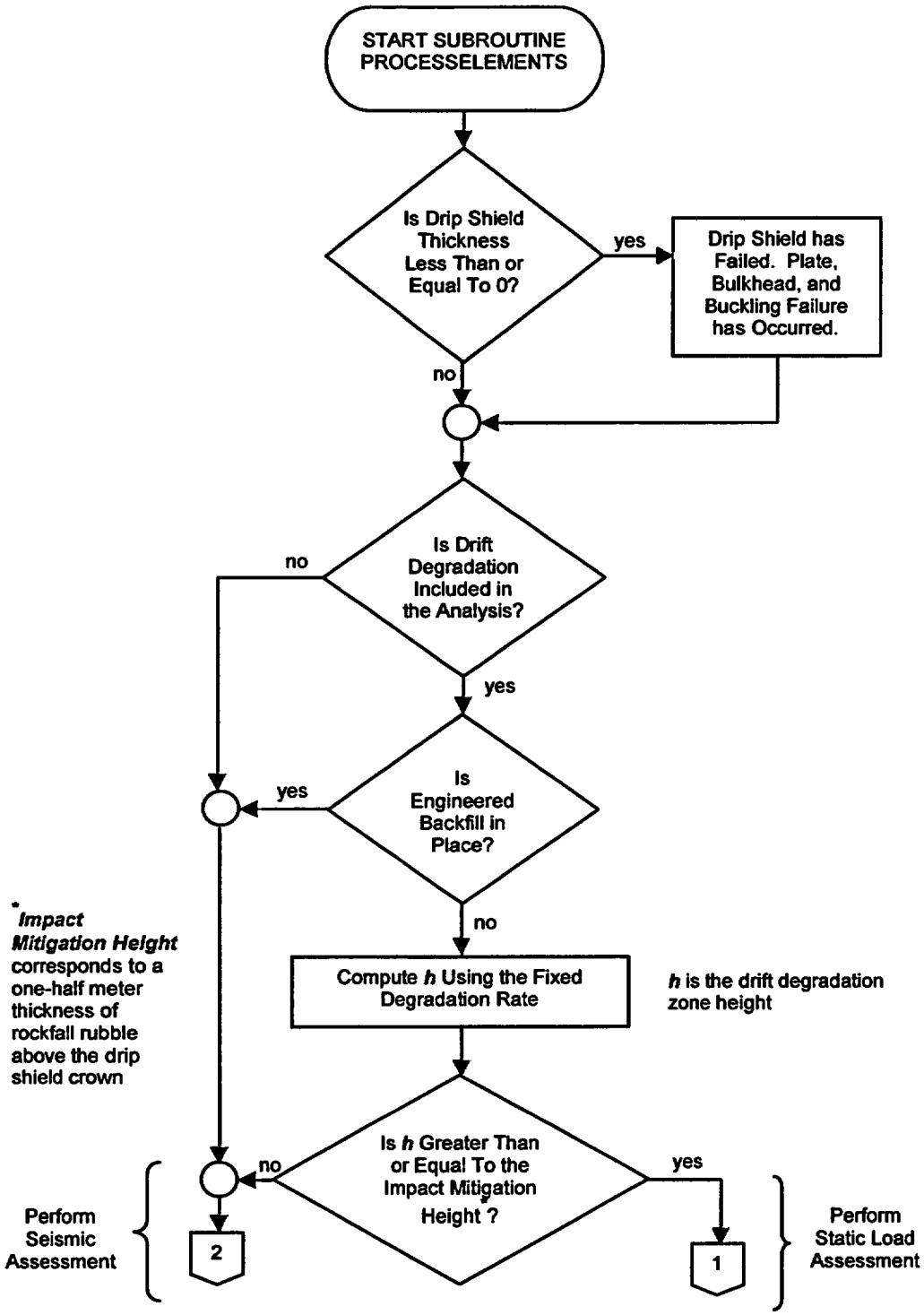

Figure 2-2. Flowchart of the PROCESSELEMENTS Subroutine

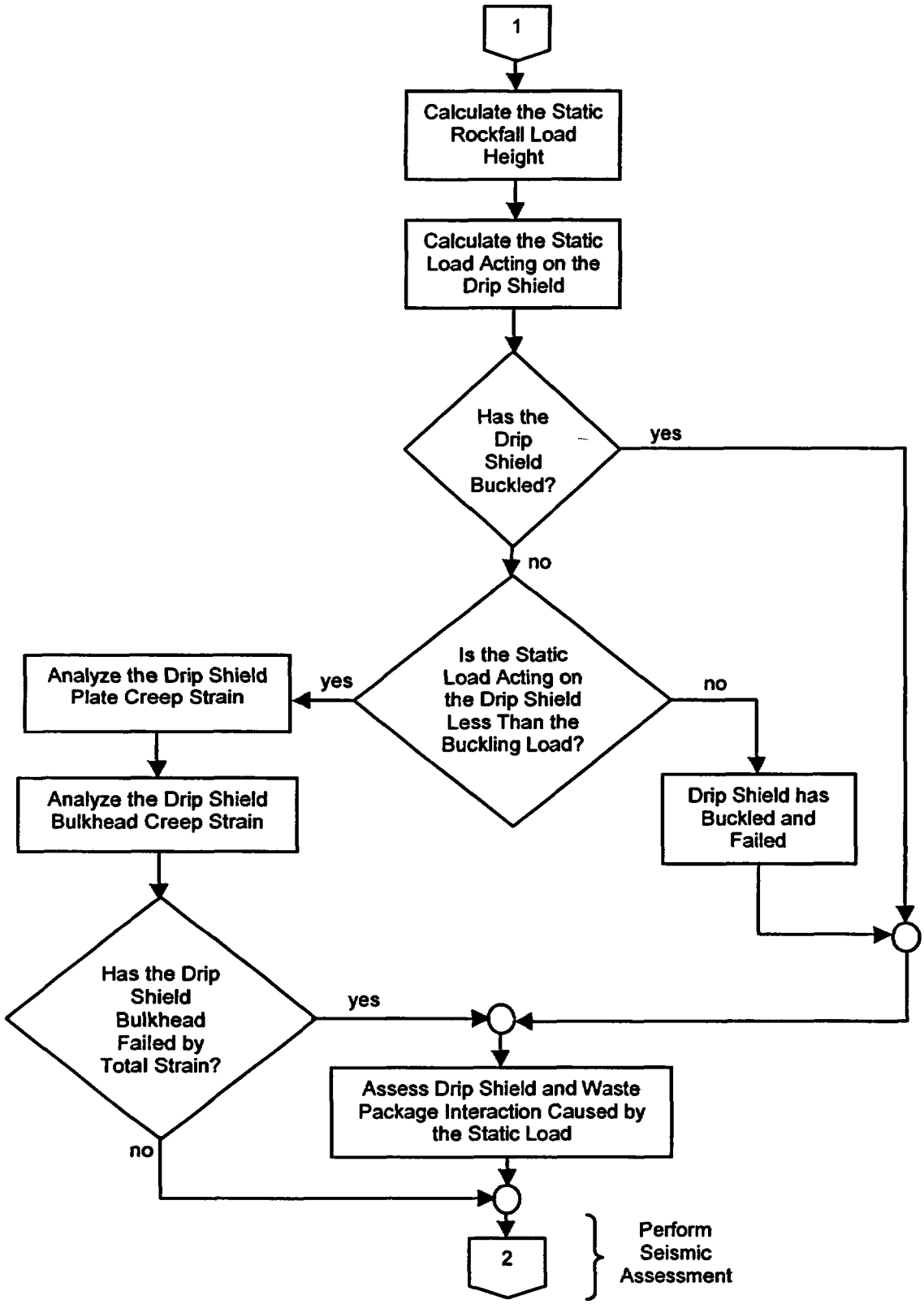

Figure 2-2. Flowchart of the PROCESSELEMENTS Subroutine (continued)

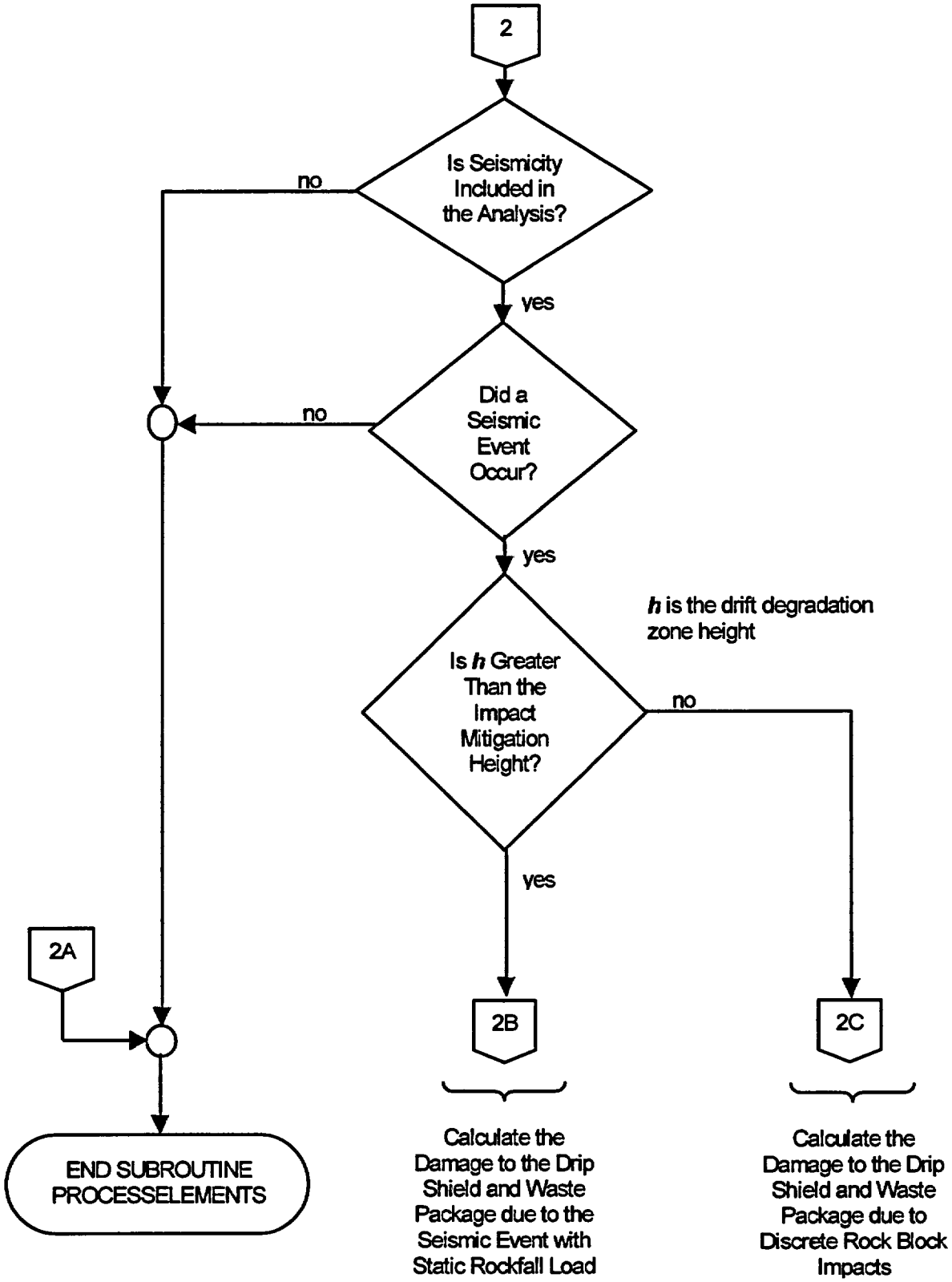

Figure 2-2. Flowchart of the PROCESSELEMENTS Subroutine (continued)

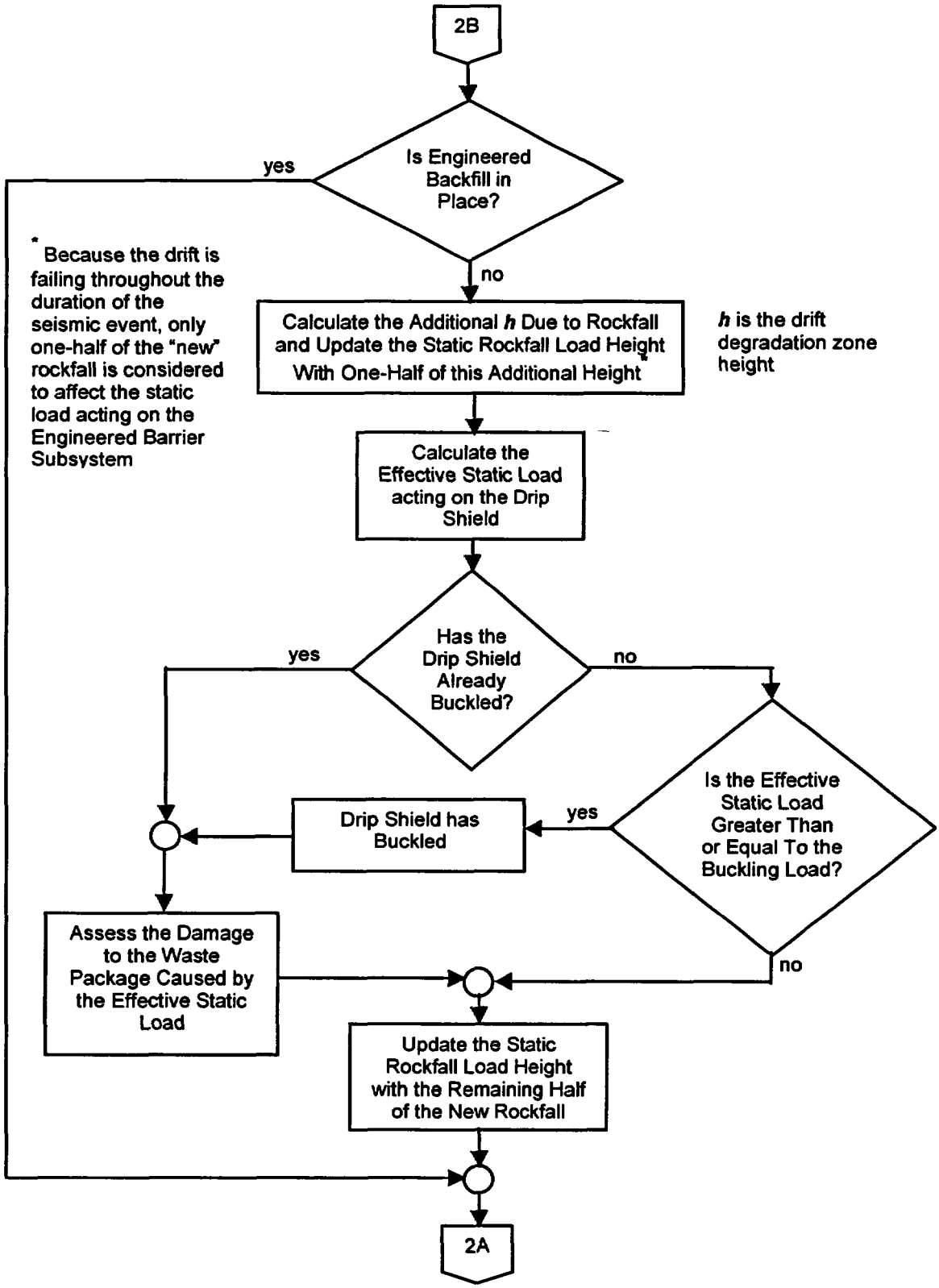

Figure 2-2. Flowchart of the PROCESSELEMENTS Subroutine (continued)

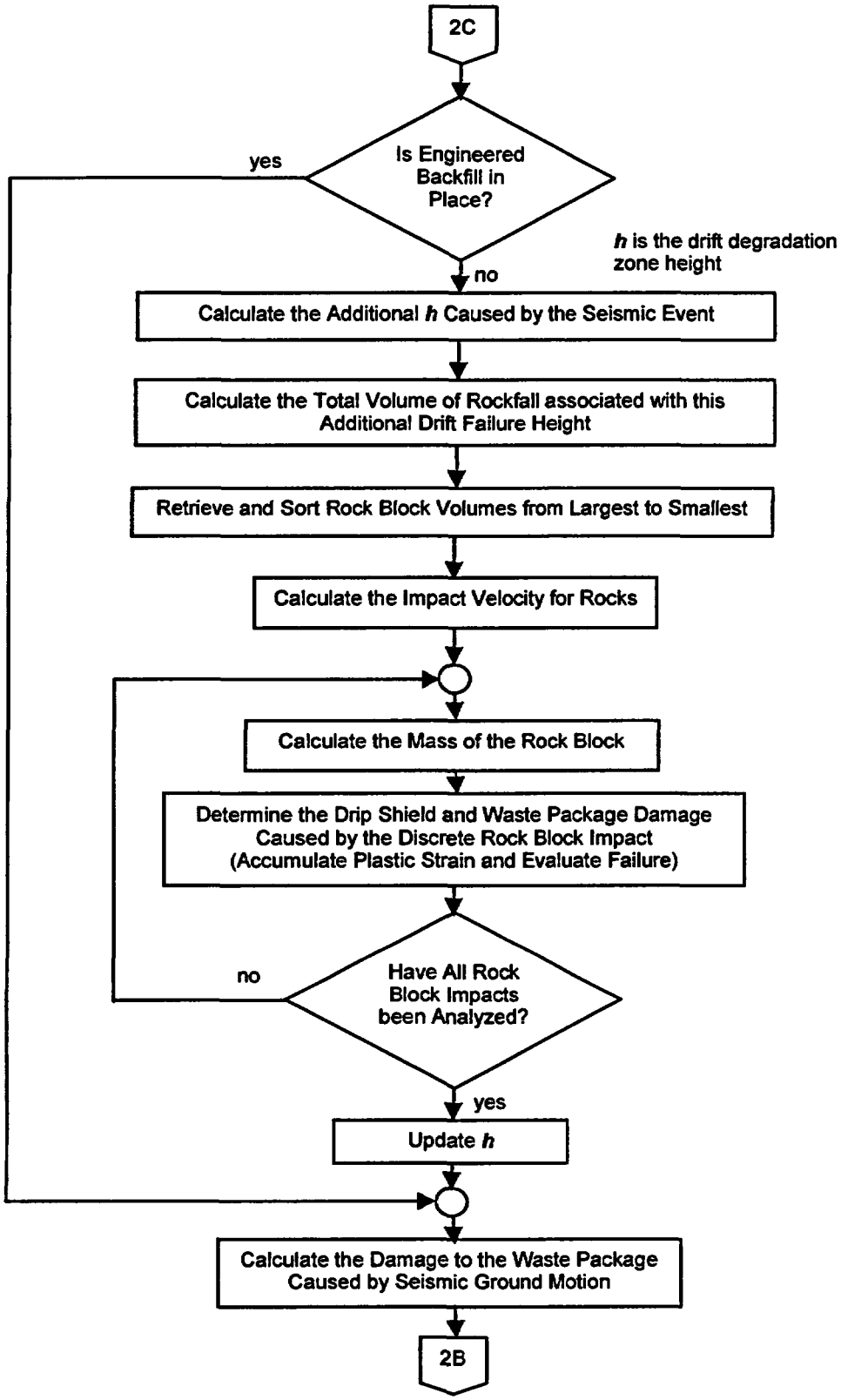

Figure 2-2. Flowchart of the PROCESSELEMENTS Subroutine (continued)

- The accumulation of rockfall rubble has been assumed to occur uniformly over the entire length of a drift, allowing the corresponding static rockfall loads to be derived on a per unit length basis (see Section 4.1.1).

- The drift degradation geometry has been assumed to have an elliptical profile (see Section 4.1.1).

- The resulting static load acting on the drip shield has been approximated by assuming the accumulated rockfall rubble exerts a continuous distribution of pressure over the surface of the drip shield crown (see Section 4.1.1). This assumption is based on the assessment that any bridging and arching of the accumulated rubble represents a metastable state of equilibrium that can be easily overcome by small particle rearrangements, such as may result from seismic shaking.

- The fracture bridge length and the gap between the edges of two adjacent coplanar fracture surfaces have been assumed in the rock block size distribution analysis because no data for these parameters are currently available (see Section 4.2.1). Fracture bridge length is normally a small value relative to the fracture trace length. If the fracture bridge length was assumed to be equal to zero, then a fracture could become persistent if variation in fracture spacing was not considered. Fracture bridge length somewhat controls the formation of blocks. Smaller values for bridge length improve the chance of a block forming.

- The fracture spacing, length, and bridge length were assumed to be uniformly distributed and varied ±30 percent about the mean values of the respective parameters when generating the three dimensional fracture patterns used for the rock block size distribution analysis (see Section 4.2.1).

- A fracture surface was assumed to be a square in shape with its characteristic length equal to the length of the corresponding fracture in the rock block size distribution analysis (see Section 4.2.1).

- Dynamic rock block impact loading has been assumed to occur during seismic events only (see Section 4.2.2). This simplifying assumption leads to the potential effects of any discrete rockfall impact loads caused by nonseismic processes being unaccounted for. Although rock blocks of sufficient size to cause appreciable dynamic impact to the drip shield can be expected at any time as a result of the various rock mass degradation processes described in Chapter 4, a satisfactory basis for how many, and when they may fall does not exist at this time.

- The effects of discrete rock blocks impacting the drip shield have been assumed to be mitigated once the accumulated amount of rockfall is sufficient to cover the drip shield crown under a 0.5-m [1.64-ft] depth of rock rubble. The rockfall caused by the occurrence of seismic events is still accounted for in the static rockfall loads after this threshold is met, however.

- The volume of rockfall caused by a seismic event was estimated using an assumed piece-wise linear relationship with the peak ground acceleration. The relationship is based on the precept that there is a threshold ground motion, g_o, needed to initiate

damage to a drift and a maximum ground motion, g_{max}, that would cause maximum damage to the drift. The maximum drift damage estimate is based on the conservation of mass principle.

- The static rockfall loads acting on the drip shield have been assumed to be symmetrically distributed over the drip shield surface. The response of the drip shield to an asymmetric buildup of accumulated rockfall rubble or natural load eccentricities, however, may be quite different than the scenario evaluated in this report. For example, the symmetric load and boundary conditions applied in the current model inherently preclude lateral (i.e., horizontal) deflections of the drip shield crown apex. Therefore, the current finite element model is expected to overestimate the structural capabilities of the drip shield when subjected to static rockfall loads because the lateral buckling mode has been artificially suppressed.

- The engineered barrier subsystem structure and component material temperatures have been assumed to be 150 °C [302 °F]. It has yet to be established that the assumed 150 °C [302 °F] material temperature adequately bounds the potential temperatures of the various engineered barrier subsystem component materials subjected to naturally backfilled conditions.

- The finite element model of the rock block was constructed using the following simplifying assumptions: (i) the rock block is a parallel-piped shape, (ii) the rock block impacts the apex of the drip shield crown with only a vertical component of velocity, and (iii) the rock block is sufficiently long to assume plane strain conditions. Assumption implies the rock block size should be interpreted as a mass-per-drip-shield segment length. For this study, the drip shield segment length was defined as the distance between two planes bisecting consecutive bulkhead and support beam structural stiffener pairs. The actual drip shield segment length is approximately 1.15 m [3.77 ft].

- To account for the ground motion associated with the seismic event assumed to be occurring at the same time as the dynamic rock block impact with the drip shield, the drip shield and invert were assumed to be moving at a constant upward velocity of 1 m/s [3.28 ft/s] at the time the impact was initiated. After impact, the invert foundation continued to move upward with a 1-m/s [3.28-ft/s] velocity throughout the duration of the analysis while the drip shield was free to respond to the rock block impact load.

- The rock block impacting the drip shield has been assumed to be fractured at the bulkhead. This assumption will create the shearing condition between the drip shield bulkhead and the drip shield crown plate that can be expected to occur after the rock block is crushed or fractured above the bulkhead. The shear stress calculated in the model should bound any potential shear stress that the drip shield may experience as the result of a rock block impact.

3 SEISMIC HAZARD CURVE ABSTRACTION

This chapter describes how the seismic hazard curve for Yucca Mountain is used to generate an evolution of seismic events and associated ground motion magnitudes within the Total-system Performance Assessment (TPA) code for the simulation period of interest. The result of the current sampling methodology is expected to be sufficient for assessing the potential effects of relatively high-probability ground motions. A different procedure will be developed for assessing the effects of the low-probability ground motions. The calculated evolution of seismic events is used as input to the analysis of dynamic rock block impacts and seismically induced rockfall, but has no effect on the calculation of accumulated rockfall resulting from nonseismic processes, as discussed in Chapter 4. The abstractions required to assess the response of the drip shield to seismic and nonseismic rockfall loads have been completed. The abstractions required to assess the response of the waste package to rockfall loads and direct seismic shaking are still being developed.

3.1 Seismic Hazard Curve

A seismic hazard curve relates the magnitude and frequency of occurrence (or return period) of the events. The seismic hazard curve used in the U.S. Nuclear Regulatory Commission (NRC) approach to total-system performance assessment is represented in terms of a relationship between the return period and the magnitude of the mean peak horizontal ground acceleration (Figure 3-1). This curve is a graphical representation of the mean peak horizontal ground acceleration hazard data provided by CRWMS M&O (1999d). These hazard curve data are based on probabilistic hazard analyses for fault displacement and vibratory ground motion at Yucca Mountain for a hypothetical rock outcrop reference location [i.e., Point 'A' as defined by the U.S. Geological Survey (1998)]. The seismic hazard curve presented in Figure 3-1 applies to this hypothetical location. Recent information presented by the U.S. Department of Energy (DOE)[1] indicates the subsurface repository horizon design basis ground motions are likely to be consistent with the hypothetical rock outcrop reference location ground motions attenuated by a factor somewhere in the range of 0.7 to 1.0, depending on the frequency range of interest. To ensure the potential effects of seismicity on repository performance are adequately captured in the TPA code, an attenuation factor of 1.0 is used. Moreover, the seismic hazard curve in the low annual frequency of exceedance regime (i.e., less than 10^{-6}/yr) has yet to be finalized.[2]

The sampled mean peak horizontal ground accelerations and the corresponding return periods (or recurrence time intervals) are provided as inputs to MECHFAIL. The continuous hazard curve is represented in the TPA code by a piece-wise step function based on 10 discrete intervals for the mean peak horizontal ground acceleration provided as input to the TPA code (see Table 3-1). The return periods for these ground motions are within the range of 142 to 100,000,000 years (i.e., a frequency of exceedance between 7.0643×10^{-3}/yr and 1.0×10^{-8}/yr). The piece-wise step function representation of the seismic hazard curve is implemented within the TPA code in the following manner. That is, once the return period

[1]DOE and NRC Public Meeting August 6–8, 2002. Las Vegas, Nevada. 2002.

[2]Stepp, C.C. and I.G. Wong. "Probabilistic Seismic Hazard Analysis for Yucca Mountain." Presentation to the Nuclear Waste Technical Review Board February 24, 2003. Las Vegas, Nevada: DOE. 2003.

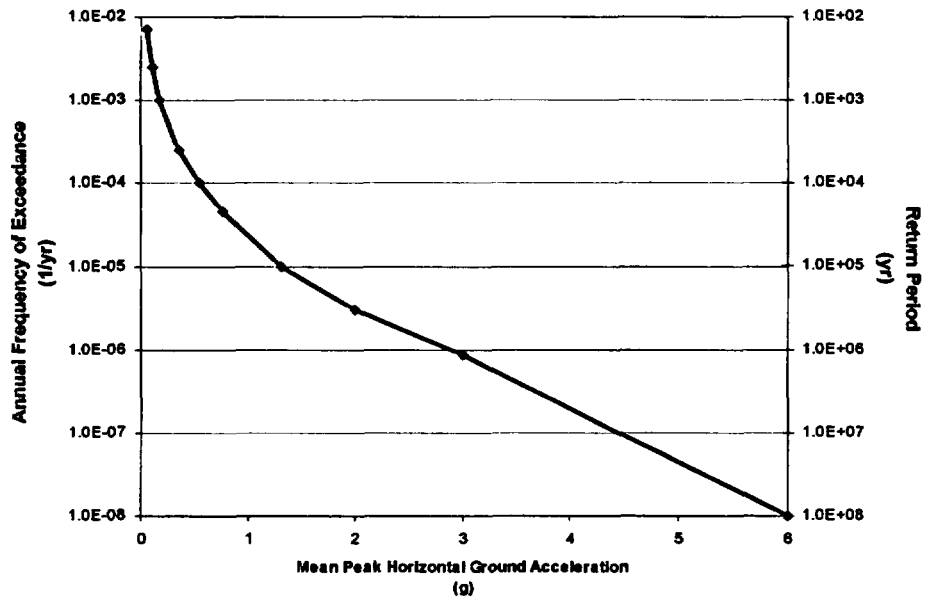

Figure 3-1. Seismic Hazard Curve Relating Annual Frequency of Exceedance and Return Period to Mean Peak Horizontal Ground Acceleration (See Table 3-1)

Table 3-1. Seismic Hazard Curve Data Input to the TPA Code	
Mean Peak Horizontal Ground Acceleration,* g	**Return Period,* yr**
0.050	142
0.100	409
0.169	1,000
0.350	3,968
0.534	10,000
0.750	22,340
1.305	100,000
2.000	336,261
3.00	1,158,062
6.00†	100,000,000†

*CRWMS M&O. "Seismic Ground Motion Hazard Inputs." WP–NEP–99309.T. MOL.19991005.0147. Las Vegas, Nevada: CRWMS M&O. 1999.
†DOE and NRC Public Meeting August 6–8, 2002. Las Vegas, Nevada. 2002.

(or recurrence interval) has been established by the applicable sampling process, the horizontal peak ground acceleration is assigned the value corresponding to the next longest return period included in the seismic hazard curve input table. For example, a seismic event with a return period of 4,000 years is assigned a horizontal peak ground acceleration of 0.534 g (see Table 3-1). Work is currently underway to determine if refinement of the seismic hazard curve interpolation will be appropriate.

3.2 Sampling of Event Time

The occurrence of seismic events is assumed to follow a Poisson process. When events occur according to a Poisson process, the time between occurrences (interarrival times) of the events has an exponential distribution. The mean recurrence time or return period for a simple Poisson process is $1/\nu$ where ν is the mean recurrence rate, that is the average number of occurrences of the event per unit time interval. In the basecase, the return period is 100 years, the fastest return period (i.e., the smallest recurrence interval). This return period means that on an average, once in 100 years a seismic event will occur (assuming that the Poisson process is a reasonable model for the occurrence of seismic events in the area). Event occurrence times and magnitude of the events are not correlated. In other words, large magnitude seismic events can occur at the same times as small magnitude events, but less frequently.

Figure 3-2 shows a histogram of sampled seismic event return periods in TPA code Version 5.0 beta from one Monte Carlo realization. As expected, the histogram is converging to an exponential distribution (i.e., increasing return periods with lower event frequency). A total of 53 seismic events were sampled during the 10,000-yr regulatory time period and 557 events in a 100,000-yr period. The position of the spikes in Figure 3-3 represent the times at which the sampled seismic events occurred in 100,000 years and the height of the spikes represent the sampled magnitudes of the mean peak horizontal ground acceleration of the individual events.

The assumptions inherent in this approach are the following:

- Any seismic event of a magnitude within the allowable range can occur at any time
- The occurrence(s) of an event in a given time interval is independent of that in any other nonoverlapping time interval
- The probability of occurrence of an event in a small interval, Δt, is proportional to Δt, and is given by $\nu\Delta t$ (assumed to be constant); and the probability of two or more occurrences in Δt is negligible.

3.3 Sampling of Seismic Event Magnitude

After the time of seismic events is established, then the event magnitude (in the case of the TPA code, expressed as the mean peak horizontal ground acceleration) is sampled according to the recurrence rate. First, the probability of occurrence of a given magnitude is computed. Then, corresponding to each seismic event time, a mean peak horizontal ground acceleration value is sampled according to its recurrence probability.

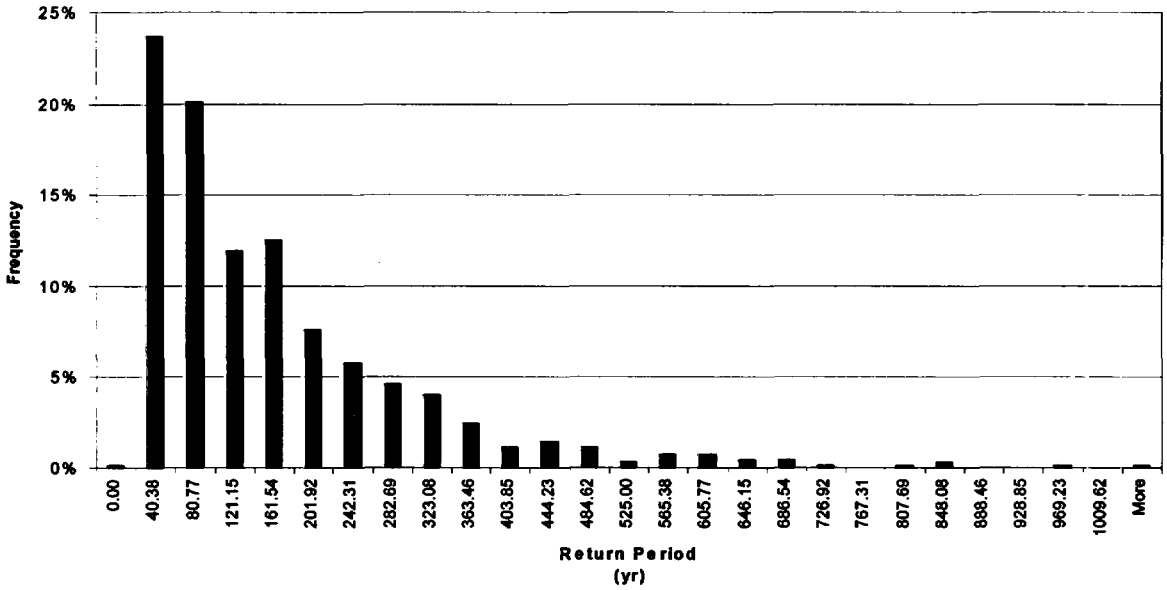

Figure 3-2. Histogram Showing Convergence to Exponentially Distributed Samples of Return Periods for a Single Realization of 100,000 Years (See Figure 3-3)

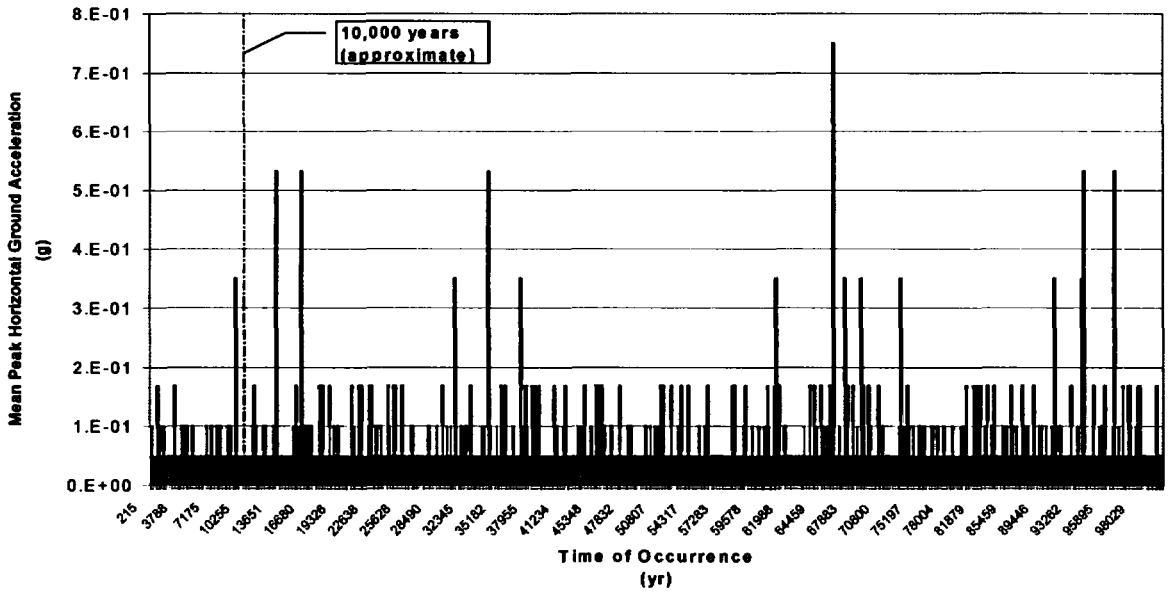

Figure 3-3. Sampled Values of Mean Peak Horizontal Ground Acceleration as a Function of Time for a Single Realization of 100,000 Years (Each Vertical Bar Represents One Seismic Event)

4 APPROXIMATION OF ROCKFALL LOAD MAGNITUDES AND PROBABILITIES

The following discussion conveys the methodologies used to establish the magnitude of static and dynamic rockfall loads likely to occur within the emplacement drifts of the proposed geologic repository. Static rockfall loads are created by the accumulation of rockfall rubble through time as the structural integrity of the drifts degrade from the combined effects of thermal, mechanical, hydrological, and chemical processes. Dynamic rockfall loads occur when individual, discrete rock blocks become dislodged from the drift roof and free fall, because of the influence of gravity, to impact either the drip shield or waste package. At the present time, it is assumed that dynamic rock block impact loading may result only from seismically induced rockfall (see Section 4.2.2). This simplifying assumption leads to the potential effects of any discrete rockfall impact loads caused by nonseismic processes being unaccounted for.

Rockfall and the associated degradation of excavated underground openings are expected as a natural response of the openings to the excavation-induced changes in the mechanical conditions within the surrounding rock mass. Underground openings are, for this reason, usually provided with adequate ground support, with a sufficient maintenance schedule, to ensure the stability of the openings through the required service life. The proposed emplacement drifts at Yucca Mountain can be expected to be provided with adequate ground support and maintenance during the preclosure operational period, but the drift openings are anticipated to degrade and experience rockfall at various rates during the postclosure period. The drifts are anticipated to degrade through progressive fracture growth and slip of existing fractures and larger-scale discontinuities (e.g., faults and bedding planes) in response to mechanical forces caused by changes in temperature, fluid pressure, and rock stress resulting from the repository excavation and thermal loading. The degradation may also be aided by rock weakening from geochemical alteration processes such as reviewed in Ofoegbu (2000) and may be triggered or accelerated by seismicity.

Previous analyses performed to assess the preclosure stability of the proposed emplacement drifts (Ahola, et al., 1996; Ofoegbu, 1999, 2000, 2001; Hsiung, et al., 2001; NRC, 2002; Bechtel SAIC Company, LLC, 2003) indicate that a ground support system and adequate maintenance of the system would be needed to mitigate rockfall and drift degradation during the preclosure period. As discussed in NRC (2002, pp. 2.1.7-10–2.1.7-12), the stress conditions caused by thermal loading would favor the development of potential zones of rock failure by fracture slip through a reverse-faulting mechanism in the roof and floor areas of the drifts and in the pillars, and strike-slip or normal-faulting mechanisms in the drift sidewall areas. Any slip surfaces formed through these mechanisms would constitute potential release surfaces for rock blocks. A degraded ground support system may be able to restrain such blocks in an essentially metastable state until the blocks are released (i.e., rockfall and drift degradation) by a triggering event, such as seismicity.

Drift degradation, therefore, is controlled by the coupled and time-dependent gradients of temperature, fluid pressure, rock stress, and chemical composition of the interacting fluids and minerals (e.g., see literature review in Manteufel, et al., 1993; Ofoegbu, 1999, 2000). Development of a rigorous mathematical model of these coupled processes that accurately simulates the degradation process for the 10,000-yr period of regulatory concern has proven elusive because of the complexity of modeling these coupled processes. The lack of information for developing such a model, despite the long history of mining, transportation, and

several other applications of underground excavations, also can be attributed to the fact that the engineering of underground space has historically focused on excavating openings required to remain stable for relatively short periods of time as compared to the period of interest for the proposed repository. As a result, the characterization of the potential instability of underground openings is typically not undertaken. Available records on abandoned underground excavations, such as the several tunnels constructed at the Nevada Test Site as part of the weapons program (e.g., U.S. Geological Survey, 1982; Wong, et al., 1991), may provide useful information on drift degradation rates.

Several abstractions are described in this chapter for calculating the quantities used for the characterization of drift degradation, rockfall, and the associated mechanical loading of the engineered barrier subsystem components. An approach for calculating the degradation-zone extent and the amount of associated rockfall rubble, which is based on a mass balance between the rock mass surrounding the opening and the rockfall rubble formed as a result of the degradation of the rock mass is described in Section 4.1. In the mass-balance approach, the bulking behavior of broken rock is used to develop a relationship between the rock volumes for the *in-situ* and rubbled states, which results in an expression for the maximum degradation-zone volume. The approach for calculating seismically induced rock block impact loads is described in Section 4.2. The inputs to the approach are (i) rock block size distributions calculated based on a statistical analysis of the site fracture data and (ii) an empirical relationship between ground acceleration and observed earthquake-induced damage to underground openings.

For the current engineered barrier subsystem design, the waste package may be exposed to direct rockfall loads only during the preclosure operational period. After emplacement of the drip shields, the waste packages may be affected by rockfall only indirectly by way of potential interactions with the drip shield. Any rockfall loading during the postclosure period, therefore, would be applied to the drip shield. Such loading may be transferred to the waste package as described in Chapters 6 and 7. The approach for calculating the drip shield loading is described in this chapter.

4.1 Characterization of Accumulated Rockfall Static Loads

The mass balance between the *in-situ* state of the rock surrounding an opening and the rubble formed after the rock breaks up and falls into the opening results in the following equation

$$b_f V_o = V_f \tag{4-1}$$

where V_o is the *in-situ* rock volume and V_f is the volume of fallen rock rubble. The bulking factor b_f is the ratio ρ_o/ρ_{eff}, where ρ_o is the *in-situ* bulk density of the rock and ρ_{eff} is the effective density of the rubble. The bulking factor accounts for the increase in volume of the rock mass after it has become fractured and broken into rubble. The mass balance approach based on the bulking behavior of rock is commonly used to calculate the potential caving height of the overburden material above a mined opening (e.g., Peng and Chiang, 1984, pp. 18–30).

The value of bulking factor for a rock is controlled by several factors, including the size, shape, and distribution of the rock particles; the shape of the receiving surface in a rockfall event; the rate of rockfall; and the stress condition within the rubble (cf., Peng and Chiang, 1984, p. 29). In

general, relatively hard and competent rocks that break into large blocks have larger bulking factors than weak or soil-like rocks that break into fine particles (e.g., Table 4-1). Laboratory data presented by Fayol (in Peng and Chiang, 1984, p. 30) illustrate that bulking factor generally increases with particle size but decreases with increasing pressure. The decrease of bulking factor with increasing pressure occurs because of compaction and may cause the value of bulking factor for a given rubble deposit to decrease with increasing age and depth within the deposit. Peng and Chiang (1984, p. 30), for example, presented data illustrating a significant decrease in bulking factor from an initial value representing negligible compaction, such as may be expected near the top of a rubble deposit, to a residual value representing an advanced stage of compaction (Table 4-2). The values of bulking factor representing the advanced stage of compaction, referred to as the residual bulking factor in Table 4-2, are more appropriate for calculating the long-term equilibrium conditions in a rubble deposit. Any occurrence of bridging or arching within the deposit would tend to decrease the effectiveness of compaction and, therefore, increase the bulking factor. Bridging and arching, however, are metastable conditions that cannot be relied upon in estimating the long-term equilibrium state in rock rubble. Such processes are highly dependent on localized interparticle stress conditions that can be changed drastically by a small amount of particle rearrangement, such as may result from seismic shaking. The occurrence of horizontal stratification in the rock mass can significantly decrease the bulking factor. A field study of caving in several Indian coal mines (Das, 2000), for example, indicated a value of bulking factor of 1.05 or less for the collapsed coal-measure strata (i.e., a sequence of sandstone and shale with clay intercalations). The study examined the failure of longwall panels in coal mines, and it appears that the overburdened rock collapsed essentially as a homogeneous plug in several cases.

The authors are not aware of bulking factor data for any of the rock units at the Yucca Mountain repository site. The values of bulking factor implemented in the current version of MECHFAIL were selected based on several considerations. First, based on the authors' mining engineering experience, the bulking factor for broken rock is rarely assigned a value larger than approximately 1.25–1.35, which is consistent with the values of residual bulking factor in Table 4-2. Second, the values of bulking factor for the lithophysal rock units are expected to be smaller, generally, than the values for the nonlithophysal units. The lithophysal rocks are generally weaker and softer, have smaller fracture spacing, and, therefore, would break into smaller fragments as compared with the nonlithophysal rocks. Furthermore, the lithophysal cavities range in size from approximately 0.01–1.0 m [0.033–3.28 ft][1] and will tend to reduce the bulking factor if some of the broken-rock particles are smaller than some of the cavities. Based on these considerations, the nonlithophysal units are assigned bulking factors in the range of 1.35–1.5, and the lithophysal units in the range of 1.15–1.5. Uniform distributions are used to define the variability of the bulking factor within the specified ranges for the two rock types. As shown in Section 4.1.1, the potential magnitude of the static rockfall load varies significantly for bulking factors within the range of 1.1–1.5. Smaller bulking factors result in higher static rockfall loads. Further analysis of Yucca Mountain specific data may result in a refined range of values for the bulking factor of the two rock units.

[1]Sweetkind, D.S., S.C. Beason, and D.C. Buesch. "Overview of the Stratigraphy and Structural Setting of Yucca Mountain, Nevada, USA." *Paper submitted to International Journal of Rock Mechanics and Mining Sciences and Geomechanics Abstracts*. In press. 2002.

Table 4-1. Bulking Factors for Common Soils and Rock Types	
Material	**Bulking Factor***
Clay (Low Plasticity Index)	1.30
Clay (High Plasticity Index)	1.40
Clay and Gravel	1.35
Sand	1.05
Sand and Gravel	1.15
Gravel	1.05
Chalk	1.50
Shales	1.50
Limestone	1.63
Sandstone (Porous)	1.60
Sandstone (Cemented)	1.61
Basalt	1.64
Granite	1.72

*Wilkinson, D. "Earthworks." *Road Design*. MEng final year project report. University of Durham, School of Engineering. Durham, United Kingdom. 1997. <http://www.dur.ac.uk/~des0www4/cal/roads/earthwk/earthwk.html> (April 25, 2003).

Table 4-2. Values of Bulking Factor for Various Coal Measure Rocks*		
	Bulking Factor	
Rock Type	**Original, b_{fo}**	**Residual, b_{fr}**
Sand	1.06–1.15	1.01–1.03
Clay	< 1.20	1.03–1.07
Broken coal	< 1.30	1.05
Clay Shale	1.40	1.10
Sandy shale	1.60–1.80	1.25–1.35
Sandstone	1.50–1.80	1.30–1.35

*Peng, S.S. and H.S. Chiang. *Longwall Mining*. New York City, New York: John Wiley and Sons. 1984.

4.1.1 Accumulated Rockfall Static Load Distribution

The magnitude of static rockfall loads is controlled by the mass of rockfall rubble that accumulates on top of the drip shield. Any occurrence of arching within the rubble would reduce the load transmitted to the drip shield. As explained previously, arching or bridging, however, results from a metastable condition and, consequently, cannot be relied upon in estimating the long-term equilibrium state in rock rubble. Any effects of arching, therefore, are not included in the abstractions for the static rockfall loads. The limiting amount of rockfall rubble supported by the drip shield can be determined by calculating the volume of rock needed to fill the combined volume of the initial drift void space and the new void space created by rockfall and accounting for the effect of bulking [see (Eq. 4-2)]. Note the similarities between Eqs. (4-1) and (4-2).

$$b_f V_o = \left(V_o + V_d\right) \tag{4-2}$$

where

b_f	—	bulking factor
V_o	—	drift degradation zone volume
V_d	—	drift void volume
$V_o + V_d$	—	volume of fallen rock rubble, V_f [see Eq. (4-1)]

Assuming this behavior occurs uniformly over the entire length of a drift, the loads can be derived on a per unit length basis. Moreover, the mathematical relationships can be written on a cross-sectional area basis as opposed to a volumetric basis [see Eq. (4-3)]. A graphical representation of Eq. (4-3) is provided in Figure 4-1.

$$b_f A_o = \left(A_o + A_d\right) \tag{4-3}$$

where

A_o	—	cross-sectional area of the drift degradation zone
A_d	—	drift void cross-sectional area
$A_o + A_d$	—	cross-sectional area of the fallen rock rubble, A_f

Because the drift void cross section can be readily estimated from available information (CRWMS M&O, 2000a), the key to the problem is establishing a reasonable approximation of the geometry for the cross-sectional area of the drift degradation zone. Three different geometries for A_o were investigated to determine the relative effects of this choice on the limiting static rockfall load. These assumed areas will be referred to as the trapezoidal (see Figure 4-2a), triangular (see Figure 4-2b), and elliptical (see Figure 4-2c) drift degradation geometries. It is important to observe that the triangular and elliptical cross-sectional areas have a single unique solution for A_o for a given bulking factor. A unique solution for A_o also establishes a unique solution for the limiting static rockfall load (i.e., for a given bulking factor). The trapezoidal drift degradation geometry, on the other hand, requires an additional parameter,

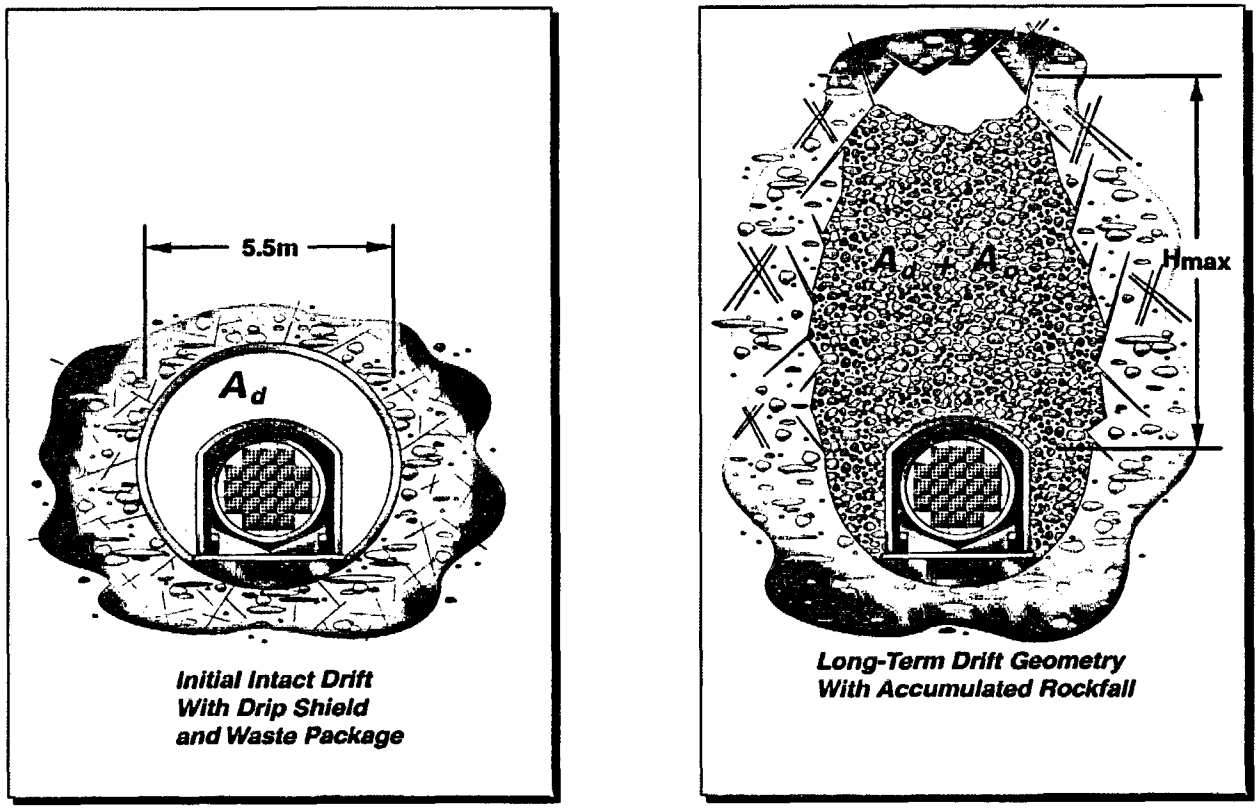

Figure 4-1. Illustration of the Drift Void and Drift Degradation Zone Area Parameters

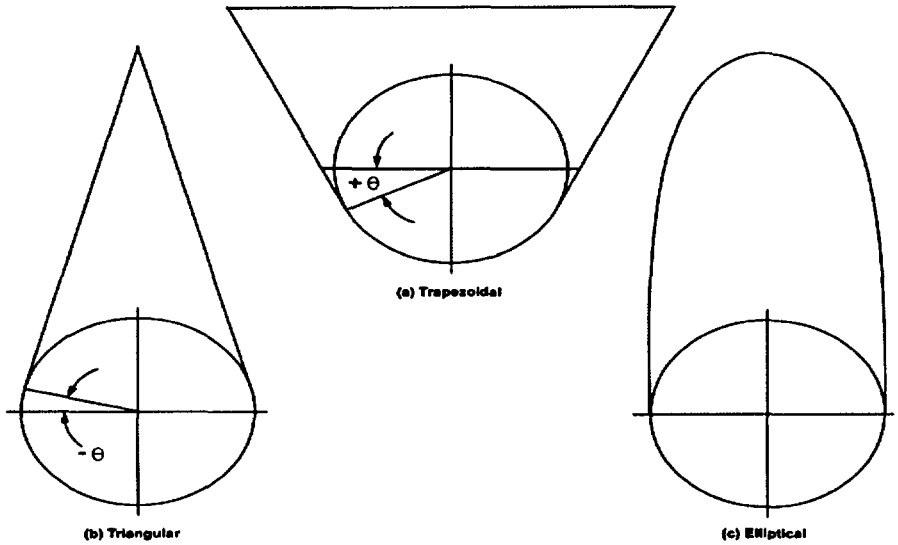

Figure 4-2. Potential Drift Degradation Geometries

θ, which is defined in Figure 4-2a, to determine the magnitude of the static rockfall load acting on the drip shield.

After A_o has been determined, the resulting load acting on the drip shield can be approximated by assuming the rockfall rubble exerts a continuous distribution of pressure over the surface of the drip shield crown. The distribution of the pressure acting on the drip shield is approximated by Eq. (4-4). Figure 4-3 illustrates the variables used in Eq. (4-4).

$$P(x) \cong \rho_{eff} g h(x) \tag{4-4}$$

where

x	—	variable defining the transverse distance from the drip shield crown center
$P(x)$	—	rock rubble pressure at x from the drip shield crown
ρ_o	—	*in-situ* rock-mass density
ρ_{eff}	—	effective density of the rock rubble
g	—	gravitational acceleration
$h(x)$	—	rock rubble height at x from the drip shield crown

The value of ρ_o is set to 2,250 kg/m^3 [140 lb/ft^3] for the lithophysal and nonlithophysal rocks based on CRWMS M&O (1997a). The effective density of the rock rubble, ρ_{eff}, required in Eq. (4-4) is determined using the conservation of mass principle. Specifically,

$$\rho_o V_o = \rho_{eff} V_f \tag{4-5}$$

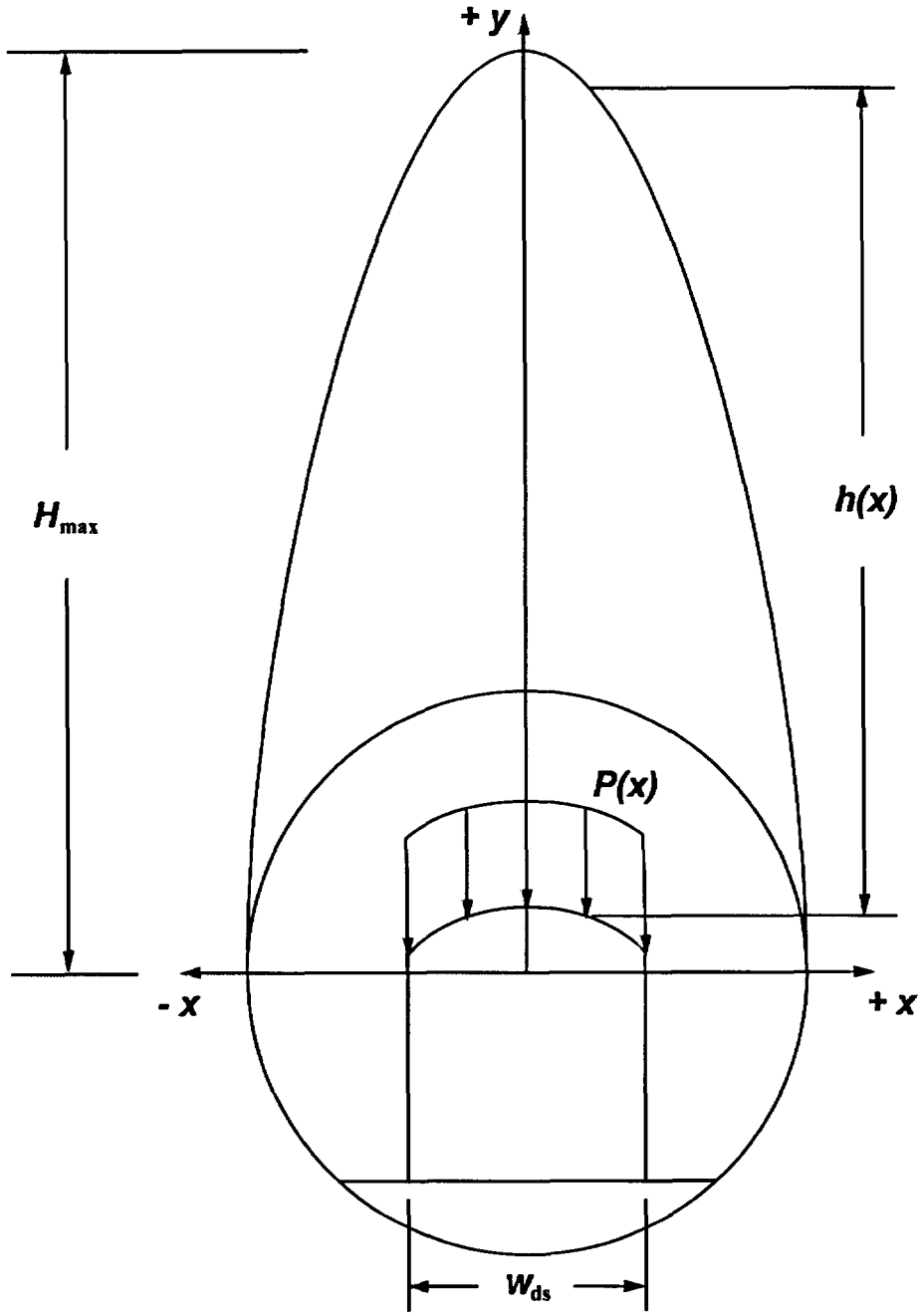

Figure 4-3. Parameters Used to Approximate Drip Shield Crown Pressure Loads

Solving Eq. (4-5) for ρ_{eff} gives

$$\rho_{eff} = \rho_o \frac{V_o}{V_f} \tag{4-6}$$

Using Eq. (4-1), Eq. (4-6) can be recast as

$$\rho_{eff} = \frac{\rho_o}{b_f} \tag{4-7}$$

The resultant static rockfall load acting on the drip shield crown, per unit length, is obtained by integrating Eq. (4-4) over the width of the drip shield [see (Eq. 4-8)].

$$\begin{aligned} \frac{F}{L} &= \int_{-\frac{w_{ds}}{2}}^{+\frac{w_{ds}}{2}} P(x)\, dx \\ &= 2\int_0^{+\frac{w_{ds}}{2}} P(x)\, dx \\ &= 2\frac{\rho_o g}{b_f}\int_0^{+\frac{w_{ds}}{2}} h(x)\, dx \end{aligned} \tag{4-8}$$

where

w_{ds} — drip shield width

Figure 4-4 plots the resultant static rockfall load acting on the drip shield for the trapezoidal and triangular drift degradation geometries for varying values of the bulking factor. As pointed out earlier, the trapezoidal drift degradation geometry requires an additional parameter, θ, to determine the magnitude of the static rockfall load acting on the drip shield. Therefore, the effects of θ on the resultant static rockfall load acting on the drip shield for variations of the trapezoidal drift degradation geometry are represented by the positive values of this parameter in Figure 4-4. The unique limiting static rockfall loads for the triangular drift degradation geometry for varying values of the bulking factor are also plotted in Figure 4-4. The unique solution for the limiting static rockfall load using the triangular drift degradation geometry is plotted in terms of its unique negative value of θ.

Figure 4-5 is a plot of the limiting static rockfall loads for the elliptical drift degradation geometry and varying values of the bulking factor. Figure 4-6 is a plot of the corresponding maximum elliptical drift degradation zone height as a function of the bulking factor.

As can be seen from Figures 4-4 and 4-5, the limiting static rockfall loads for the trapezoidal drift degradation geometry are significantly smaller than those for the triangular and elliptical versions. Experience with mining-induced caving (e.g., Brady and Brown, 1985) indicates that the elliptical geometry is more likely than either the trapezoidal or triangular geometries if the host rock is homogeneous and rockfall is controlled by mechanical processes. The elliptical drift-degradation geometry, which is often described as chimney caving in mining engineering, is associated with two types of homogeneous rock conditions: (i) soils or weak rocks, such as sand, clay, weak shale, sandstone, chalk, or similar materials; and (ii) a regularly jointed rock mass, in which rockfall is controlled by the unraveling of the discontinuities. In such rock-mass conditions, rockfall in an unsupported opening may lead to the formation of a chimney-shaped

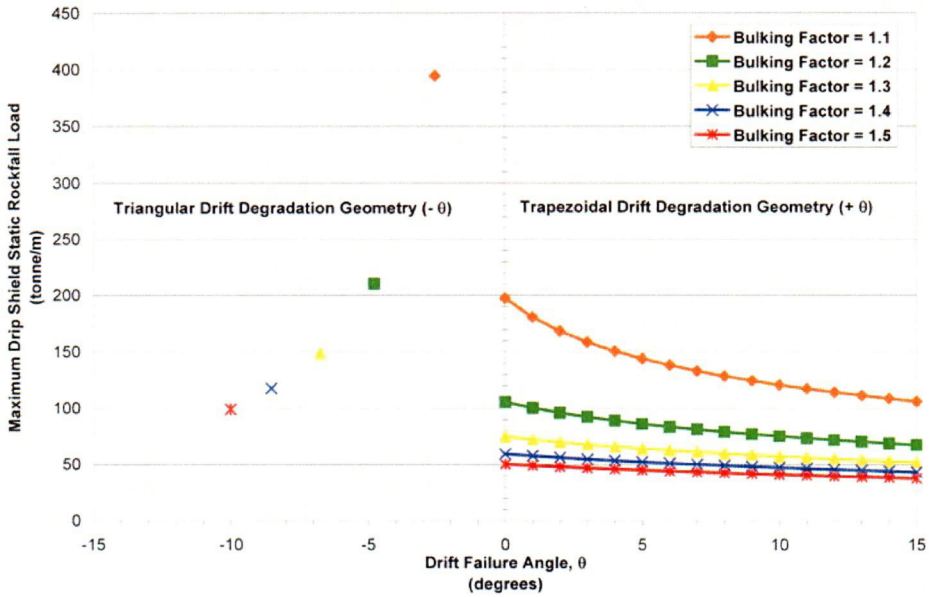

Figure 4-4. Maximum Static Rockfall Load Acting on the Drip Shield Crown for the Trapezoidal (+ θ) and Triangular (– θ) Drift Degradation Geometries for Different Bulking Factors

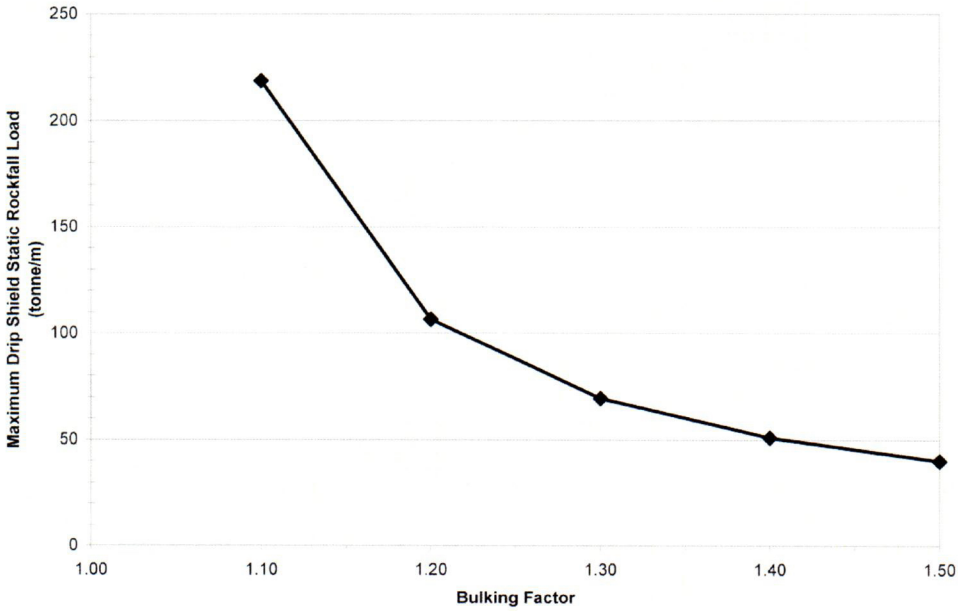

Figure 4-5. Maximum Drip Shield Static Rockfall Load as a Function of the Bulking Factor for the Elliptical Drift Degradation Geometry

C01

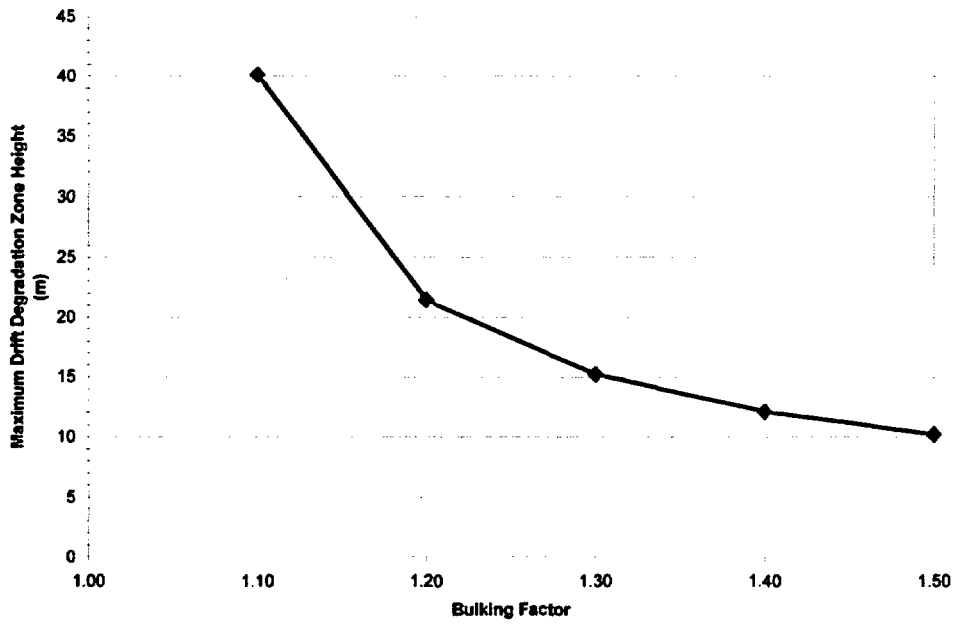

Figure 4-6. Maximum Drift Degradation Zone Height as a Function of the Bulking Factor for the Elliptical Drift Degradation Geometry

degradation zone. The height of such a degradation zone is controlled by the bulking characteristics of the rock. The lower lithophysal rock is similar to a weakly cemented sandstone, based on observations of rockfall characteristics in a recently completed exploratory drift at Yucca Mountain and on information provided by the U.S. Department of Energy (DOE) staff. Also, the middle nonlithophysal unit is known to be regularly jointed, having three regular sets and one random set of joints (CRWMS M&O, 2000b). These two rock units, therefore, belong to the class of rock masses for which caving is likely to follow the elliptical geometry.

The long-term configuration of an emplacement drift and the associated static rockfall load have been determined using a mass-balance analysis in which the height of the drift-degradation zone is controlled by the bulking behavior of the rock. The mass-balance approach does not consider the forces and material resistance that control rockfall, but is based on the principle that rockfall would occur if, and only if, the available space can accommodate the rubble formed from the rockfall until completely backfilled. An alternative approach based on a limit-equilibrium analysis is now presented to further explore the potential variability of the drift-degradation zone height.

The limit-equilibrium analysis is based on a procedure widely used to evaluate the potential for chimney caving above underground mines (Brady and Brown, 1985). Consider, for example, the static equilibrium of a rectangular block of rock above an emplacement drift. The base of the block is at the same elevation as the drift spring line. The width of the block is the same as the drift diameter, D. The length, L, of the block (along the drift axis) is arbitrary; however, L is set equal to D for the analysis. The block extends to the ground surface, but a section of the block up to a height, h, above the drift roof may fall as determined by the static equilibrium conditions. Therefore, h represents the height of the degradation zone. The equilibrium of the

potentially unstable block is controlled by the weight, the overburden pressure on the top surface, and the shear resistance on the four vertical boundary surfaces of the block.

It can be shown by summing these forces to zero, representing the limit-equilibrium condition, that the height of the degradation zone is given by the equation

$$h = z + \frac{c}{\mu K \gamma} - \left[\left(z + \frac{c}{\mu K \gamma}\right)^2 - \frac{Dz}{2\mu K}\right]^{1/2} \tag{4-9}$$

where γ, μ, and c are the average unit weight, friction coefficient, and cohesion parameters for the rock mass; z is the depth of the drift axis below the ground surface; and K is the horizontal-to-vertical stress ratio. The following parameter values were used for the analysis: D = 5.5 m [18.0 ft], z = 300 m [984 ft], γ = 0.025 MN/m^3 [159 lb/ft^3], and μ = 0.8 (which is equivalent to a friction angle of approximately 40 degrees). The results calculated using Eq. (4-9) are shown in Figure 4-7, which illustrates the variation of the potential drift degradation zone height as c and K are varied.

The decrease in K to near-zero values represents a change that would occur during a seismic event. Such changes in K, therefore, help explore how an equilibrium configuration calculated for static conditions may change during a seismic event. The range of c values used in the analysis was chosen to explore the behavior of the fractured rock mass when subjected to the near-zero confining pressures implied by the low K values. A fractured rock mass has no significant intrinsic cohesion. The strength-envelope for such a rock, however, is curved such that a straight-line fit to the strength envelope for relatively high confining-stress conditions would give a significant nonzero value for the c parameter (e.g., Hoek and Brown, 1997; Figure 6). Such c values, however, are not appropriate for analyzing the behavior of the rock when subjected to low confining stress conditions, such as may occur during a seismic event as represented by the low K values in Figure 4-7. The behavior obtained using a rock-mass cohesion of 0.1 MPa [14.5 psi], therefore, represents the expected behavior of a fractured rock mass better than the relationships obtained using the higher cohesion values.

As Figure 4-7 shows, the drift degradation zone height obtained for static (i.e., K = 0.2) conditions using the limit-equilibrium analysis is smaller than the drift degradation zone height obtained from the mass-balance calculation. The limit-equilibrium analysis, however, gives an increasing drift degradation zone height as K decreases (using a small value of c appropriate for low K conditions) and predicts an ultimate equilibrium configuration with a degradation zone that is more extensive than the degradation zone calculated based on the mass-balance approach. The mass-balance approach indicates that the degradation zone would extend to a maximum height of 40 m [131.2 ft] for the smallest value of bulking factor used in this report, whereas the limit-equilibrium analysis predicts a maximum height of approximately 100 m [328 ft]. The limit-equilibrium approach may overestimate the drift degradation zone height because the self-equilibration mechanism provided by the bulking behavior of the rock is not accounted for in the analysis. This analysis indicates that the height obtained through the mass-balance approach is a reliable limiting estimate of the potential drift degradation zone height, dependent only on the value of bulking factor used for the analysis.

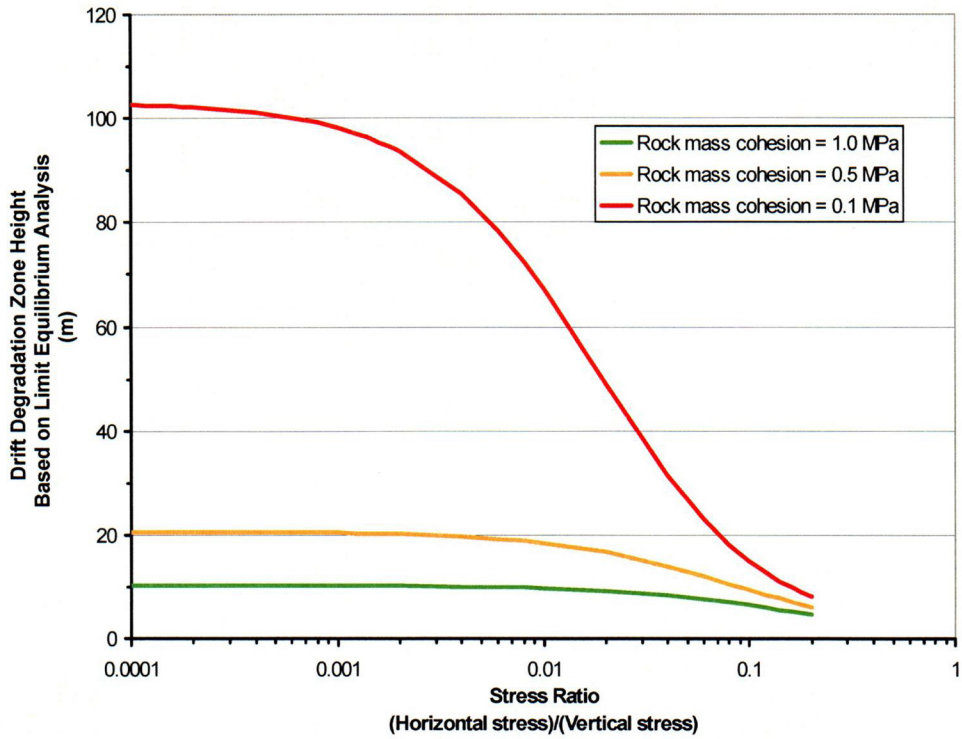

Figure 4-7. Variations of the Height of a Potential Drift-Degradation Zone Based on a Limit-Equilibrium Analysis of Chimney Caving Above an Emplacement Drift

4.1.2 Accumulated Rockfall Static Load Abstraction

The following discussion describes the rationale and methodology used to determine the rates of drift degradation resulting from nonseismic (thermal, mechanical, hydrological, and chemical) processes in the Total-system Performance Assessment (TPA) code.

As described in Chapter 2, the repository footprint is represented by 20 spatial grid elements, with two grid elements assigned to each of the 10 subareas used within the TPA code. One of the grid elements represents the percentage of the given subarea that is in the lower lithophysal rock unit and the other grid element represents the remaining percentage of the middle nonlithophysal rock unit. Each grid element is assigned a bulking factor from the range of possible bulking factors for that particular rock unit. A uniform distribution of the bulking factor is used for this purpose. After a bulking factor has been assigned to a given grid element, the maximum drift degradation zone height can, in turn, be estimated.

C02

An abstraction of the long-term configurations of the emplacement drifts and the accumulated rockfall static loads has been developed based on the bulking behavior of rocks. To develop an abstraction of the drift degradation rate (i.e., the rate of change of the drift geometry from the initial to long-term configurations as illustrated in Figure 4-1), it is necessary to consider (i) the anticipated stand-up time for an unsupported opening in fractured rock typically varies from a few hours in poor-quality rocks to a few months in good-quality rocks (cf., Hoek and Brown, 1980) and (ii) the ground support system for the emplacement drifts can be expected to be monitored and maintained through the preclosure period but not thereafter.

The stand-up time for an unsupported opening is the time period from the initial excavation to the onset of drift instability, which is manifested by the formation of new fractures, propagation of existing fractures, and rockfall. As can be seen in Figure 4-8, the allowable unsupported span (e.g., tunnel length) of an underground opening can be estimated using the rock mass quality index. This information is further augmented by the estimated ranges of stand-up time for different rock mass quality indices and unsupported span lengths (see Figure 4-9). The rock mass quality classification for the repository host rock lies in the range of fair rock through good rock (CRWMS M&O, 1997b). The expected stand-up time for unsupported openings in such rocks is on the order of days and months.

The ground support system cannot be relied on to remain effective for more than a few tens of years following the cessation of maintenance. The emplacement drifts, therefore, should be considered as unsupported openings after a few tens of years following the cessation of maintenance, and, considering the information in Figures 4-8 and 4-9, the anticipated stand-up time for the openings thereafter would not exceed a few years. Considering this argument and the associated uncertainties, it is reasonable to expect the emplacement drifts to fully backfill themselves (i.e., attain the anticipated long-term configuration illustrated in Figure 4-1) within a relatively short time following the cessation of maintenance.

A quantitative interpretation of "relatively short time" is needed to provide a probability distribution of the degradation rates for performance assessment calculations. Considering that the ground support system can be expected to remain effective for as long as 100 years (i.e., on the order of tens of years) following the cessation of maintenance, the anticipated postclosure stand-up time for the drifts should be at least 100 years. The anticipated self-backfilling time for the drifts, therefore, should be on the order of a few hundred years (i.e., greater than 100 but less than 1,000 years). A beta distribution based on this interpretation has been developed for assigning the time required for the drifts to backfill themselves completely to the maximum drift degradation zone height (see Figure 4-10). Each spatial grid element is assigned a unique self-backfilling time, ranging from a minimum of 250 years to a maximum of 1,000 years. An improvement of the abstraction may be achieved if reliable records on abandoned underground openings can be found, but the maximum self-backfilling time is not expected to exceed a few hundred years.

Because the maximum drift degradation zone height and the time required to achieve this level of degradation have been defined for each spatial grid element, the rate of drift degradation can be calculated on a per-grid element basis. The rate of drift degradation within the MECHFAIL module is characterized by the rate of change of the major elliptical axis (i.e., drift degradation height) of the drift degradation zone with respect to time.

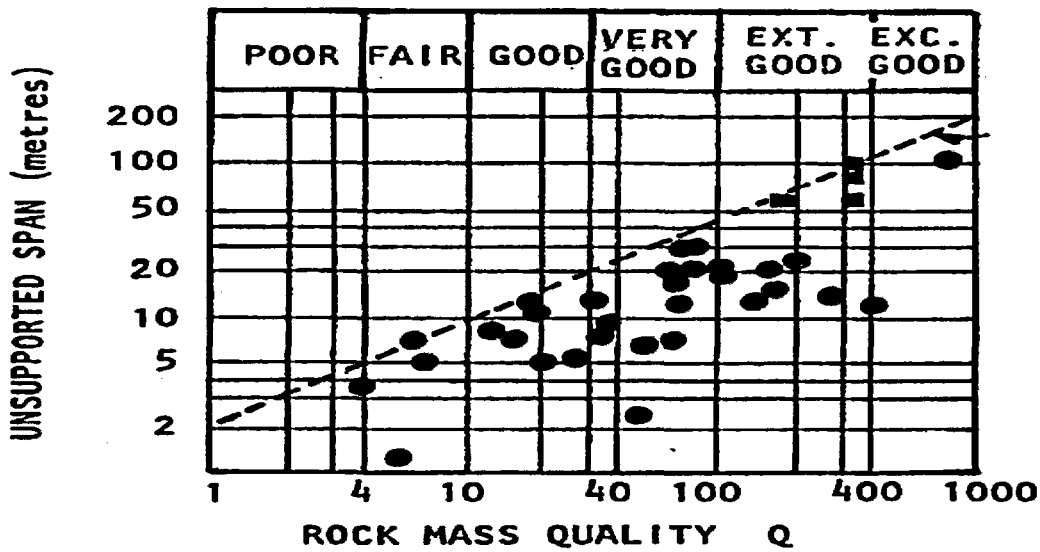

Figure 4-8. Allowable Unsupported Span as a Function of Rock Mass Quality (Hoek, and Brown, 1980)

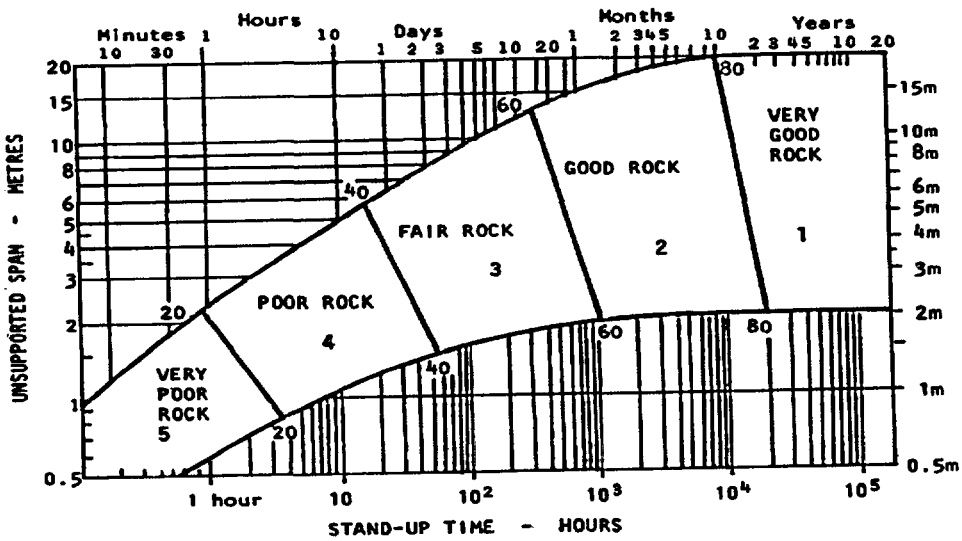

Figure 4-9. Estimated Ranges of Drift Stand-up Time for Different Rock Mass Quality Indices and Unsupported Span Lengths (Bieniawski, in Hoek and Brown, 1980)

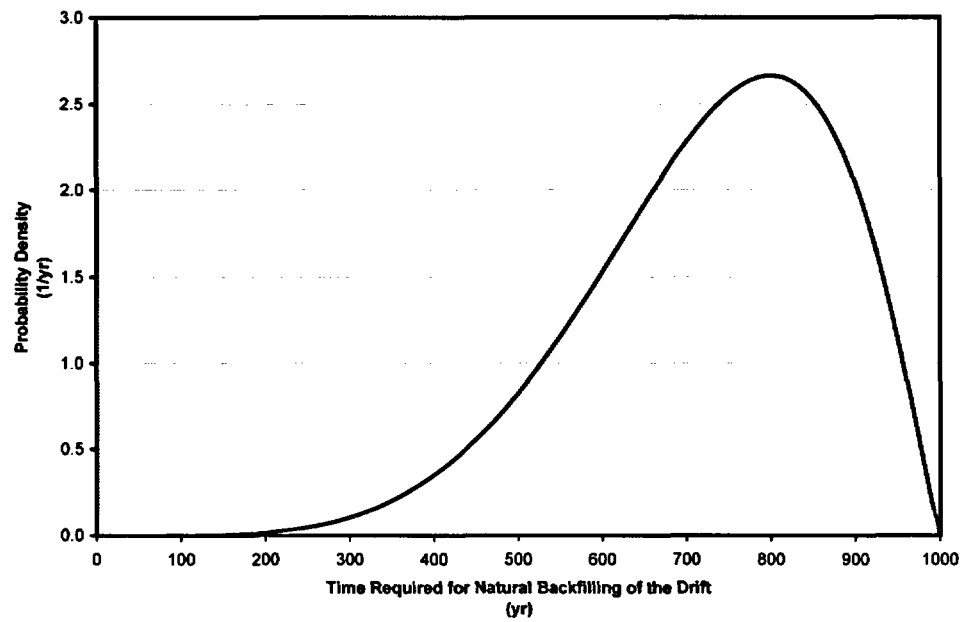

Figure 4-10. Beta Distribution Defining the Time Required for the Drifts to Backfill Themselves Completely

$$\frac{dh(x=0)}{dt} = \frac{(H_{max} - r_d)}{t_d} \tag{4-10}$$

where

dh/dt	—	drift degradation zone height rate (m/yr)
H_{max}	—	maximum drift degradation zone height (m)
t_d	—	natural backfilling time (yr)
r_d	—	drift radius (m)

The static rockfall load acting on the drip shield is calculated using both the drift degradation zone height rate and the volume of rockfall attributable to individual seismic events (see Section 4.2). The accumulated rockfall volume resulting from drift degradation is calculated on an incremental time basis. At the end of each TPA code time increment, the drift degradation height is updated using the following relationship

$$h_{i+1} = h_i + \frac{dh(x=0)}{dt}\Delta t_i \tag{4-11}$$

The additional volume of rockfall and its contribution to the static load can be readily calculated using basic elliptical geometry relationships, the updated drift degradation height defined in Eq. (4-11), and Eq. (4-8). The additional volume of rockfall attributable to a seismic event at the end of a time increment is added to the accumulated rockfall volume as well (see Section 4.2.3 for more details).

4.2 Characterization of Discrete Rock Block Impact Loads

Rockfall may be seismically induced or, as described in Section 4.1, caused by long-term degradation of a rock mass. In a fractured rock mass, the falling rocks may be blocks bounded by existing fractures or new rock blocks developed because of long-term degradation of existing blocks. The objective of this section is to describe the rationale, methodology, and basis for estimating the size distributions of the existing rock blocks in the Topopah Springs Welded Tuff Middle Nonlithophysal and Lower Lithophysal rock units and how this information is used to establish rock block impact loads on the engineered barrier subsystem.

4.2.1 Discrete Rock Block Size Distribution

4.2.1.1 Joint Data Input

The fracture orientation, spacing, and length used in developing the size distribution of existing rock blocks for the Topopah Spring Welded Tuff Middle Nonlithophysal and Lower Lithophysal units are given in Tables 4-3 and 4-4. The data presented in both tables were documented in a fracture geometry analysis report prepared by CRWMS M&O (2000c) and developed using the Exploratory Studies Facility fracture mapping data. These data include only the fractures with measured trace length larger than 1 m [3.28 ft].

The fracture bridge length and the gap between the edges of two adjacent coplanar fracture surfaces were assumed in this analysis because no data for these parameters are currently available. Fracture bridge length is normally a small value relative to the fracture trace length. If the fracture bridge length was assumed to be equal to zero, then a fracture could become persistent if variation in fracture spacing was not considered. Fracture bridge length somewhat controls the formation of blocks. Smaller values for bridge length improve the chance of a block forming.

4.2.1.2 Generation of Fracture Surfaces in Space

To generate fracture patterns in a three-dimensional space, a preprocessor for the Three-Dimensional Discontinuous Deformation Analysis computer code was used. A Monte Carlo technique was used so that variations associated with the fracture information could be considered. Note that each pattern generated is an equally likely realization of fractures that honors the information in Tables 4-3 and 4-4. In developing these realizations, the fracture spacing, length, and bridge length were assumed to be uniformly distributed and varied ±30 percent about the mean values of the respective parameters.

For each realization, a model of 20 × 20 × 20 m [65.6 × 65.6 × 65.6 ft] in dimension was used to generate fracture patterns for the Topopah Spring Welded Tuff Middle Nonlithophysal unit in a three-dimensional space while the model dimension was 40 × 40 × 40 m [131.2 × 131.2 × 131.2 ft] for the Topopah Spring Welded Tuff Lower Lithophysal unit. The larger dimension was used for the latter because the associated fracture spacings were relatively larger than those for the Topopah Spring Welded Tuff Middle Nonlithophysal unit. The larger dimension was used to minimize the potential model-boundary effect.

Table 4-3. Fracture Information for Topopah Spring Welded Tuff Middle Nonlithophysal Rock Unit					
Fracture Set Number	Dip Angle,* Degrees	Dip Direction,* Degrees	Mean Trace Length,† m [ft]	Mean Bridge Length,‡ m [ft]	Mean Spacing,† m [ft]
1	84	221	2.54 [8.33]	0.1 [0.33]	0.60 [1.97]
2	83	299	2.71 [8.88]	0.1 [0.33]	1.92 [6.30]
3	9	59	3.23 [10.59]	0.1 [0.33]	0.56 [1.84]

*CRWMS M&O. "Fracture Geometry Analysis for the Stratigraphic Units of the Repository Host Horizon." ANL–EBS–GE–000006. Rev. 00. Las Vegas, Nevada: CRWMS M&O. 2000.
†CRWMS M&O. "Drift Degradation Analysis." ANL–EBS–MD–000027. Rev. 01. Las Vegas, Nevada: CRWMS M&O. 2000.
‡Assumed values.

Table 4-4. Fracture Information for Topopah Spring Welded Tuff Lower Lithophysal Rock Unit					
Fracture Set Number	Dip Angle,* Degrees	Dip Direction,* Degrees	Mean Trace Length,† m [ft]	Mean Bridge Length,‡ m [ft]	Mean Spacing,† m [ft]
1	82	235	4.56 [14.96]	0.1 [0.33]	3.47 [11.38]
2	79	270	4.02 [13.19]	0.1 [0.33]	4.05 [13.28]
3	5	45	7.36 [24.14]	0.1 [0.33]	2.94 [9.64]

*CRWMS M&O. "Fracture Geometry Analysis for the Stratigraphic Units of the Repository Host Horizon." ANL–EBS–GE–000006. Rev. 00. Las Vegas, Nevada: CRWMS M&O. 2000.
†CRWMS M&O. "Drift Degradation Analysis." ANL–EBS–MD–000027. Rev. 01. Las Vegas, Nevada: CRWMS M&O. 2000.
‡Assumed values.

The fracture geometry analysis report prepared by CRWMS M&O (2000c) shows that the fracture spacings and trace lengths for the four litho-stratigraphic subunits of the Topopah Spring Welded Tuff are mostly lognormally distributed and some are exponentially distributed. Consequently, depending on the lower and upper limits used to constrain sampling, the assumption of a uniform distribution in this analysis could potentially underestimate the maximum block size but overestimate the number of relatively large blocks available. No attempt was made to address the potential effects of the uniform distribution assumption used in this study. Variations in fracture dip angle and dip direction were not incorporated in the analyses presented in this report to avoid producing blocks with overly complicated geometries.

In this study, a fracture plane in the three-dimensional space was treated as a planar surface. Potential curved conditions were not considered because of complexity and lack of information. There are considerable uncertainties on what the representative shapes for fracture planes

should be. The shape of a fracture plane may depend largely on the mechanism through which the fracture is formed. In this study, a fracture surface was assumed to be a square in shape with its length equal to the length of the corresponding fracture. The potential shape effects on rock block size distribution were not evaluated.

The fracture trace lengths listed in Tables 4-3 and 4-4 are mapped field data, which form a lower bound on actual dimensions of the fracture planes. To avoid under-representation of actual dimensions of fracture planes, three length dimensions representing a square fracture geometry were used in this study to assess the distribution of block sizes. These length dimensions were equal to two, three, and four times the corresponding fracture trace lengths.

4.2.1.3 Probability of Occurrence of Block Size

After a fracture pattern was fully developed for a realization, it was used to identify individual rock blocks. A rock block is defined as a rock fragment or piece that is isolated completely from the rest of the rock medium by the surrounding fracture surfaces. Five realizations for each fracture length dimension were performed. No attempt was made to determine the potential effect of number of realizations on block number and size distribution.

Figure 4-11 shows the percent distribution of rock block sizes developed using the three fracture plane dimensions for the Topopah Spring Welded Tuff Middle Nonlithophysal unit. The curves presented in Figure 4-11 were calculated based on isolated rock blocks identified for five realizations. Each data point shown in the figure represents a volume range. The largest volume in each volume range was used in the figure for convenience. For the cases where the fracture dimension was twice the corresponding trace length, the total volume of the isolated rock blocks formed ranged from 10 to 14 percent of the volume of the model, which was 20 × 20 × 20 m [65.6 × 65.6 × 65.6 ft] in dimension, for the five realizations performed. The range was from 43 to 54 percent for the cases where the fracture dimension was three times the corresponding trace length and varied from 62 to 64 percent for the cases where the fracture dimension was four times the corresponding trace length.

Understandably, it is less likely that smaller fracture planes intersect and consequently form isolated blocks. Even though the number of blocks formed using the three fracture plane dimensions were different, the size distributions for the blocks identified appeared to be similar, as shown in Figure 4-11. Figure 4-12 presents the data shown in Figure 4-11 in a cumulative fashion. A majority of the blocks (more than 95 percent) were smaller than 4 m^3 [141 ft^3] with only a very small percentage of the rock blocks greater than 8 m^3 [282 ft^3].

No more than one isolated block was formed for each realization performed for the Topopah Spring Welded Tuff Lower Lithophysal unit when the fracture plane dimension used was either two or three times the mapped fracture trace length. Although some isolated rock blocks were identified for the five realizations where four times the corresponding trace length was used as the fracture dimension, the number of blocks for each realization ranged only from 6 to 16. The volume of these isolated rock blocks varied from 43 m^3 [1,520 ft^3] to 160 m^3 [5,650 ft^3], which was considerably larger than those for the Topopah Spring Welded Tuff Middle Nonlithophysal unit. The average total volume of the isolated rock blocks for the five realizations amounted to less than 0.2 percent of the total model volume. Recall that the model used for the Topopah Spring Welded Tuff Lower Lithophysal unit was 40 × 40 × 40 m [131.2 × 131.2 × 131.2 ft] in size. This finding suggests that the Topopah Spring Welded Tuff Lower Lithophysal

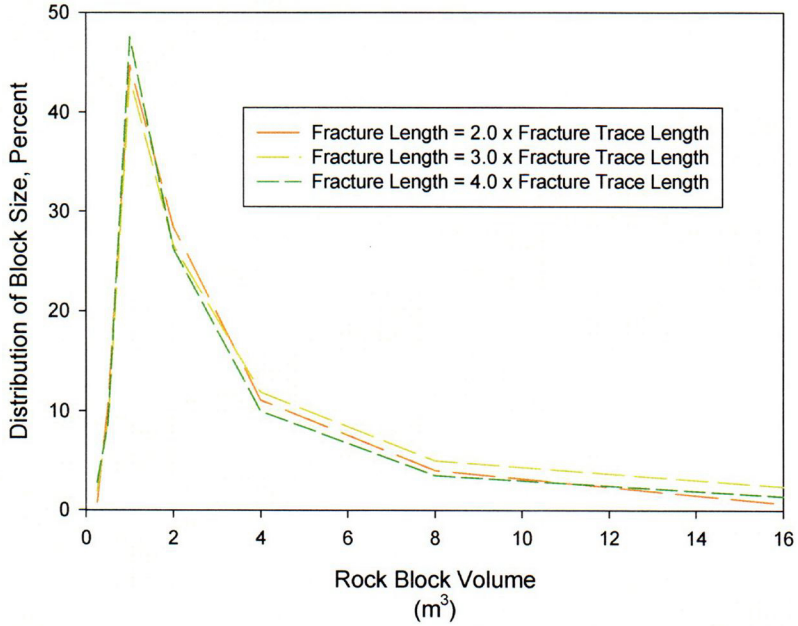

Figure 4-11. Normalized Histogram of Rock Block Size Distribution for the Topopah Spring Welded Tuff Middle Nonlithophysal Rock Unit

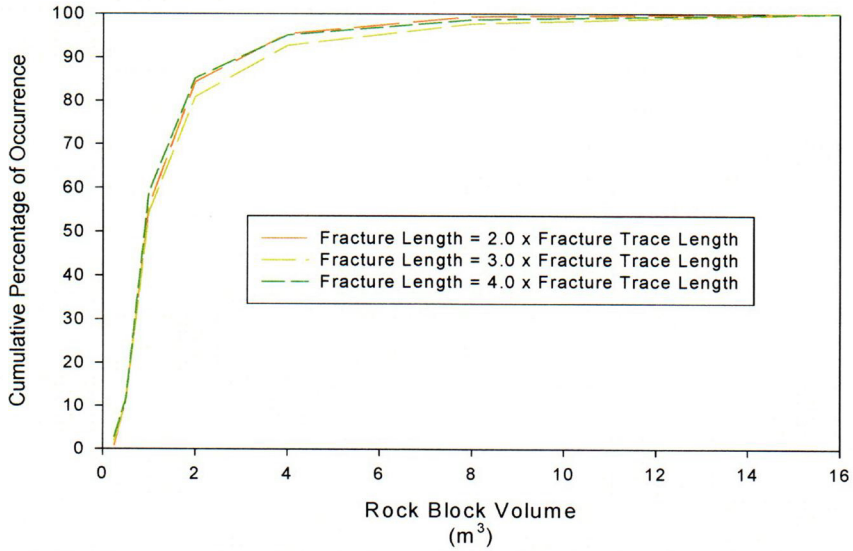

Figure 4-12. Cumulative Rock Block Size Distribution for the Topopah Spring Welded Tuff Middle Nonlithophysal Rock Unit

C03

unit can be considered a continuous medium if the representative fracture plane dimension is less than or equal to four times the mapped trace length.

4.2.2 Discrete Rock Block Loads

Although rock blocks of sufficient size to cause appreciable dynamic impact to the drip shield can be expected at any time as a result of the various rock mass degradation processes described earlier, a satisfactory basis for how many, and when they may fall does not exist at this time. As a result, it is simply assumed for the development of the MECHFAIL module of the TPA code that discrete rock block impact loads on the drip shield may occur only when a seismic event of a sufficient magnitude occurs. A compilation of case histories of tunnel damage from earthquake shaking by Dowding and Rozen (1978) suggests threshold ground-motion magnitudes that would cause damage to underground excavations (Figure 4-13). The case histories involved 71 tunnels subjected to earthquakes of Richter magnitude 5.8–8.3. The majority of the tunnels were excavated in rock. Only three of the tunnels were excavated in soil-like materials. The observed tunnel damage was compared with the value of peak ground acceleration calculated at the ground surface using an attenuation relationship. Tunnel damage was divided into three classes on the bases of the observed earthquake-induced damage, as shown in Figure 4-13. "No damage" implies that no earthquake-induced cracks or rockfall was observed; "minor damage" implies that earthquake-induced cracking and rockfall were observed but were considered minor; and "damage" implies that major rockfall, severe cracking, and closure of the tunnel occurred. The information in Figure 4-13 suggests that a minimum ground-surface acceleration of approximately 0.2 g is needed to initiate earthquake-induced damage to an underground opening, and a ground-surface acceleration of approximately 0.5 g or greater would be sufficient to cause major earthquake-induced damage to an underground opening.

Many researchers have proposed using particle velocities as an alternative to using peak ground accelerations at the ground surface to estimate the damage incurred by subsurface excavations (NRC, 1991). In summary, loose rock is likely to begin to fall for particle velocities of 0.050 m/s [0.164 ft/s], 0.300 m/s [0.984 ft/s] for ground falls, and 0.600 m/s [1.969 ft/s] for severe damage. Because the TPA code limits its characterization of seismic ground motions to mean peak horizontal ground accelerations, it was decided that the amount of rockfall caused by a seismic event would be based on this parameter.

4.2.3 Discrete Rock Block Load Abstraction

Assuming that the damage to the drift can be represented by a change in the drift degradation zone height that is proportional to the magnitude of the seismic event peak ground acceleration, pga, the total volume of falling discrete rock blocks can be estimated. Referring to Figure 4-14, the increase in the drift degradation zone height for a given seismic event depends on the peak ground acceleration needed to cause minor damage, g_o, the peak ground acceleration needed to cause major damage (i.e., drift closure), g_{max}, and the maximum drift degradation zone height, H_{max}. The relationship shown graphically in Figure 4-14 is represented mathematically in the following equation.

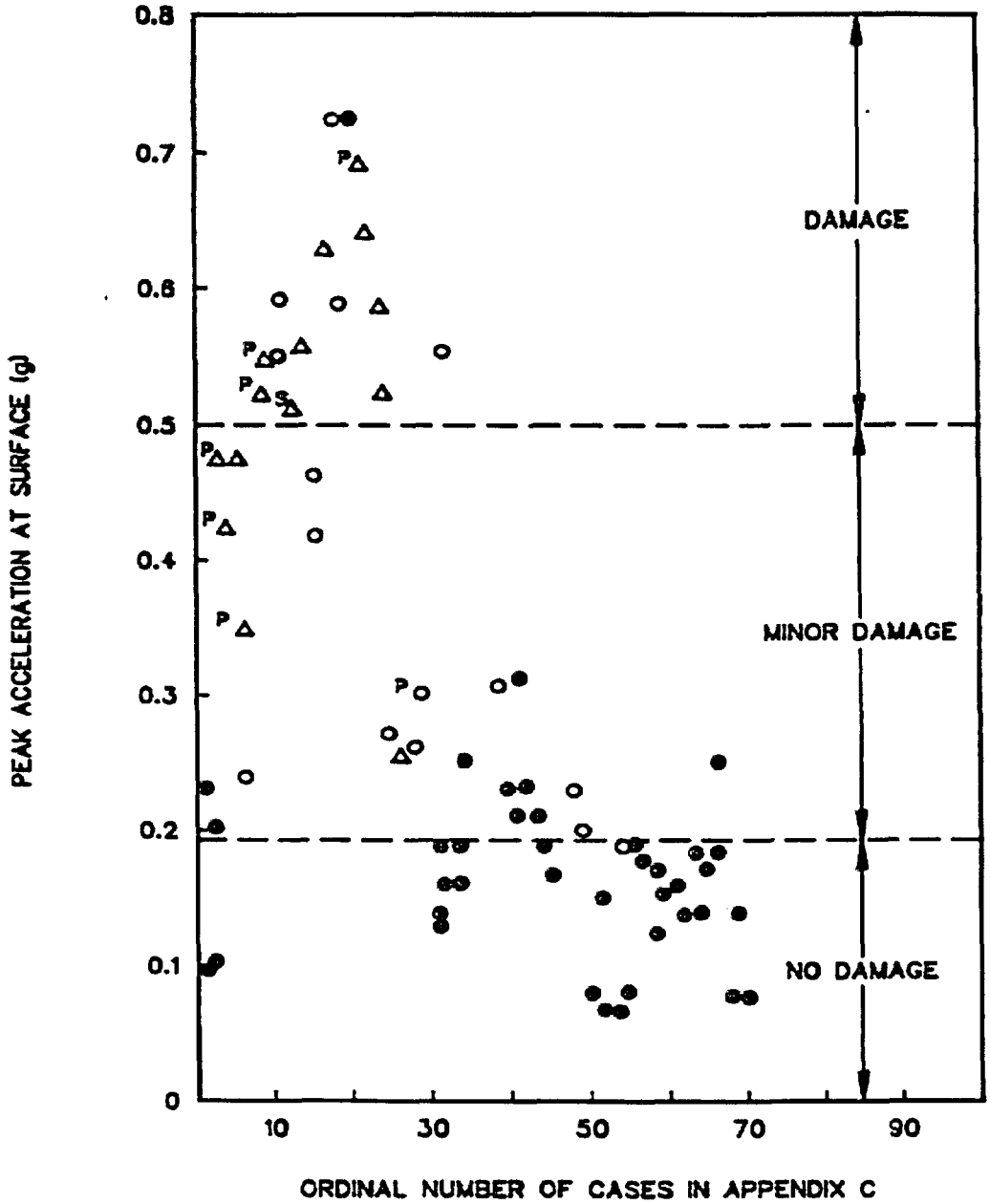

LEGEND

● NO DAMAGE

○ MINOR DAMAGE

△ DAMAGE FROM SHAKING

P△ NEAR PORTAL

S△ SHALLOW COVER

Figure 4-13. Characterization of Drift Damage as a Function of Ground Surface Peak Ground Accelerations (Dowding and Rozen, 1978)

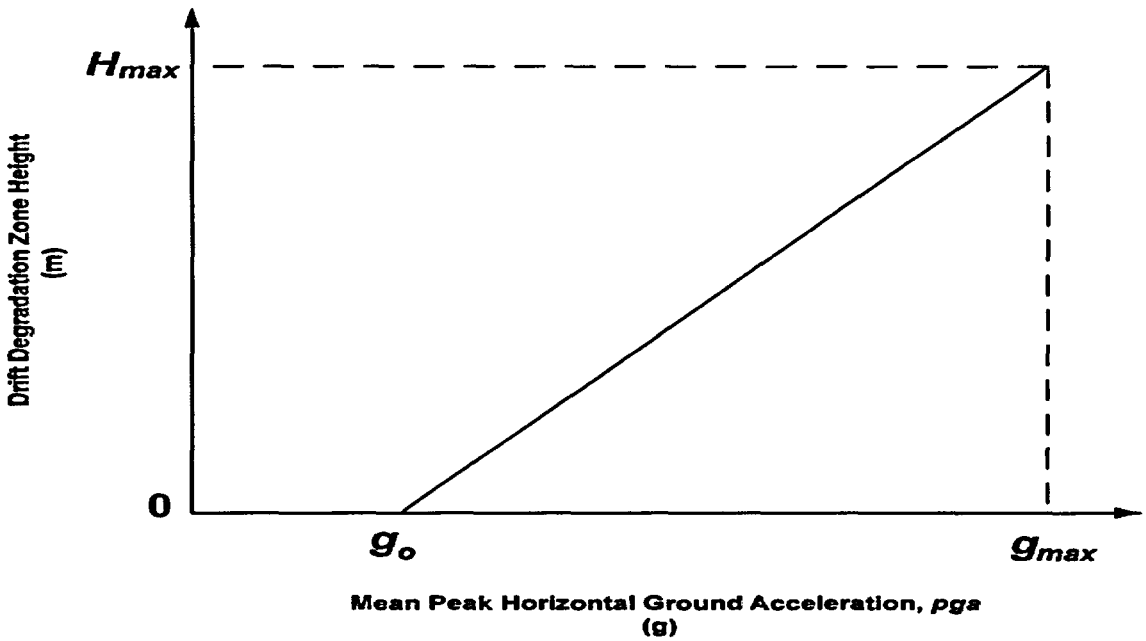

Figure 4-14. Change in the Drift Degradation Zone Height as a Function of Mean Peak Horizontal Ground Acceleration

$$\Delta h = \frac{\left(H_{\max} - h_{i+1}\right)}{\left(g_{\max} - g_o\right)}\left(\text{pga} - g_o\right) \tag{4-12}$$

The fundamental precept of Eq. (4-12) is that there is a certain ground motion that corresponds to the onset of damage within the drift (i.e., g_o) and a ground motion (i.e., g_{max}) that will cause the drift to fail to the maximum extent allowed by the conservation of mass presented in Section 4.1. Lacking any other information, a linear relationship was assumed between these two points. Note that the slope of the curve is updated as the drift degradation zone height changes. This change in slope is intended to account for the increased drift stability expected as the drift degradation zone height increases. When implemented within the MECHFAIL module, the drift degradation zone height is updated first using Eq. (4-11) to account for the rockfall associated with the coupled thermal, mechanical, hydrological, and chemical processes by way of the drift degradation rate over the timestep preceding additional rockfall from the seismic event. Furthermore, each spatial grid element is assigned a value of g_o and g_{max} using beta distributions. For g_o, the minimum mean peak horizontal ground acceleration required to cause minor damage is greater than 0.2 g, and no more than 20 percent of the spatial grid elements will be assigned a g_o greater than 0.24 g (see Figure 4-15). Similarly, for g_{max}, the minimum mean peak horizontal ground acceleration required to cause major damage is greater than 1.0 g, and no more than 20 percent of the spatial grid elements will be assigned a g_{max} greater than 1.20 g (see Figure 4-16). Recall that the magnitude of H_{max} is controlled by the bulking factor that was assigned to the spatial grid element (see Section 4.1).

After the change in the drift degradation zone height, Δh, defined in Eq. (4-12), has been calculated for its respective grid element, the volume of rockfall caused by the seismic event

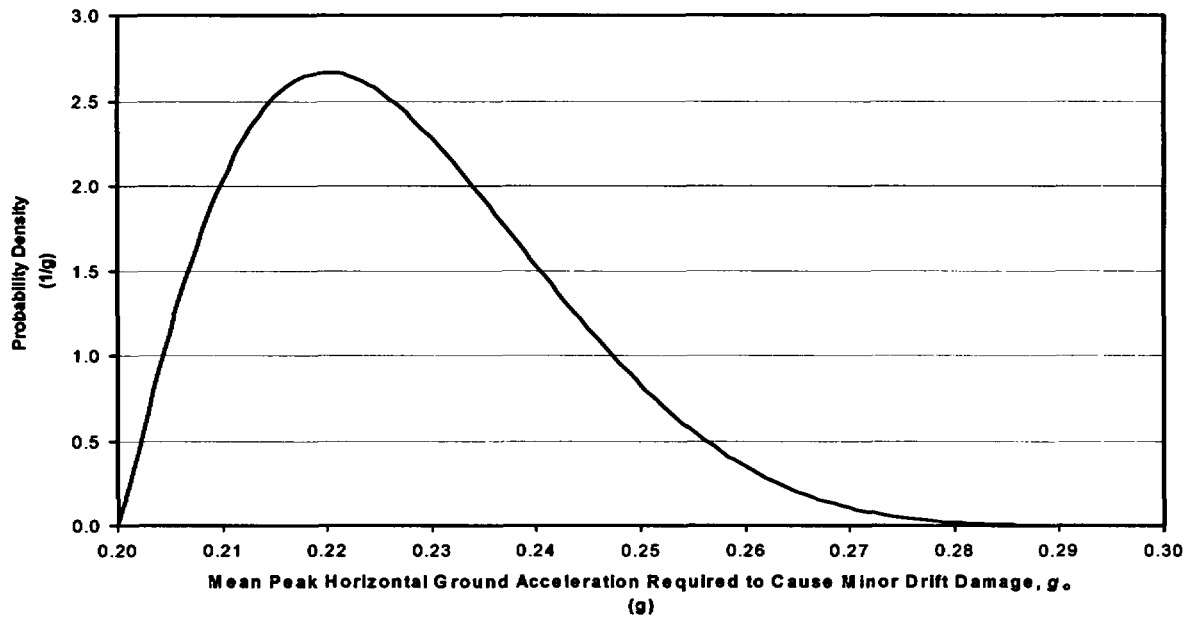

Figure 4-15. Beta Distribution Defining the Mean Peak Horizontal Ground Acceleration Required to Cause Minor Drift Damage

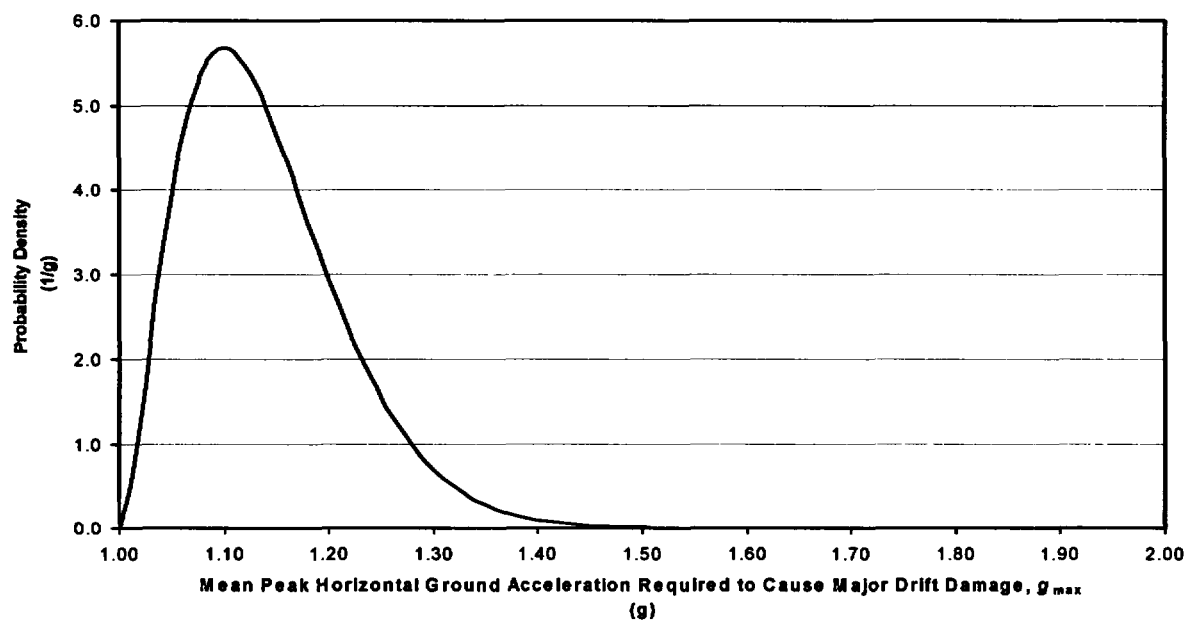

Figure 4-16. Beta Distribution Defining the Mean Peak Horizontal Ground Acceleration Required to Cause Major Drift Damage

can be determined. The rock block size distribution curve is then sampled until the sum of the individual rock block volumes is greater than the total volume of rockfall calculated for the seismic event. The individual rock blocks are then sorted from largest to smallest until the sum of the individual rock block volumes is greater than the total volume of rockfall calculated for the seismic event. This sorting process is performed to ensure a large rock block is not thrown out of the sample simply because it was the last rock block retrieved from the rock block size distribution curve. These rock blocks are then assumed to impact the drip shield with a fall height equal to h_{i+1}. Lastly, once the accumulated amount of rockfall is sufficient to cover the drip shield crown under a 0.5-m [1.64-ft] depth of rock rubble, the effects of discrete rock blocks impacting the drip shield are no longer evaluated. The rockfall caused by the occurrence of seismic events is still accounted for in the static rockfall loads after this threshold is met, however.

5 DRIP SHIELD AND ACCUMULATED ROCKFALL STATIC LOAD PERFORMANCE ANALYSES

It is expected that varying amounts of rock debris or rubble will accumulate around the drip shield during the 10,000-yr regulatory period. An understanding of the response of the various components of the engineered barrier subsystem—including the drip shield, waste package, waste form, pallet, invert, and drift—to the static load created by this accumulated rubble is needed. Furthermore, potential interactions between the components that could be caused by this static load must be understood. This chapter documents the work accomplished thus far in understanding the effects of accumulated rockfall on the drip shield. Sections 5.1 and 5.2 discuss the methodology used to simulate drip shield performance and the resultant stress and deflection data. Section 5.3 discusses how these data have been used to model the response of the drip shield to static rockfall loads in the MECHFAIL Total-system Performance Assessment (TPA) code module.

5.1 Finite Element Model Description

This section documents the finite element analyses that were performed to assess the effects of accumulated rockfall rubble on the drip shield. As a first approximation, it was assumed that the static rockfall loads acting on the drip shield are symmetrically distributed over the drip shield surface. The response of the drip shield to an asymmetric buildup of accumulated rockfall rubble or natural load eccentricities, however, may be quite different than the scenario being evaluated here. For example, the symmetric load and boundary conditions applied in the current model inherently preclude lateral (i.e., horizontal) deflections of the drip shield crown apex. Therefore, the current finite element model is expected to overestimate the structural capabilities of the drip shield when subjected to static rockfall loads because the lateral buckling mode has been artificially suppressed. In addition, the drip shield is not bolted, welded, or attached to the carbon steel frame of the invert in any way. As the carbon steel frame corrodes, the foundation of the drip shield is increasingly compromised and, as a result, can affect the response of the drip shield to rockfall loads (both static and dynamic). No attempt has been made to assess the potential effects of a degraded carbon steel invert frame in the current modeling efforts.

It was recognized early in the drip shield modeling process that the drip shield structural behavior will be affected by the rock rubble that has accumulated around its sides. Specifically, the rock rubble amassed around the sides of the drip shield and subjected to an overburden pressure by the accumulated rock above will enhance the structural stability and stiffness of the drip shield. It is not sufficient, however, to simply apply a static pressure distribution down the side of the drip shield to include this effect within the models because this approach would underestimate the structural support provided by the rubble. Therefore, the rock material interacting with the drip shield is modeled in two parts. The first part is the distributed pressure acting on the drip shield crown surface (see Section 5.1.2). The second part is a continuum model of the rock rubble that interacts with the side of the drip shield. The top surface of this rock rubble is subjected to an overburden pressure created by the accumulated rubble above the modeled section (see Sections 5.1.1 and 5.1.2).

Several simulations were performed to assess the response of the drip shield for varying magnitudes of static rockfall loads and the effective Young's Modulus of the rock rubble accumulated on the sides of the drip shield.

5.1.1 Finite Element Model Geometry

The finite element model of the drip shield subjected to static rockfall loads consists of four major components. These components are the drip shield, the rockfall rubble, invert, and the drift wall. Figure 5-1 shows the layout of these components, while Figure 5-2 highlights the individual components that make up the drip shield. As can be seen from Figure 5-1, the finite element model takes advantage of the geometrical, loading, and kinematic symmetry conditions assumed to exist to prepare an efficient model for simulation. Geometrically, it is assumed that the drip shield segments, defined by the uniform axial spacing of the support beam and bulkhead reinforcing members, repeat continuously in the axial direction. The resulting model is cut at the axial and lateral symmetry planes as shown in Figure 5-3. As was pointed out earlier, the assumed symmetric load and boundary conditions applied in the current model inherently preclude lateral (i.e., horizontal) deflections of the drip shield crown apex. Therefore, the current finite element model is expected to overestimate the structural capabilities of the drip shield when subjected to static rockfall loads because the lateral buckling mode has been artificially suppressed.

The model was constructed using a mixture of plate and solid elements. Plate elements (three-dimensional quadrilaterals) are used for the Titanium Grade 7 panel sections, including the drip shield crown plates, side plates, and inner and outer stiffening plates. Plate elements were also used to represent the Alloy 22 base of the structure. Solid elements (three-dimensional hexahedrons) are used to represent the Titanium Grade 24 structural support beam and bulkhead components (CRWMS M&O, 2000a, Reference Sketch Number SK–0148, Revision 05). The cited reference sketch also documents the detailed dimensions of the drip shield. In addition, the common surfaces between components were modeled as idealized tied surfaces by discretizing the interface congruently and equivalencing the common nodes. In actuality, these components will be welded at their respective peripheries, which would allow the common surfaces to deform independently if the welds fail. The stresses predicted at the component peripheries may be underestimated as a result of this modeling simplification.

Elastic-plastic material behavior and small strain element formulations were used for the drip shield models subjected to static rockfall loads. Plate elements were used to represent the thin drip shield structural members, such as the Titanium Grade 7 plate regions. This approximation does not provide accurate results, however, if the drip shield undergoes large deformations that significantly change the geometry of the structure relative to its original configuration. Large deflection theory accounts for changes in load distribution created by the large deformations and uses a more robust mathematical formulation for calculating strains such that large rigid body rotations within the finite element model do not erroneously predict strains. The ability to use plate elements in the construction of the drip shield finite element model significantly reduces the memory requirements and computational times required to perform the analyses relative to a model comprised solely of solid elements.

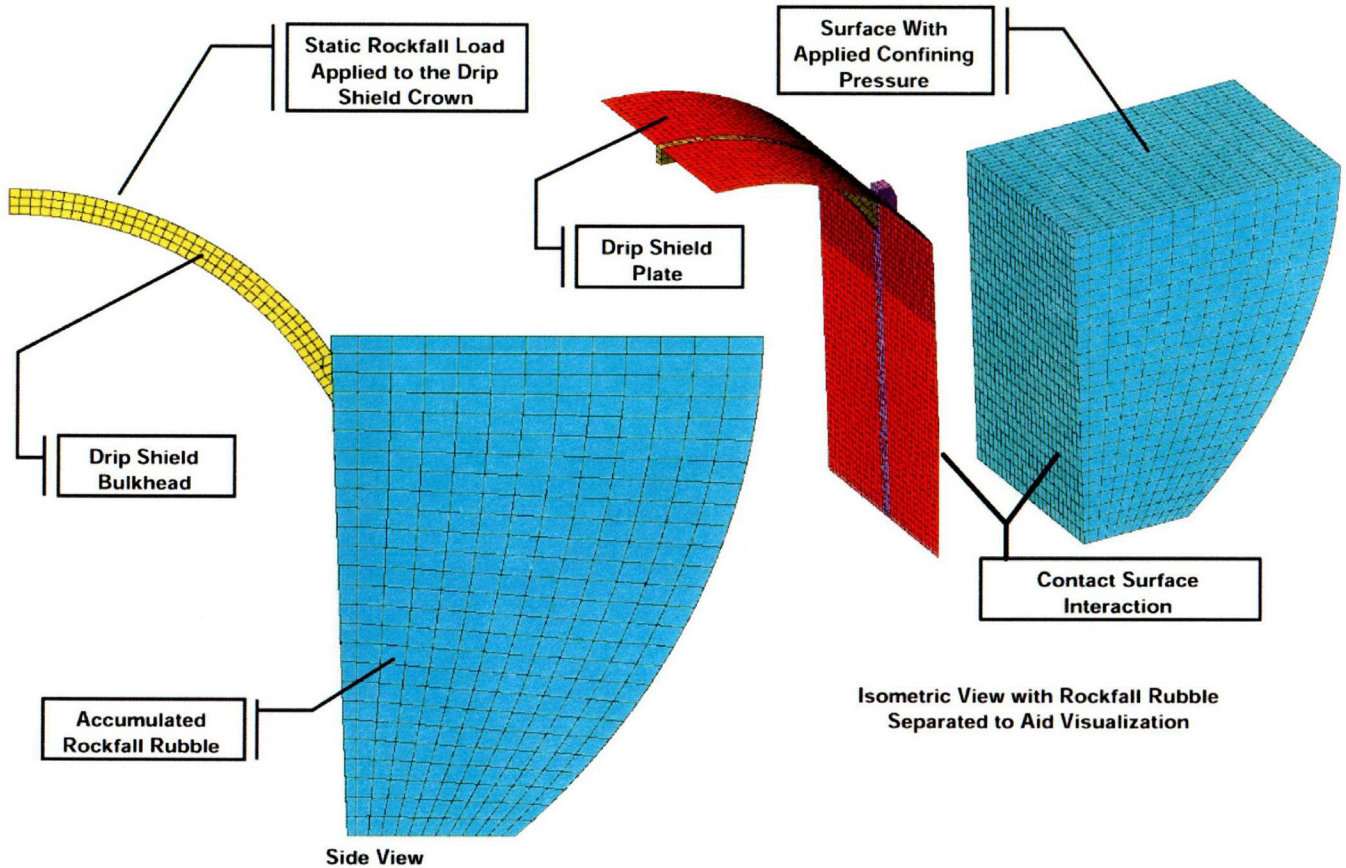

Figure 5-1. Drip Shield and Accumulated Rockfall Interaction Model

C04

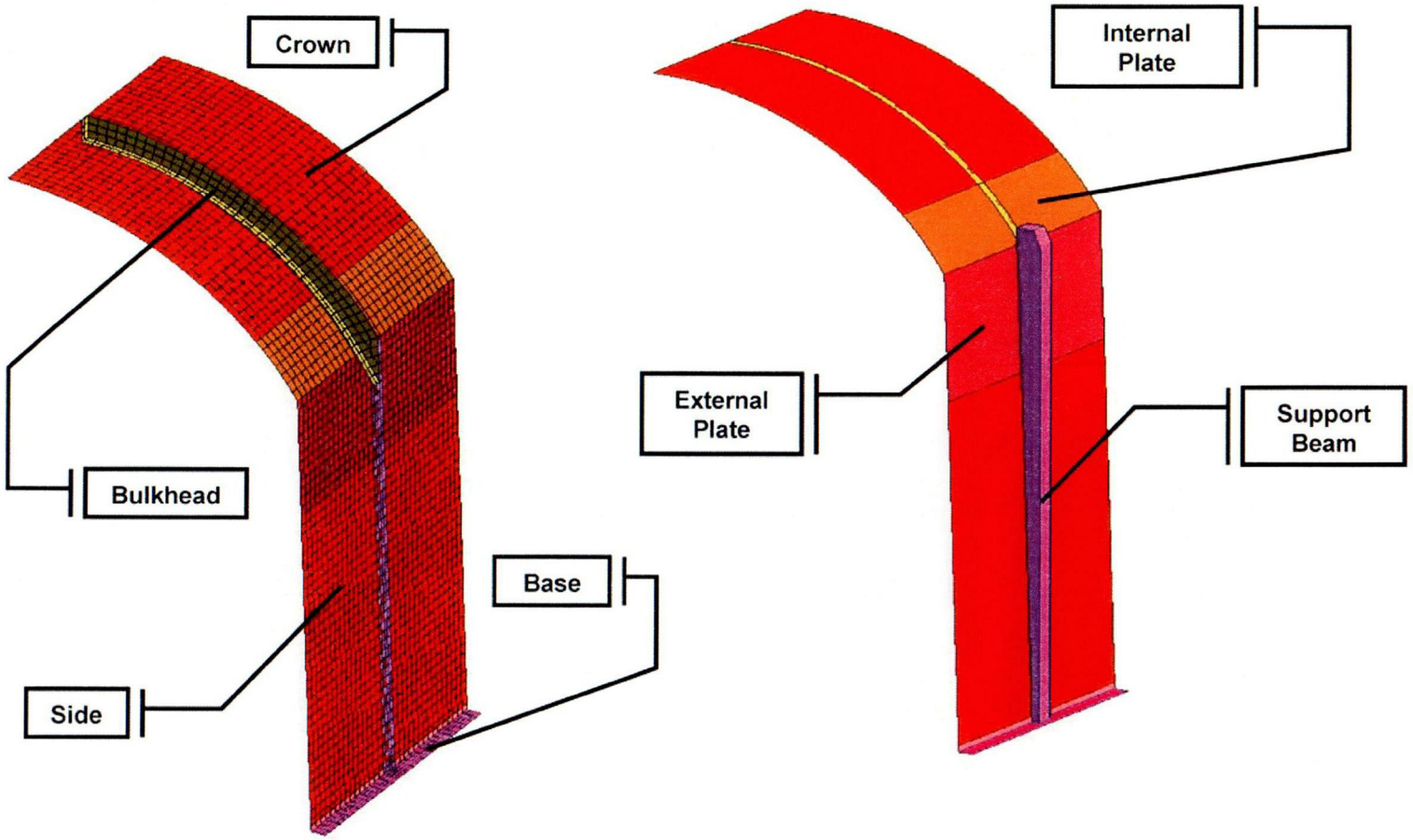

Figure 5-2. Drip Shield Components

C05

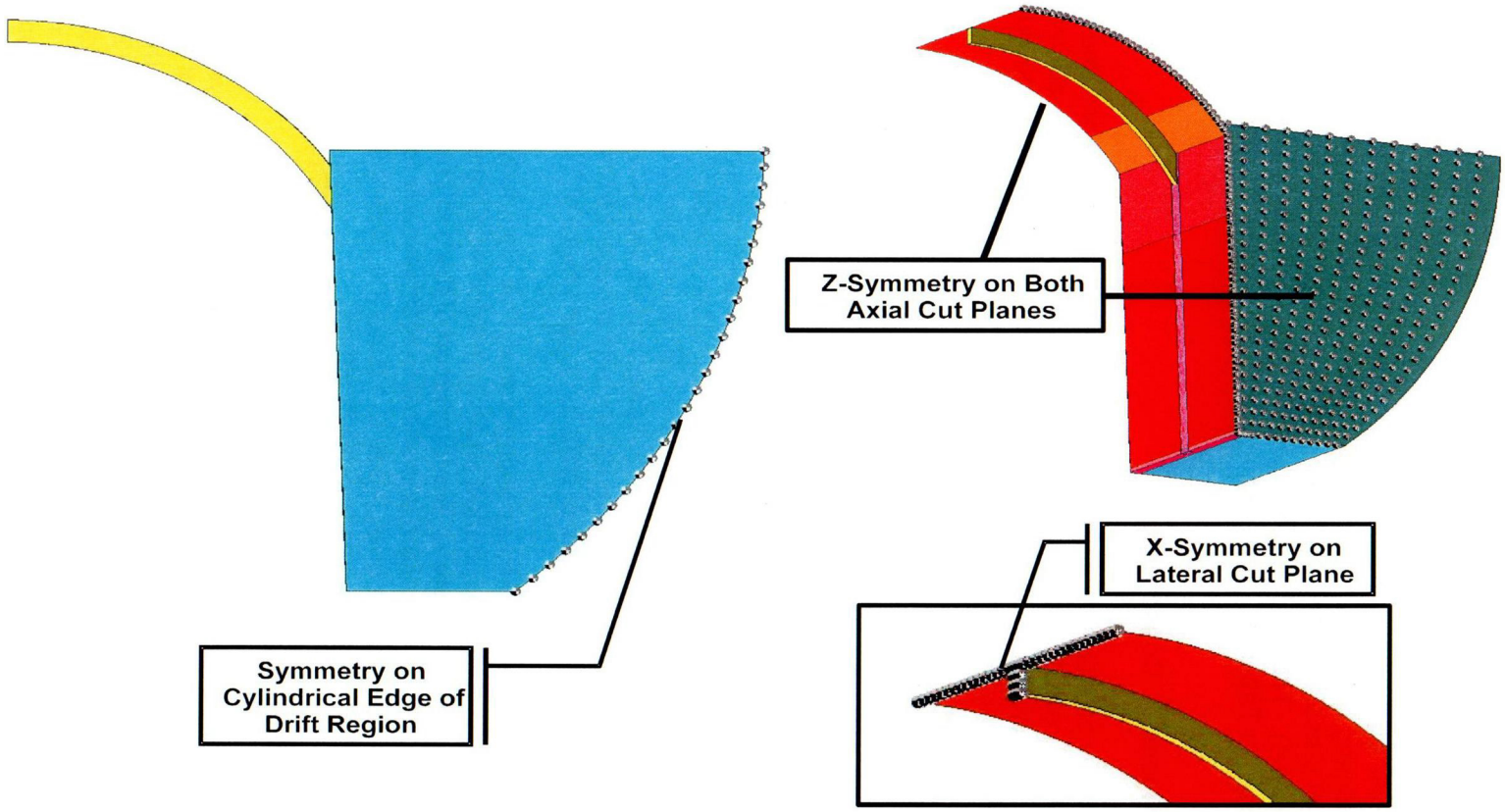

Figure 5-3. Drip Shield and Accumulated Rockfall Rubble Interaction Model Kinematic Boundary Conditions

C06

5.1.2 Finite Element Model Boundary Conditions

5.1.2.1 Loads

Static pressure was applied to the drip shield crown and the top surface of the solid continuum elements representing the rockfall rubble that has accumulated on the sides of the drip shield. The distribution of pressure acting on the drip shield crown and on top of the rockfall rubble was derived from Eq. (4-4). Table 5-1 summarizes the static rockfall load history used in the model. The loads identified in Table 5-1 correspond to the maximum static rockfall loads for a given bulking factor.

5.1.2.2 Kinematic Constraints

The lateral symmetry condition constrains out-of-plane lateral translations and rotations. This particular constraint precludes the drip shield from leaning or sliding laterally into the waste package. Further analysis would be required to determine if a one-sided buildup of rockfall rubble constitutes a design risk for the drip shield or waste package.

The axial symmetry condition constrains translations and rotations out of the axial plane. This constraint is analogous to a two-dimensional plane strain assumption and implies that the static rockfall load is uniformly applied along the entire length of the drip shield.

The accumulated rubble interacting with the side of the drip shield was modeled using a contact definition that allowed the rubble to slide along the interface without separation. This type of contact definition allows the rockfall rubble to conform to the changing orientation of the drip shield wall as it deforms during the analysis. Modeling the interface between the drip shield side wall and rock rubble in this manner, however, allows tensile stresses to develop at the interface (i.e., the drip shield side wall is not allowed to pull away from the rock rubble). Therefore, the additional drip shield structural stability provided by the rock rubble is likely to be overestimated, with larger magnitudes of error for larger values of Young's modulus.

The invert and drift wall are modeled as a single analytical rigid body such that the drip shield and rockfall rubble are properly supported and constrained within the confines of the drift. As the carbon steel invert frame corrodes, the foundation of the drip shield is increasingly compromised, and the response of the drip shield to rockfall loads (both static and dynamic) may be affected. No attempt has been made to assess the potential effects of a degraded carbon steel invert frame in the current modeling efforts.

5.1.3 Finite Element Model Material Properties

Derivation of the drip shield component material properties and constitutive models were presented in detail in a previous report (Gute, et al., 2001). For the sake of completeness, however, Table 5-2 provides a summary of the basic material data used in the drip shield finite element models presented in this report. Table 5-3 indicates which material is assigned to each component shown in Figure 5-2. The values for density and Poisson's ratio delineated in Table 5-2 correspond to room temperature values. Any potential differences in density and Poisson's ratio between the assumed temperature of 150 °C [302 °F] and room temperature are not expected to be significant with regard to the various drip shield analyses presented in this

Table 5-1. Maximum Static Rockfall Loads for a Given Bulking Factor				
Load Step	Bulking Factor	Maximum Crown Pressure, MPa [psi]	Average Rock Rubble Overburden Pressure, MPa [psi]	Total Vertical Load, tonne/m [lb/ft]
1	1.5	0.156 [22.6]	0.150 [21.8]	40.0 [26,890]
2	1.4	0.198 [28.7]	0.189 [27.4]	50.9 [34,210]
3	1.3	0.272 [39.4]	0.255 [37.0]	69.3 [46,580]
4	1.2	0.420 [60.9]	0.388 [56.3]	106.5 [71,590]
5	1.1	0.869 [126.0]	0.789 [114.4]	218.7 [147,010]

Table 5-2. Summary of Drip Shield Material Property Data at 150 °C [302 °F]			
Material Name	Density, tonne/m^3 [lb/in^3]	Young's Modulus, GPa [psi]	Poisson's Ratio
Titanium Grade 7	4.512 [0.163]*	100.7 [14.6 × 10^6]†	0.32‡
Titanium Grade 24	4.512 [0.163]*	107.2 [15.5 × 10^6]§	0.32‡
Alloy 22	8.691 [0.314]‖	197.2 [28.6 × 10^6]¶	0.32‖

*ASME International. "ASME International Boiler and Pressure Vessel Code." Table NF–2, Typical Physical Properties of Nonferrous Materials (Unalloyed Titanium). New York City, New York: ASME International. 2001.
†ASME International. "ASME International Boiler and Pressure Vessel Code." Table TM–5, Moduli of Elasticity of Titanium and Zirconium for Given Temperatures. New York City, New York: ASME International. 2001.
‡ASME International. "ASME International Boiler and Pressure Vessel Code." Table NF–1, Typical Mechanical Properties of Materials (Unalloyed Titanium). New York City, New York: ASME International. 2001.
§U.S. Department of Defense. "Military Handbook: Metallic Materials and Elements for Aerospace Vehicle Structures." MIL–DBK–5H. Figure 5.4.1.1.4, Effect of Temperature on the Tensile and Compressive Moduli of Annealed Ti–6Al–4V Alloy Sheet and Bar. Washington, DC: U.S. Department of Defense. 1998.
‖ASTM International. "Standard Specification for Low-Carbon Nickel-Molybdenum-Chromium, Low-Carbon Nickel-Chromium-Molybdenum, Low-Carbon Nickel-Chromium-Molybdenum-Copper, Low-Carbon Nickel-Chromium-Molybdenum-Tantalum, and Low-Carbon Nickel-Chromium-Molybdenum-Tungsten Alloy Plate, Sheet, and Strip." New York City, New York: ASTM International. 1998.
¶ASME International. "ASME International Boiler and Pressure Vessel Code." Table TM–4, Moduli of Elasticity of High Nickel Alloys for Given Temperatures. New York City, New York: ASME International. 2001.

Table 5-3. Drip Shield Component Materials			
Drip Shield Component	Titanium Grade 7	Titanium Grade 24	Alloy 22
Crown	X	—	—
Side Plating	X	—	—
Inner Plate Stiffener	X	—	—
Outer Plate Stiffener	X	—	—
Bulkhead	—	X	—
Support Beam	—	X	—
Base	—	—	X

report. The Young's moduli for the different materials, on the other hand, have been adjusted to account for the effects of temperature. The Young's modulus for Titanium Grade 7 was obtained from Table TM–5 of the ASME International (2001) Boiler and Pressure Vessel Code. The Young's modulus for Alloy 22 was obtained from Table TM–3 of the ASME International (2001) Boiler and Pressure Vessel Code. Note that the Young's modulus for Alloy 22 was not explicitly provided in Table TM–3 of the ASME International (2001) Boiler and Pressure Vessel Code. The value for Young's modulus at 150 °C [302 °F] provided for nickel alloy Uniform National Standard number N06455 was used for Alloy 22 because of its similarity in alloy composition to Alloy 22. The temperature-dependent values for the Young's moduli of Titanium Grade 5 or Titanium Grade 24 are not provided in the ASME International (2001) Boiler and Pressure Vessel Code. Note that the composition of Titanium Grade 5 and Titanium Grade 24 are the same except that the Titanium Grade 24 contains 0.04 to 0.08 percent palladium. As a result, it is expected that these two grades will exhibit similar mechanical behavior (i.e., mechanical properties). The U.S. Department of Defense (1998) and ASM International (1994) provide extensive material data for Titanium Grade 5. The Young's modulus for Titanium Grade 5 corresponding to a temperature of 150 °C [302 °F] was derived from graphical data provided in U.S. Department of Defense (1998). As Table 5-2 indicates, the density and Poisson's ratio used in the analysis for the Titanium Grade 24 drip shield components were the same as those used for Titanium Grade 7. According to the U.S. Department of Defense [1998; Table 5.4.1.0(b)], more appropriate room temperature values for density and Poisson's ratio would be 4,429.0 kg/m^3 [0.160 lb/in^3] and 0.31. These values do not appreciably vary from those used in the analyses and the results presented in this report, therefore, are well within acceptable engineering tolerances. Nevertheless, the updated values for density and Poisson's ratio will be used in future analyses. Additional drip shield material properties of interest are tabulated in Table 5-4. These properties have been adjusted from their standard engineering stress and strain values to their corresponding Cauchy stress and logarithmic strain counterparts (Gute, et al., 2001). This adjustment was needed to satisfy the requirements of the ABAQUS finite element code used to perform the analyses presented in this report. Lastly, with regard to temperature effects on material mechanical properties, it has yet to be established that the assumed 150 °C [302 °F] material temperature adequately bounds the potential temperatures of the various engineered barrier subsystem component materials subjected to naturally backfilled conditions.

Any accumulated rubble behind the drip shield wall may contribute to the structural resistance of the drip shield if the drip shield walls tend to deform outward when subjected to vertical loading. Outward deformation of the drip shield walls would tend to compress the rubble, thereby developing a passive resistance. The amount of passive resistance developed through a compression of the rubble varies with the confining pressure and the magnitude of any previous compression (e.g., Lambe and Whitman, 1969, pp. 164–166). The limiting passive resistance, which is related to the vertical stress through the coefficient of passive earth pressure for the rubble, varies with several factors such as particle size and shape distributions, degree of wetness, strength of individual particles, and porosity (e.g., Marsal, 1973). The potential contribution of the accumulated rubble to the structural resistance of the drip shield, therefore, depends on a complex combination of processes and parameter values. To obtain a range of estimates for the buckling resistance of the drip shield, the rubble is represented in the drip shield finite element model as a linear-elastic continuum. The stiffness of the continuum is varied in the model to represent a wide range of conditions, from a model case with no lateral support for the drip shield to a case with lateral support from a linear-elastic continuum assigned a Young's modulus of 30 MPa [4.36 × 10^3 psi] (see Table 5-5).

Table 5-4. Drip Shield Material Data for Modeling Post-Yield Behavior at 150 °C [302 °F]			
Material Name	Yield Stress,* MPa [psi]	Ultimate Tensile Strength,* MPa [psi]	Log Normal Failure Strain, Percent
Titanium Grade 7	174.1 [2.53×10^4]	299.5 [4.34×10^4]	17.93
Titanium Grade 24	658.1 [9.54×10^4]	827.0 [1.20×10^5]	8.76
Alloy 22	254.7 [3.69×10^4]	984.7 [1.43×10^5]	36.7
*Cauchy Stress			

Table 5-5. Case Numbers for the Assumed Rock Rubble Young's Moduli Evaluated	
Case	Young's Modulus MPa [psi]
1	no rock
2	3.0 [4.35×10^2]
3	6.0 [8.70×10^2]
4	10.0 [1.45×10^3]
5	30.0 [4.36×10^3]

The lateral pressure exerted on the walls of the drip shield by the rockfall rubble can be approximated using the ratio of horizontal (or lateral) to vertical (or overburden) pressure at rest, (i.e., K_o). According to Lambe and Whitman (1969, Figure 13.7), $K_o = 0.2$ for the condition of no horizontal strain, which is assumed to be the case here because of the plane strain conditions applicable in the axial direction and the presence of the drip shield and drift wall restricting or limiting lateral strain. In other words, only vertical, uniaxial strain is expected to result from the confining pressure acting on the top surface of the continuum elements representing the rock rubble that has accumulated on the sides of the drip shield. For these conditions, the ratio of horizontal to vertical pressure (or stress) can be shown to be

$$K_o = \frac{\sigma_H}{\sigma_V} = \frac{\nu}{(1-\nu)} \tag{5-1}$$

where

ν — Poisson's ratio
σ_H — horizontal stress
σ_v — vertical stress

For the assumption that K_o = 0.2, Eq. (5-1) can be used to calculate the corresponding value of Poisson's ratio (i.e., ν = 0.17).

5.2 Summary of Analysis Results

The various simulations of the drip shield subjected to static rockfall loads were run until the full load was applied or until the drip shield structure became unstable (i.e., the onset of buckling was determined). The unstable condition is characterized by large deflections of the drip shield crown and yielding of the bulkhead and plate components. The deflections and stresses experienced by the drip shield under static rockfall load conditions for the different rockfall rubble material property cases were similar up to the occurrence of buckling (i.e., locations of maximum stress). Therefore, unless noted otherwise, the figures that illustrate drip shield performance under static rockfall load conditions in the remainder of this section correspond to Case 4 (see Table 5-5).

5.2.1 Drip Shield Deflection

Figure 5-4 summarizes static rockfall load versus drip shield deflection for each of the rock rubble material property variations that were simulated. Figure 5-4 illustrates that the drip shield buckling load is reduced as the Young's modulus of the rockfall rubble accumulated on its sides is reduced. This result was to be expected because a stiffer material will provide more support for buttressing the drip shield. Figure 5-4 also shows the drip shield crown experiencing a positive, upward displacement for very low drip shield crown loads because of the lateral pressure from the rock rubble acting on the drip shield side walls.

Figure 5-5 illustrates the drip shield deforming and interacting with the accumulated rockfall material. In general, the drip shield side wall and rockfall rubble will begin to interact as the initial, smaller magnitude static rockfall loads are first applied to the drip shield. After contact is established, the side wall and support beam become column loaded. The bulkhead arch begins to flatten and push the side wall harder into the rockfall rubble. As the static rockfall load increases on the drip shield crown, the interaction load between the drip shield side wall and rock rubble intensifies until the drip shield structure buckles. Buckling primarily occurs in the support beam, which is generally column loaded.

For the extreme condition where there is no rock rubble interaction at the drip shield side wall (i.e., Case 1), the drip shield buckles under just a 23-tonne/m [15,460-lb/ft] static rockfall load. This result illustrates the importance of modeling the interaction of the drip shield side wall and the accumulated rockfall rubble. This particular analysis also demonstrates that the drip shield, as it is currently designed, is unable to protect the waste package from static rockfall loads without taking some credit for the extra structural support provided by the rockfall rubble. In addition, the maximum drip shield load capacity as predicted by the analyses presented here is considered to be overestimated because buckling of the drip shield is predicted under ideal load and symmetry assumptions (i.e., no load eccentricities and an artificially high drip shield structural stiffness created by the assumed planes of symmetry). This conclusion is further substantiated by the recognition that these analyses did not include the effects of prior damage to the carbon steel invert foundation and drip shield caused by dynamic rock block impacts, material creep, seismic activity, or corrosion over the long service life of the structure.

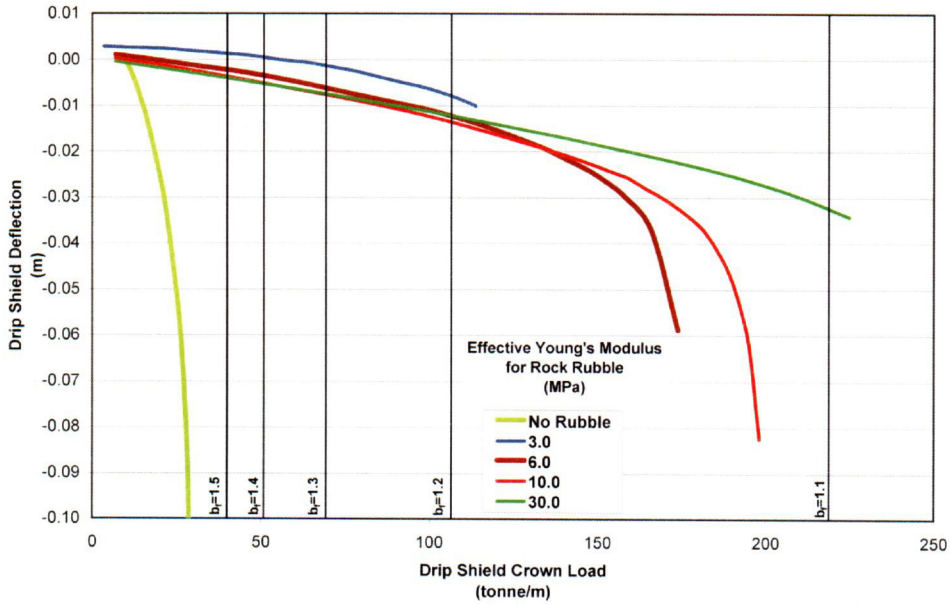

Figure 5-4. Drip Shield Deflection Versus Static Rockfall Load for Varying Rock Rubble Youngs' Moduli

5.2.2 Drip Shield Component Stresses

Bending moments are the primary source of stress in the drip shield components under static rockfall loads. The distributed pressure acting on the drip shield crown is transferred from the plate to the bulkhead which, in turn, transfers the load to the support beam. The bulkhead is loaded along its length (i.e., along the periphery of the drip shield crown) with a distributed pressure load and concentrated bending moments at its ends that are needed to satisfy static equilibrium requirements. The vertically oriented support beams ultimately carry the entire vertical rockfall load acting on the drip shield crown. The compressive load carried by the support beam, in conjunction with the concentrated bending moment acting at its top, ultimately leads to the buckling of the drip shield structure. Note that the concentrated bending moment acting at the top of the support beam is created by its connection with the bulkhead. As the static rockfall load is increased (Figures 5-6a through 5-6e), the bulkhead deflection pushes the side wall of the drip shield outward, by way of the bending moment acting at the top of the support beam, so that it comes into contact with the rockfall rubble. This interaction, in turn, will affect the magnitude and orientation of the bending moment between the bulkhead and the support beam. As illustrated in Figure 5-7, the deformation of the drip shield without accumulated rockfall interaction results in the side wall spreading out. The presence of the rockfall rubble prevents this spreading from occurring. The action and reaction cause the bending moment at the intersection of the bulkhead and support beam to change orientation.

C07

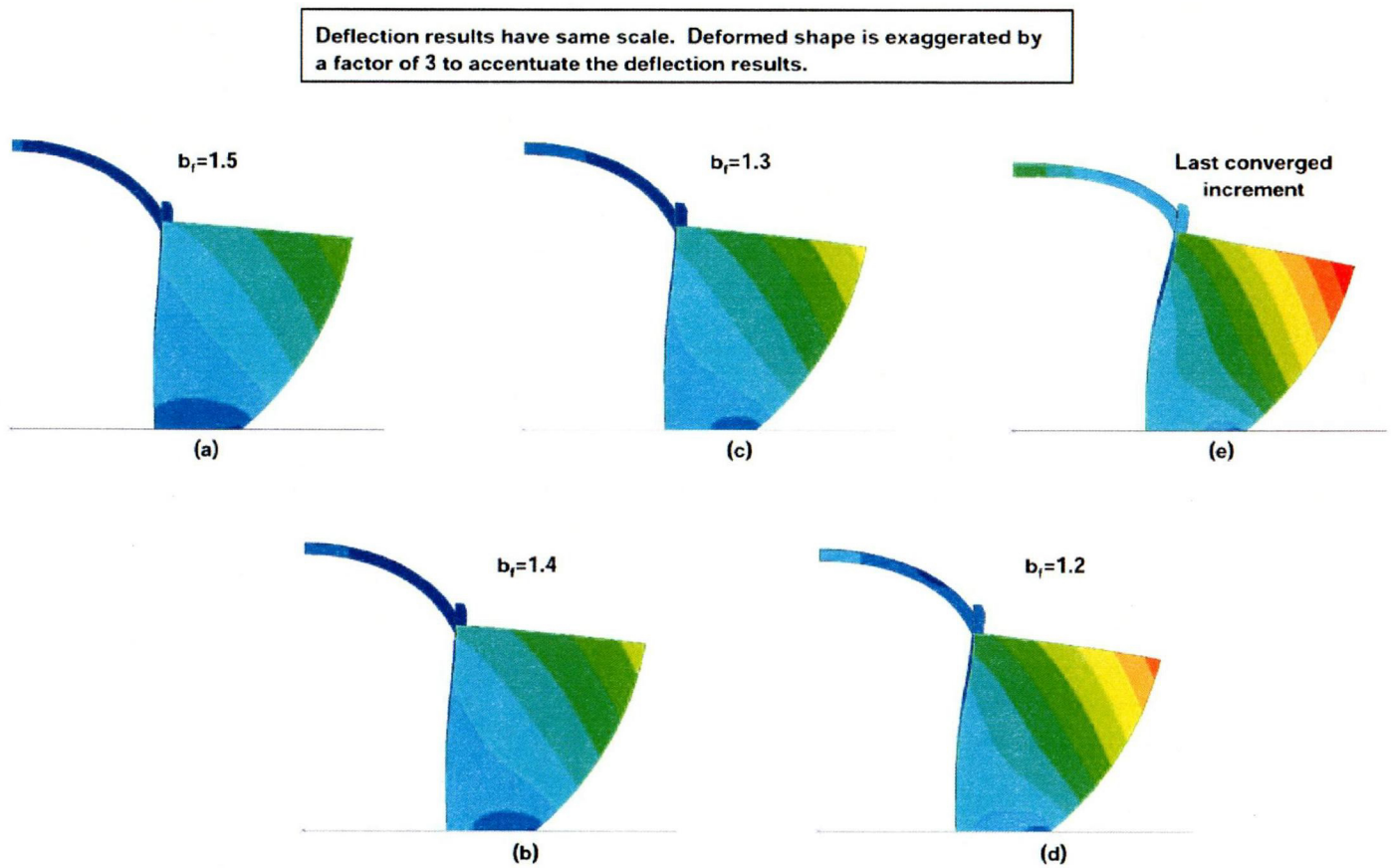

Figure 5-5. Drip Shield Deformation Under Static Rockfall Loads

C08

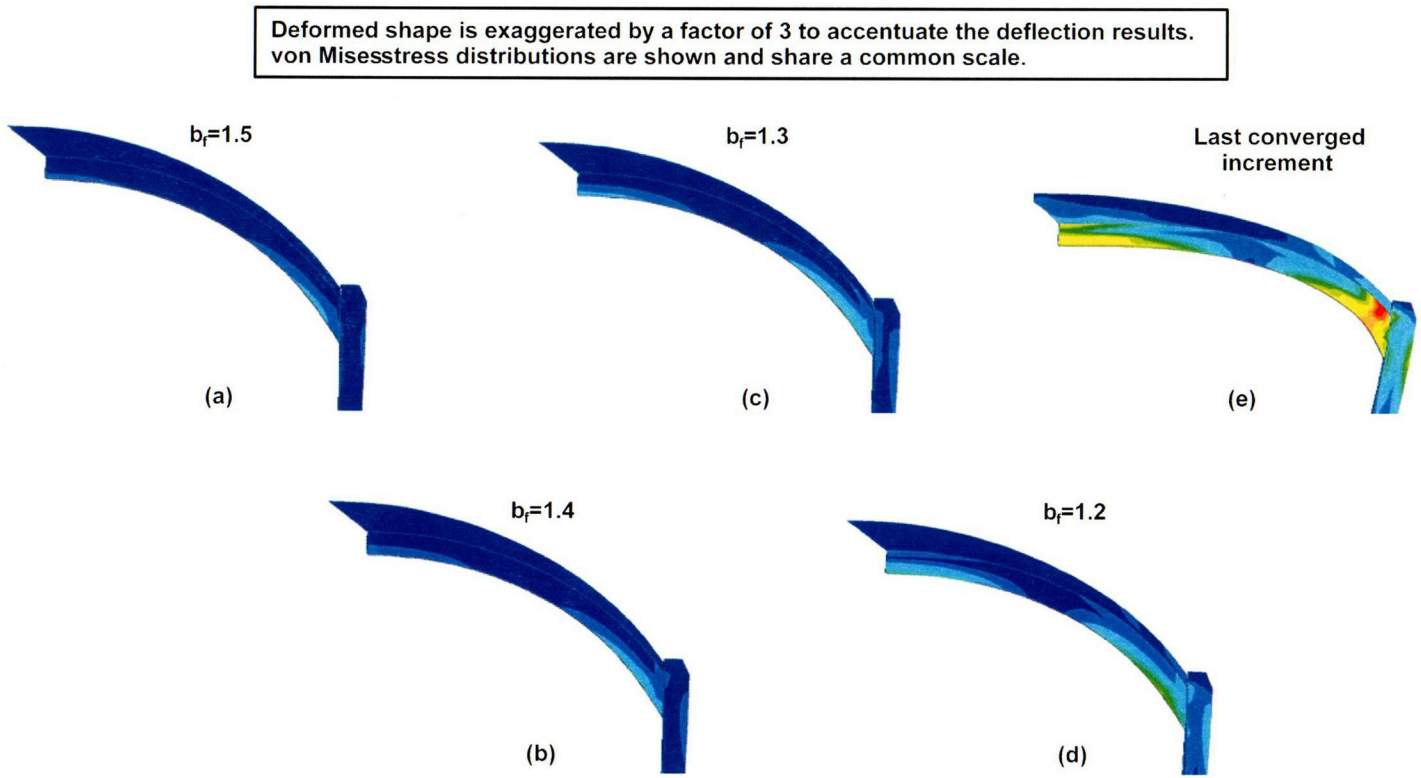

Figure 5-6. Bulkhead von Mises Stress Distribution and Deformation Corresponding to Maximum Static Rockfall Loads for Different Bulking Factors

C09

Deformed shape is exaggerated by a factor of 3 to accentuate the deflection results.
Von Mises stress distributions are shown and do not share a common scale.

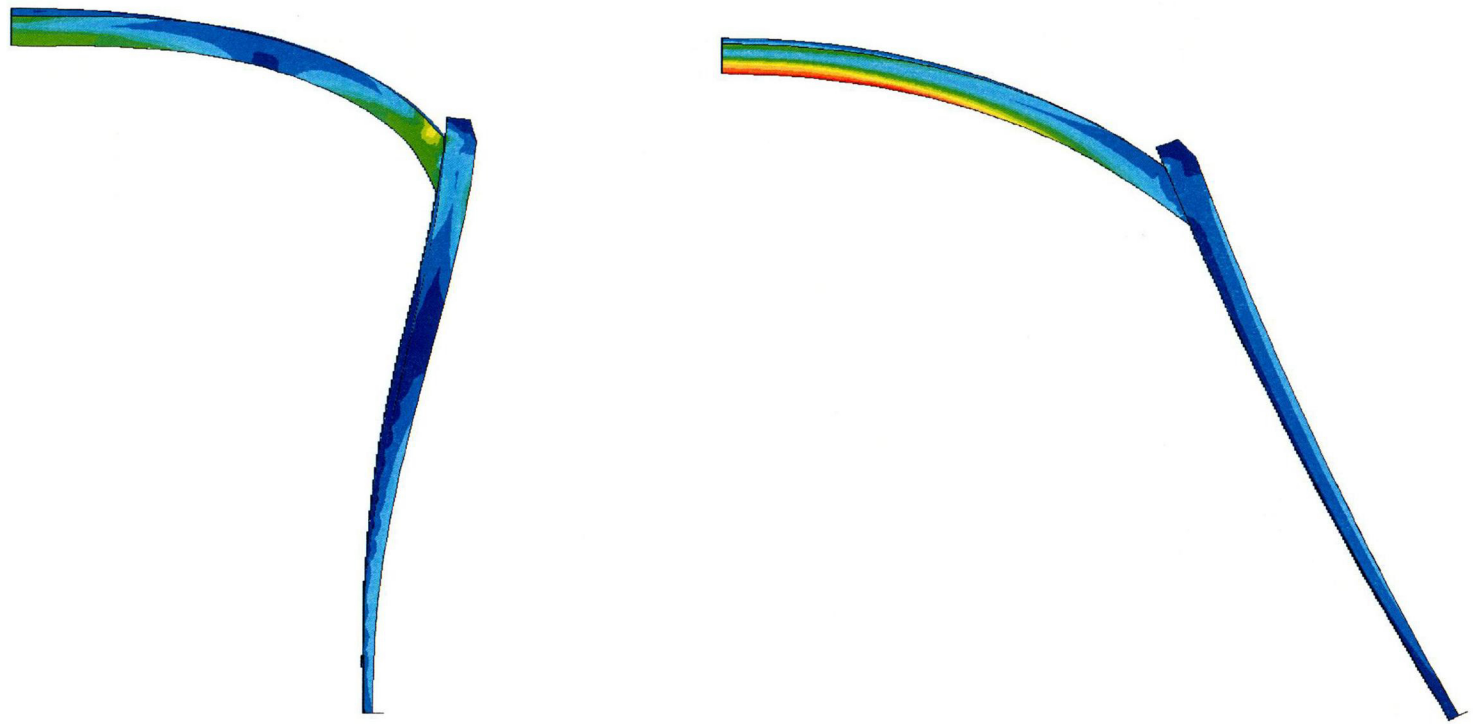

Drip Shield with Rockfall Rubble Interaction

(a)

Drip Shield without Rockfall Rubble Interaction

(b)

Figure 5-7. Comparison of Drip Shield Buckling Geometries With and Without Rock Rubble Lateral Support

C10

Stresses in the drip shield plates and bulkhead quickly reach magnitudes at or above the stress threshold for the initiation of creep. According to Neuberger, et al. (2002), Titanium Grades 7 and 24 can be expected to creep at stresses above 60 percent of their yield stress. Figures 5-8 through 5-12 show the maximum von Mises stress versus accumulated rockfall load for the drip shield bulkhead components for the five different rockfall rubble cases that were evaluated. These figures show that the rise in the maximum von Mises stress value is nearly a linear function of the rockfall load until the yield stress is reached. It is also interesting to note that the slope of the maximum von Mises stress versus rockfall load changes with the Young's modulus of the rockfall rubble. Table 5-6 conveys the vertical rockfall load acting on the drip shield crown that is likely to initiate creep in the drip shield plate and bulkhead. Creep in both the plate and bulkhead will occur earlier with softer Young's moduli for the rockfall rubble. Stress levels within the support beam do not approach the threshold stress needed to initiate creep until after buckling has occurred.

A post-buckling analysis of the drip shield was not performed. The post-buckled drip shield structure will exhibit extremely high plastic strains in the bulkhead to support beam transition region. Figures 5-8 through 5-12 illustrate that as the drip shield approaches its buckling load, the maximum stresses and plastic strains begin to rise dramatically. The post-buckling response is reasonably expected to continue this trend until the drip shield plate, bulkhead, or weld filler material fails.

In summary, the drip shield structure is not self supporting under static rockfall loads. The drip shield structure is likely to buckle under accumulated rockfall loads of approximately 25 tonne/m [16,800 lb/ft] unless assumptions are made about the drip shield side wall interaction with the rockfall rubble. As Figure 5-13 illustrates, the drip shield buckling load is reduced significantly as the effective Young's modulus for the rock rubble approaches expected values {i.e., 10 to 100 kPa [1.45 to 14.5 psi]}. The drip shield may not buckle if there are no static rockfall load eccentricities and the rock rubble behaves in a very stiff manner. The physical properties of the rockfall rubble are not known with a high degree of certainty, however, and taking excessive credit for its contribution to the structural stability of the drip shield would be premature at this time. Moreover, even if the drip shield does not buckle outright from supporting the potential static rockfall loads, the drip shield plate and bulkhead are still susceptible to creep failure.

5.3 Data Abstractions for MECHFAIL

5.3.1 Drip Shield Buckling Abstraction

Several factors were considered when constructing the drip shield buckling load distribution. First, because the accumulated rubble is not an engineered feature, the amount of potential side resistance from the rubble is highly uncertain. Second, the amount of side resistance is expected to vary widely along a typical drift; from areas with no appreciable side-rubble accumulation, for several conceivable reasons; to areas with relatively stiff side rubble. Third, even for the typical condition of full and reasonably uniform side-rubble accumulation, the compressibility of the rubble would vary widely because of varying amounts of previous compression. Although the rubble was assigned a uniform linear-elastic rheology in the finite element modeling, the actual behavior is anticipated to be nonlinear. It is the typical behavior of fragmented materials that some amount of compression is needed to mobilize the material resistance, such that the effective stiffness of the material increases with the amount of compression, starting from a very small value. As noted in Section 5.2.2, the staff estimated

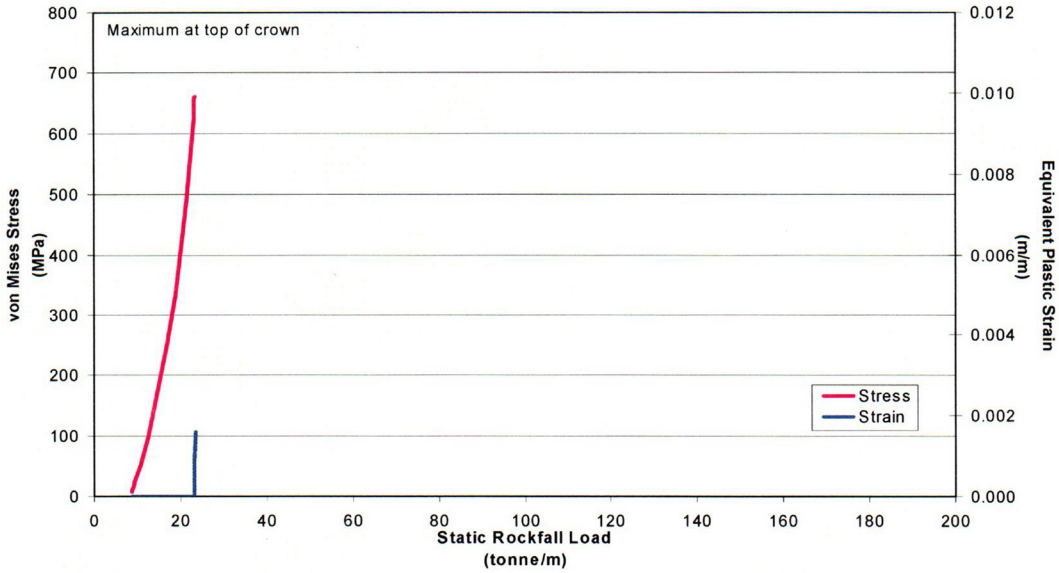

Figure 5-8. Maximum Bulkhead von Mises Stress and Equivalent Plastic Strain Versus Static Rockfall Load With No Accumulated Rockfall Rubble Lateral Support

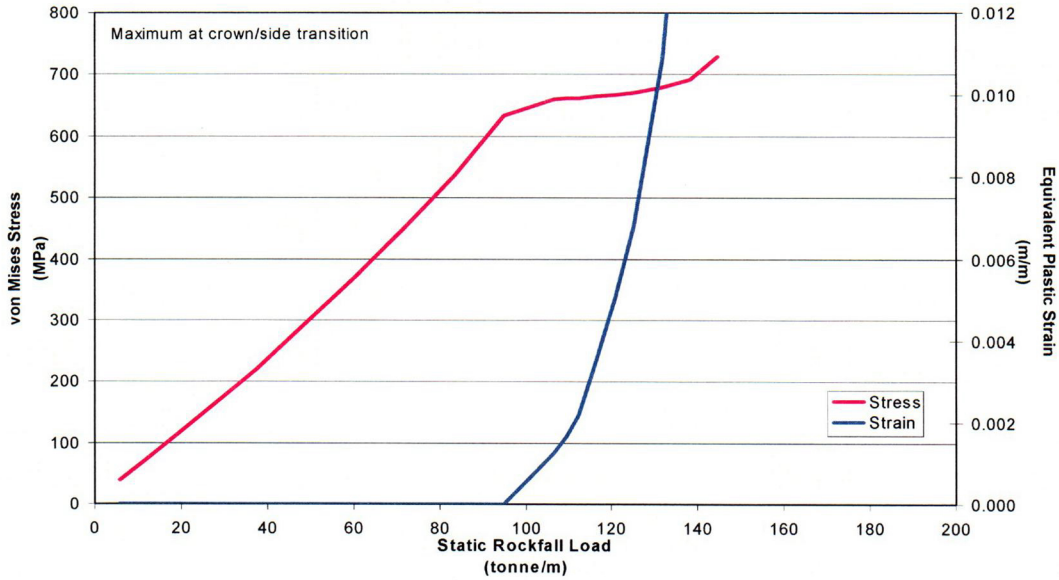

Figure 5-9. Maximum Bulkhead von Mises Stress and Equivalent Plastic Strain Versus Static Rockfall Load With Accumulated Rockfall Rubble Lateral Support {Effective Rock Rubble Young's Modulus = 3 MPa [4.35 × 10^2 psi]}

C11

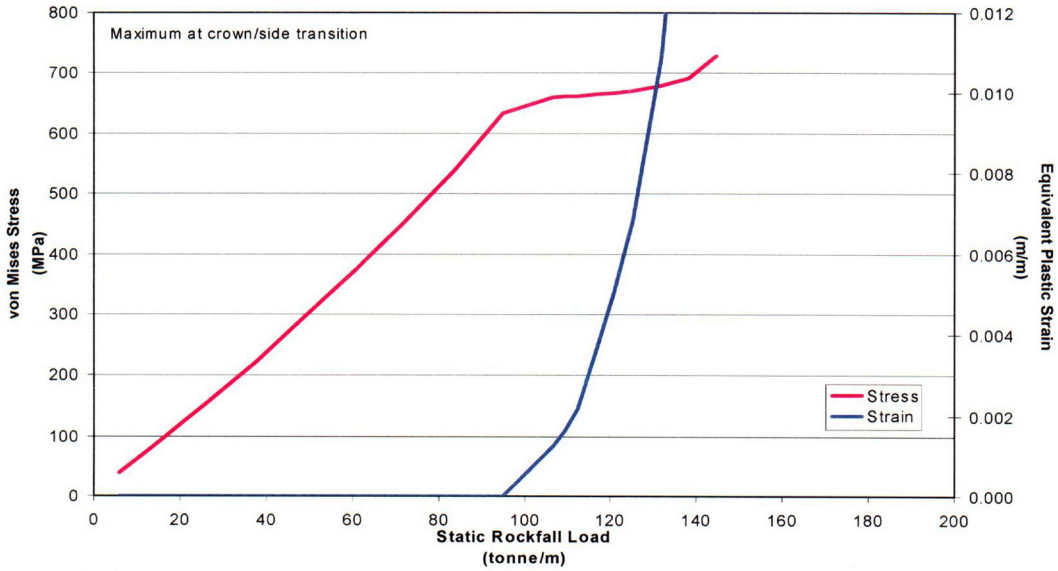

Figure 5-10. Maximum Bulkhead von Mises Stress and Equivalent Plastic Strain Versus Static Rockfall Load With Accumulated Rockfall Rubble Lateral Support {Effective Rock Rubble Young's Modulus = 6 MPa [8.70 × 10^2 psi]}

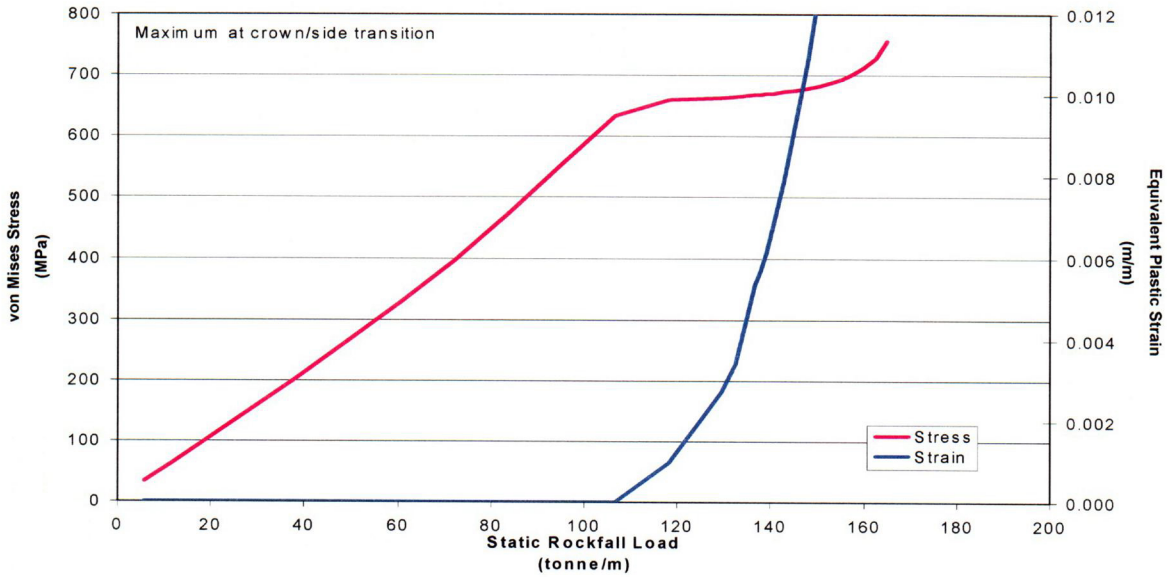

Figure 5-11. Maximum Bulkhead von Mises Stress and Equivalent Plastic Strain Versus Static Rockfall Load With Accumulated Rockfall Rubble Lateral Support {Effective Rock Rubble Young's Modulus = 10 MPa [1.45 × 10^3 psi]}

C12

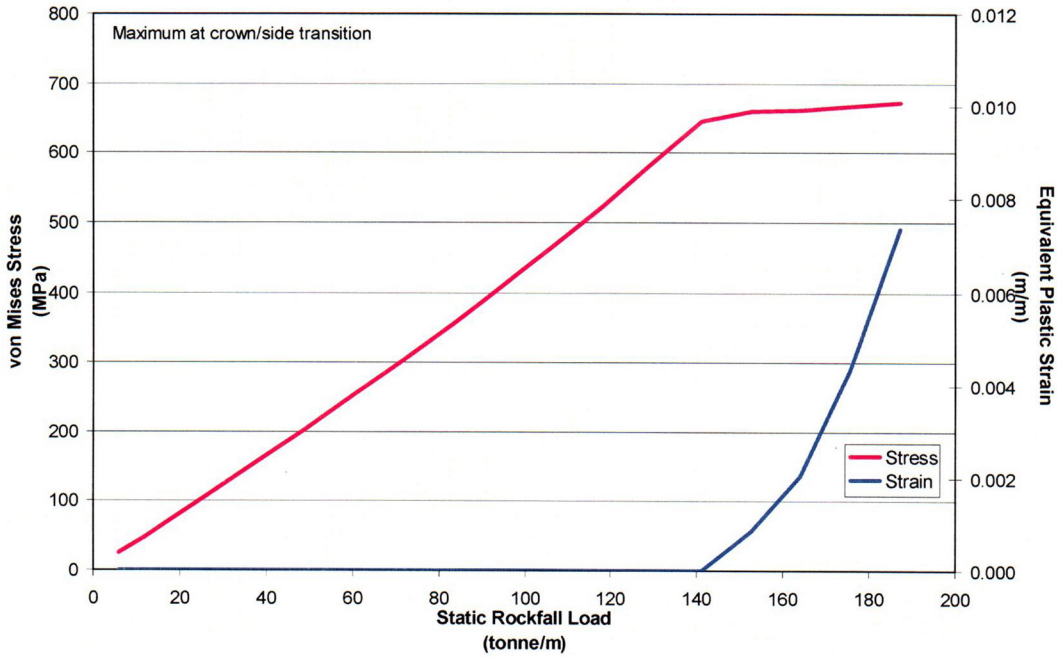

Figure 5-12. Maximum Bulkhead von Mises Stress and Equivalent Plastic Strain Versus Static Rockfall Load With Accumulated Rockfall Rubble Lateral Support {Effective Young's Modulus = 30 MPa [4.36 × 10^3 psi]}

Table 5-6. Total Static Rockfall Load Needed to Initiate Creep for Varying Rock Rubble Young's Moduli

Simulation	Rock Rubble Young's Modulus, MPa [psi]	Load at 60 Percent Plate Yield, tonne/m [lb/ft]	Load at 60 Percent Bulkhead Yield, tonne/m [lb/ft]	Drip Shield Buckling Load, tonne/m [lb/ft]
1	no rock	15 [10,080]	20 [13,440]	23 [15,460]
2	3.0 [4.35 × 10^2]	48 [32,270]	54 [36,300]	95 [63,860]
3	6.0 [8.70 × 10^2]	51 [34,280]	64 [43,020]	138 [92,760]
4	10.0 [1.45 × 10^3]	54 [36,300]	72 [48,400]	157 [105,540]
5	30.0 [4.36 × 10^3]	64 [43,020]	92 [61,840]	187 [125,700]

C13

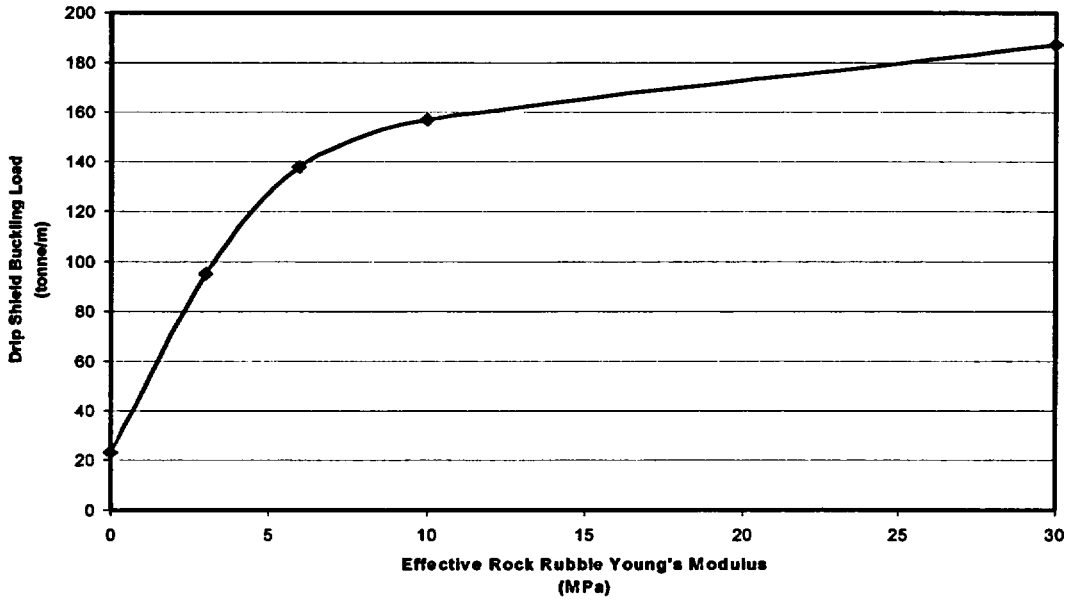

Figure 5-13. Drip Shield Buckling Load Versus Effective Rock Rubble Young's Modulus

that the effective Young's moduli for the rock rubble should be within the range of 10 to 100 kPa [1.45 to 14.5 psi]. Fourth, the assumed symmetric load and boundary conditions applied in the process level finite element model inherently preclude lateral (i.e., horizontal) deflections of the drip shield crown apex, artificially suppressing the lateral buckling made of the drip shield. Fifth, as the carbon steel invert frame corrodes, the foundation of the drip shield is increasingly compromised. Degradation of the drip shield foundation is expected to adversely affect its load-bearing capacity. Sixth, the adverse affects that can potentially be created by corrosion of the drip shield materials have not been explicitly accounted for in the process-level models. Based on the foregoing considerations, the drip shield buckling load beta distribution (see Figure 5-14) was assigned a range from 25 tonne/m [16,800 lb/ft], which corresponds to a negligible side support from rubble; to 150 tonne/m [100,800 lb/ft], which corresponds to an accumulated rubble with an effective stiffness of approximately 10 MPa [1,440 psi]. The drip shield buckling load beta distribution also has the characteristic that no more than 20 percent of the drip shields will have a buckling load threshold greater than 60 tonne/m [40,330 lb/ft]. The drip shield buckling load distribution curve is used during the initialization phase of the MECHFAIL module to assign a drip shield buckling load to each spatial grid element.

The effects of a seismic event on the effective static rockfall load acting on the drip shield is accounted for by Eq. (5-2). This adjustment is a first approximation of the potential effect that seismic activity will have on the effective static rockfall load. It is important to recognize that this adjustment does not consider dynamic amplification effects that would occur if the natural frequencies of the rock rubble mass were excited during the seismic event. In addition, it should be noted that the peak horizontal ground acceleration is used in Eq. (5-2) to adjust the

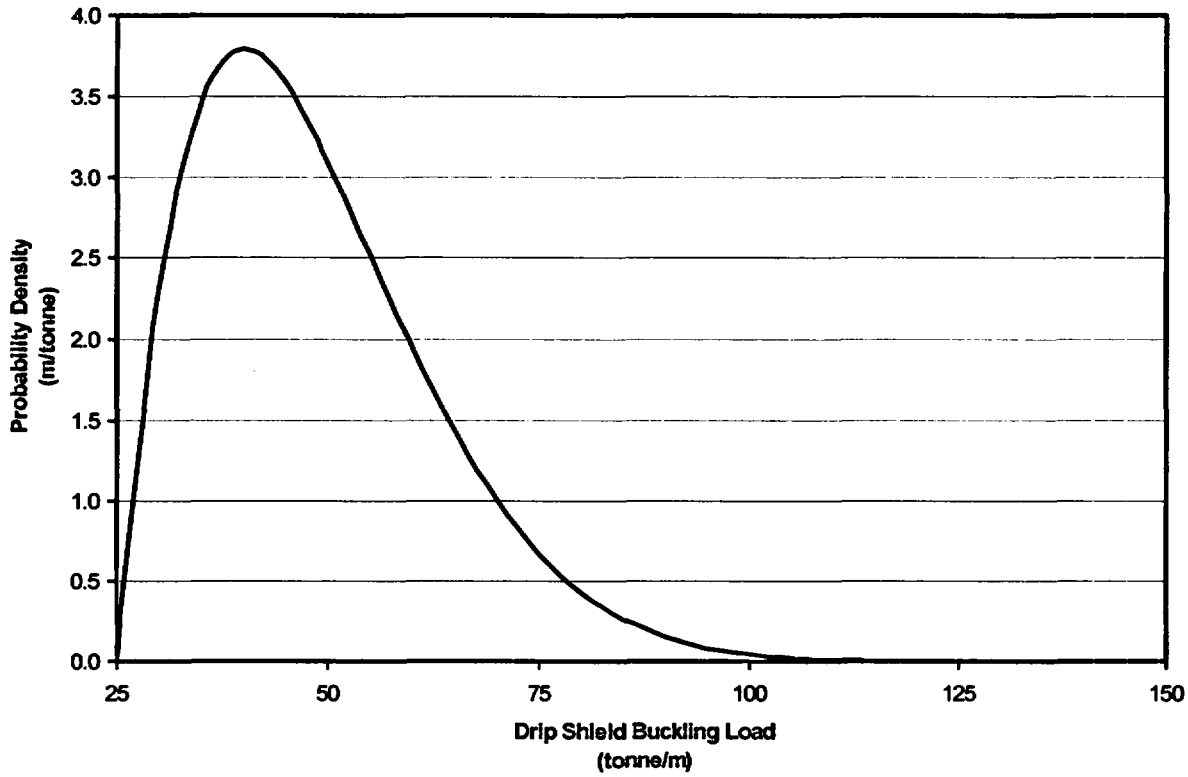

Figure 5-14. Beta Distribution Defining the Drip Shield Buckling Load

static rockfall load. It would be more appropriate to use the peak vertical ground acceleration for this purpose. Future revisions of the MECHFAIL module will utilize the peak vertical ground acceleration for adjusting the static rockfall load.

$$L_{\text{adj.static}} = (1 + \text{pga})\, L_{\text{static}} \tag{5-2}$$

where

$L_{\text{adj. static}}$	—	static rockfall load adjusted to account for the effects of a seismic event (tonne/m)
L_{static}	—	static rockfall load (tonne/m)
pga	—	mean peak horizontal ground acceleration (g)

5.3.2 Drip Shield Component Stress Abstraction

The following discussion conveys the approach taken to create the functions relating static rockfall load to the maximum von Mises stress magnitude for the drip shield plate and bulkhead. These stresses are then used to calculate the magnitude of plastic strain in these components attributable to creep using the results of Neuberger, et al. (2002). Recall that the stress levels within the support beams are not sufficient to initiate creep.

Table 5-6 clearly shows that the maximum von Mises stress generated within the drip shield plate and bulkhead is strongly dependent on the Young's modulus assumed for the rock rubble. In addition, Table 5-6 also suggests a correlation between the drip shield buckling load and the maximum von Mises stress within the drip shield plate and bulkhead components. Because the drip shield buckling load is assigned to each spatial grid element using a beta distribution curve as described in Section 5.3.1, the static rockfall load required to generate stresses within the drip shield plate and bulkheads that satisfy the initiation of creep stress threshold is abstracted in terms of the assigned drip shield buckling load. Specifically,

$$L_{plate} = \left[4.903 \times 10^{0}\right] + \left[5.120 \times 10^{-1}\right] L_{buckling} - \left[1.130 \times 10^{-3}\right] L^{2}_{buckling} \tag{5-3}$$

$$L_{bulkhead} = \left[1.277 \times 10^{1}\right] + \left[3.572 \times 10^{-1}\right] L_{buckling} + \left[2.703 \times 10^{-4}\right] L^{2}_{buckling} \tag{5-4}$$

where

L_{plate}	—	static rockfall load (tonne/m) needed to initiate creep in the drip shield plate
$L_{bulkhead}$	—	static rockfall load (tonne/m) needed to initiate creep in the drip shield bulkhead
$L_{buckling}$	—	drip shield buckling load (tonne/m)

The normalized error for Eqs. (5-3) and (5-4) were calculated using the following relationship

$$L^{err} = \frac{\sum_i \left[L_i - L\left(L_{buckling,i}\right)\right]^2}{\sum_i \left[L_i\right]^2} \tag{5-5}$$

Using Eq. (5-5), the normalized error for Eqs. (5-3) and (5-4) were determined to be

$$L^{err}_{plate} = 4.29 \times 10^{-3} \tag{5-6}$$

and

$$L^{err}_{bulkhead} = 2.68 \times 10^{-3} \tag{5-7}$$

6 DRIP SHIELD AND WASTE PACKAGE INTERACTION CAUSED BY ACCUMULATED ROCKFALL STATIC LOADS PERFORMANCE ANALYSES

The analysis results presented in Chapter 5 demonstrated the propensity of the drip shield to buckle when subjected to accumulated static rockfall loads. As a result of this buckling, the static rockfall loads acting on the exterior of the drip shield will be transmitted to the waste package by way of the drip shield bulkheads. Because of the relatively small contact area between the waste package and drip shield bulkheads, at least initially, and the magnitudes of the static rockfall loads, the waste package outer barrier is expected to experience very large plastic strains. The rationale for this expectation is provided in the following discussion.

The planned thickness of the drip shield bulkhead is 0.038 m [0.125 ft] (CRWMS M&O, 2000a, Reference Sketch Number SK–0148, Revision 05). Assuming the arc length of the bulkhead initially in contact with the waste package outer barrier is 0.020 m [0.066 ft], the contact area between the bulkhead and waste package is 7.6×10^{-4} m^2 [8.2×10^{-3} ft^2]. Recalling the accumulated static rockfall load acting on the drip shield will lie somewhere in the range of 40 to 160 tonne/m [26,890 to 107,550 lb/ft] (see Figure 4-5) and recognizing that the spacing between adjacent drip shield bulkheads is approximately 1 m [3.28 ft], the resultant load transmitted to the waste package by each bulkhead will be at least 40 tonne [26,890 lb] and no more than 160 tonne [107,550 lb]. The average stress acting over the assumed contact area between the waste package and bulkhead will exceed the ultimate tensile strength of Alloy 22 {984.7 MPa [1.43×10^5 psi]}, the waste package outer barrier material, for a 76.3-tonne/m [51,290-lb/ft] static rockfall load. In the context of the material failure criterion defined in the ASME International (2001) Boiler and Pressure Vessel Code for Service Level D conditions, which is 90 percent of the material ultimate tensile strength, the static rockfall load that can be considered to breach the waste package outer barrier is reduced to 68.7 tonne/m [46,180 lb/ft]. The static rockfall load needed to yield {i.e., exceed the 254.7 MPa [3.69×10^4 psi] Alloy 22 yield stress} the waste package outer barrier is 19.8 tonne/m [13,310 lb/ft].

In addition to the concern pertaining to the contact stress created between the waste package and drip shield bulkhead is the contact stress between the waste package and its supporting pallet. The contact stress between the waste package and supporting pallet is also a concern because this interaction could also generate localized contact stresses that exceed the allowable material limits of Alloy 22.

There are two important factors that have not been adequately considered in the foregoing simplified, qualitative waste package and drip shield interaction analysis. First, as has been demonstrated, the initial contact stresses between the waste package and drip shield bulkheads and waste package and pallet are clearly sufficient to generate large plastic deformations of Alloy 22. As a result, the initial contact area that has been estimated here can be expected to increase significantly as the outer barrier deforms under the applied load. This increase in contact area will, in turn, reduce the average contact stress acting on the waste package outer barrier and, at some point, the deformed system will reach an equilibrium point. The critical question that needs to be answered is how much plastic strain must be incurred by the waste package outer barrier before this equilibrium point is reached. Alloy 22 is a relatively unique material because its minimum allowable elongation at failure, as defined by ASTM International (1998), is 45 percent. Most metals used for structural applications do not exhibit this much material ductility prior to failure. The log normal failure strain equivalent for Alloy 22 is 36.7 percent (Gute, et al., 2001).

Even though the high ductility of Alloy 22 may reduce the potential for a waste package breach because of interactions with the drip shield and pallet under static rockfall loads, the second factor that has not been accounted for in the simplified, qualitative analysis presented earlier is the contribution of bending moments to the stress state of the Alloy 22 in the various contact regions. These bending moments can be attributed to the overall structural response of the waste package consistent with classic engineering beam theory and localized bending moments created by localized deformations in the immediate areas of the various contact interactions. The localized bending moments will become more significant as the radial gap between the inner and outer barriers of the waste package increases as the waste package temperature decreases.

Additional observations regarding the potential interaction between the waste package and drip shield include the following. First, it is not certain the base of the bulkhead or the waste package itself will be oriented in a manner consistent with the assumption that the contact stress will be uniformly distributed over the bulkhead surface. The initial contact between the waste package and bulkhead may occur primarily along the edge of the bulkhead, more consistent with a line load than a distributed load. Second, even though the Young's modulus for the Alloy 22 waste package outer barrier is approximately twice that of the Titanium Grade 24 bulkhead (see Table 5-2), the yield stress of the bulkhead {658.1 MPa [9.54×10^4 psi]} is substantially greater than the yield stress of the Alloy 22 waste package outer barrier {254.7 MPa [3.69×10^4 psi]}. As a result, the waste package outer barrier will yield much earlier than the drip shield bulkhead. After yielding, the stiffness of Alloy 22 is governed by its tangent modulus that, assuming a bilinear stress-strain curve, is approximately 2 GPa [2.9×10^5 psi], which is significantly smaller than the 107.2 GPa [15.5×10^6 psi] Young's modulus of Titanium Grade 24 that is still responding to the load in a linear elastic manner. Therefore, the bulkhead can be considered to be a rigid body from the perspective of the waste package outer barrier. Third, the outer barrier is not attached to the inner barrier in any way. Consequently, the inner barrier acts as an anvil that the outer barrier can be cold worked against. The inner barrier protects the spent nuclear fuel or high-level waste within its confines from the effects of rockfall loads, both static and dynamic. If the outer barrier is breached, however, the level of protection of the waste package contents provided by the inner barrier is not clear because of the uncertainty associated with the quantity and chemistry of water that could infiltrate the breach and the subsequent affect of the water on the corrosion rate of the inner barrier.

Recall that the effects of a seismic event on the effective static rockfall load acting on the drip shield is accounted for in Eq. (5-2). This adjustment to the static rockfall load enables a proper accounting of those drip shields that are likely to buckle during a seismic event. After the drip shield has buckled, however, the same increase in the effective load must be considered when assessing the potential damage to the waste package. Assuming a static rockfall load of 76.3 tonne/m [51,290 lb/ft] is sufficient to breach the waste package by way of a buckled drip shield (as derived earlier), a peak ground acceleration of 0.91 g would increase a 40-tonne/m [26,890-lb/ft] static rockfall load to a magnitude capable of breaching the waste package under seismic conditions. As was pointed out in Section 5.3.1, the Total-system Performance Assessment code characterizes the magnitude of a seismic event only in terms of the peak horizontal ground acceleration, which is used in Eq. (5-2) to adjust the static rockfall load. It would be more appropriate, however, to use the peak vertical ground acceleration for this purpose. Furthermore, it was shown in Chapter 4 that 40 tonne/m [26,890 lb/ft] is the minimum static rockfall load that the drip shield is anticipated to have to support, and these loads will

have fully manifested themselves within 1,000 years after cessation of maintenance of the ground support system.

To investigate the foregoing concerns, a finite element model of the waste package and drip shield that can be used to assess the effects of different interaction orientations under static rockfall loads is being developed. This model will also include the waste package pallet support. Although this model has yet to be completed, Section 6.1 presents a brief description of the current approach being taken to construct the model.

6.1 Finite Element Model Description

Sections 6.1.1–6.1.3 convey the rationale and technical bases for the various boundary conditions implemented in the construction of the finite element model used to approximate the waste package and drip shield interaction under static rockfall loads.

6.1.1 Finite Element Model Geometry

The finite element model of the waste package and drip shield interaction under static rockfall loads consists of six distinct components: the fuel assemblies, basket, inner barrier, outer barrier, waste package pallet, and drip shield bulkhead. Figure 6-1 shows the layout of these components described in detail in the following discussion. The entire assembly is assumed to be under a vertical load from the drip shield bulkheads. The model geometry has been simplified by using symmetry conditions for both the load and geometry about the vertical plane that intersects the waste package centerline (as shown in Figure 6-1). All features and dimensions are based on documented engineering drawings (CRWMS M&O, 2000a, Reference Sketch Numbers SK–0175, Revision 02; and SK–0191, Revision 00). The model is being constructed using a mixture of plate and solid elements. Plate elements (three-dimensional quadrilaterals) are used for the basket structure. Solid elements (three-dimensional hexahedrons) are used to represent all other structural members (see Figures 6-2 through 6-5).

An effort has been made to minimize the number of nodes and elements used to discretize the model, but the level of modeling detail required to capture the contributions of geometric stress concentration factors in critical areas (e.g., the closure lid weld region) cannot be avoided if reliable results in these regions are desired. The fuel assemblies and basket are simplified to a relatively coarse mesh that provides a good representation of the mass and stiffness of these structures. The inner and outer barriers are similarly simplified only in regions away from areas of concern. Much of the cylindrical sections of the inner and outer barriers are modeled with one element through the thickness. These elements use an incompatible mode formulation that makes them accurate in modeling bending where a standard solid element would not be accurate unless three or more well-shaped elements were used through the thickness. The cylindrical sections with the incompatible mode elements are effectively glued to the fine meshed regions of the outer barrier closure lids using a tied contact surface interaction. The outer barrier regions in contact with the pallets and bulkhead are also finely meshed to provide satisfactory contact and stress results.

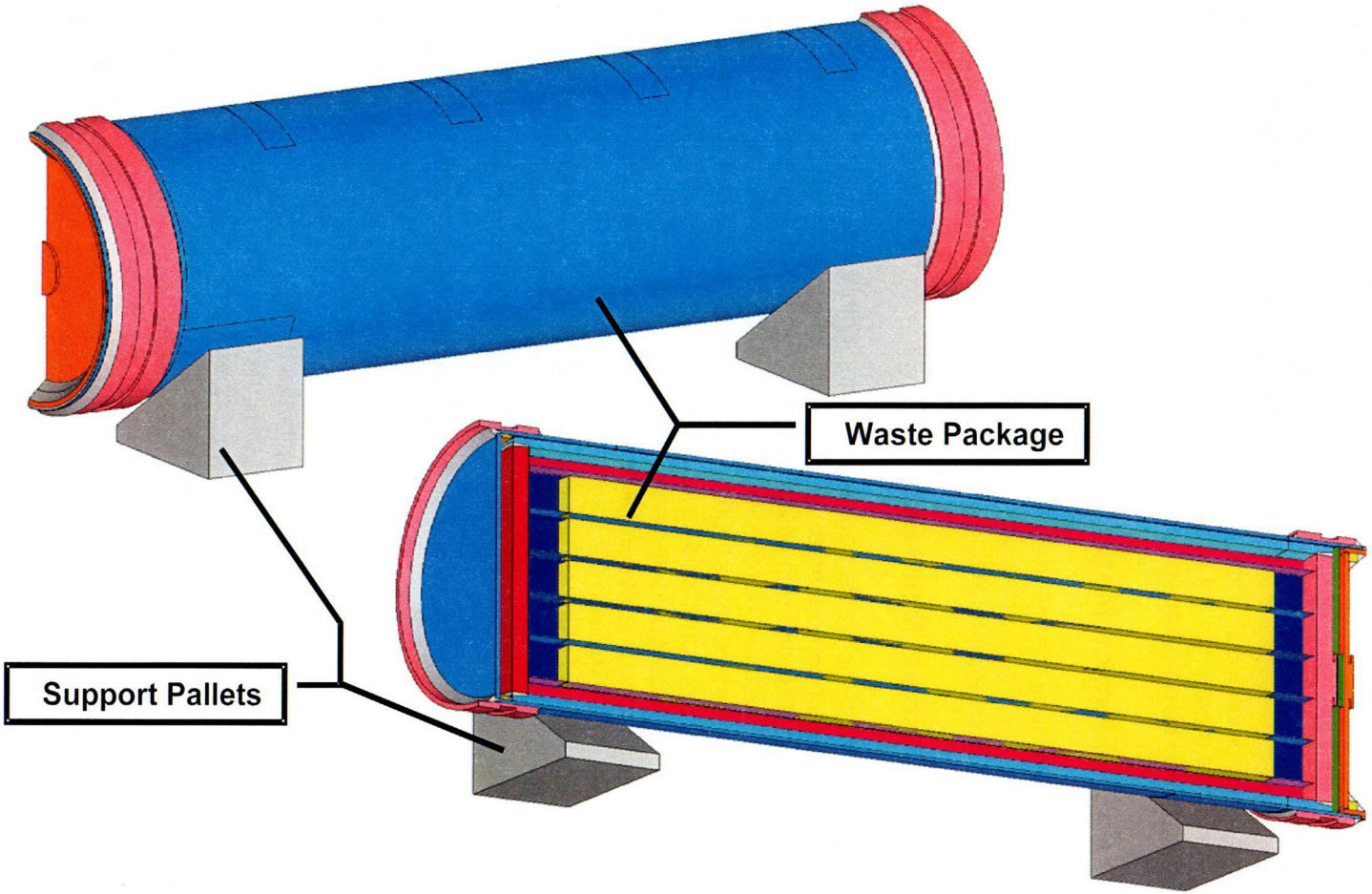

Figure 6-1. Waste Package and Drip Shield Static Rockfall Load Interaction Model

C14

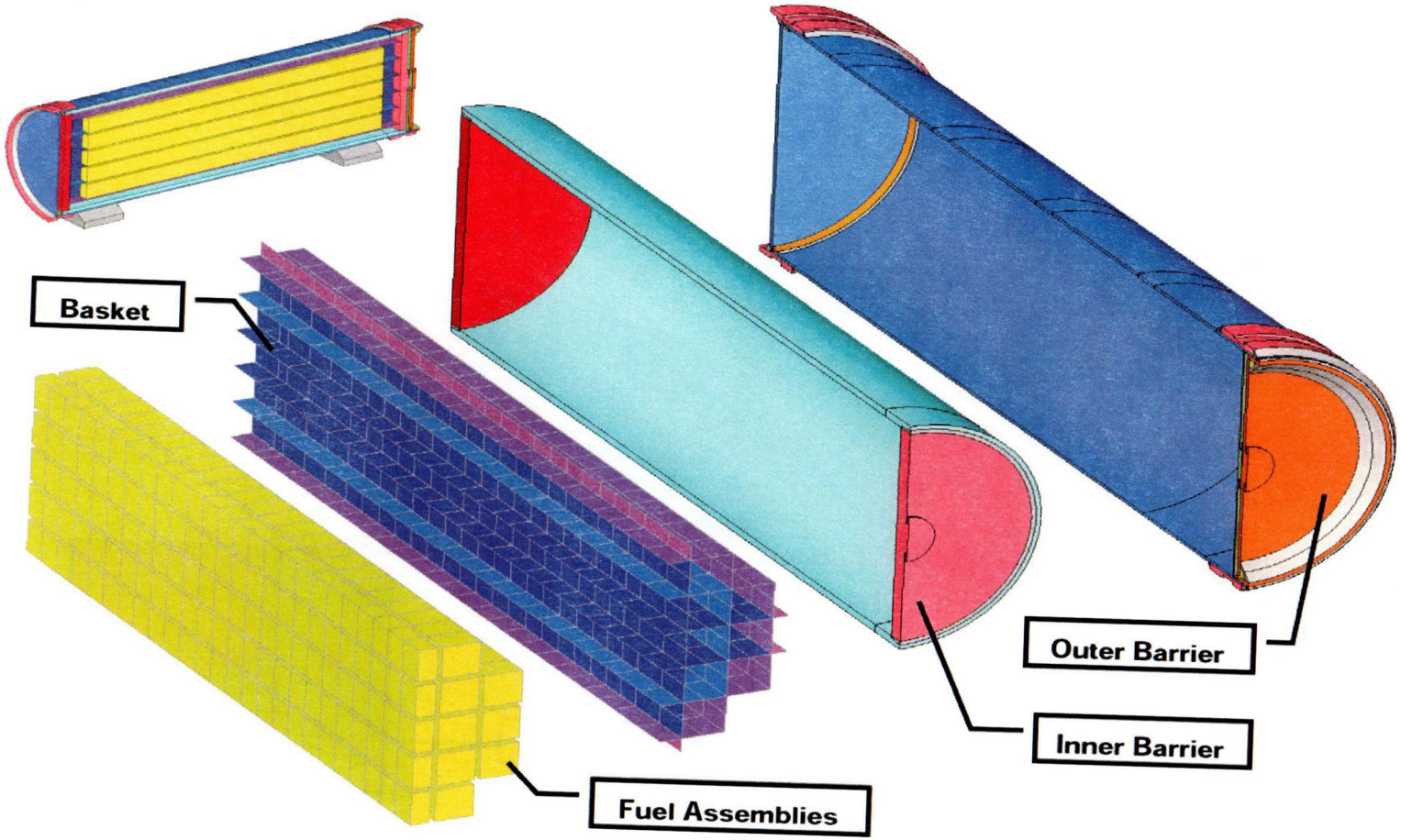

Figure 6-2. Waste Package Model Components

C15

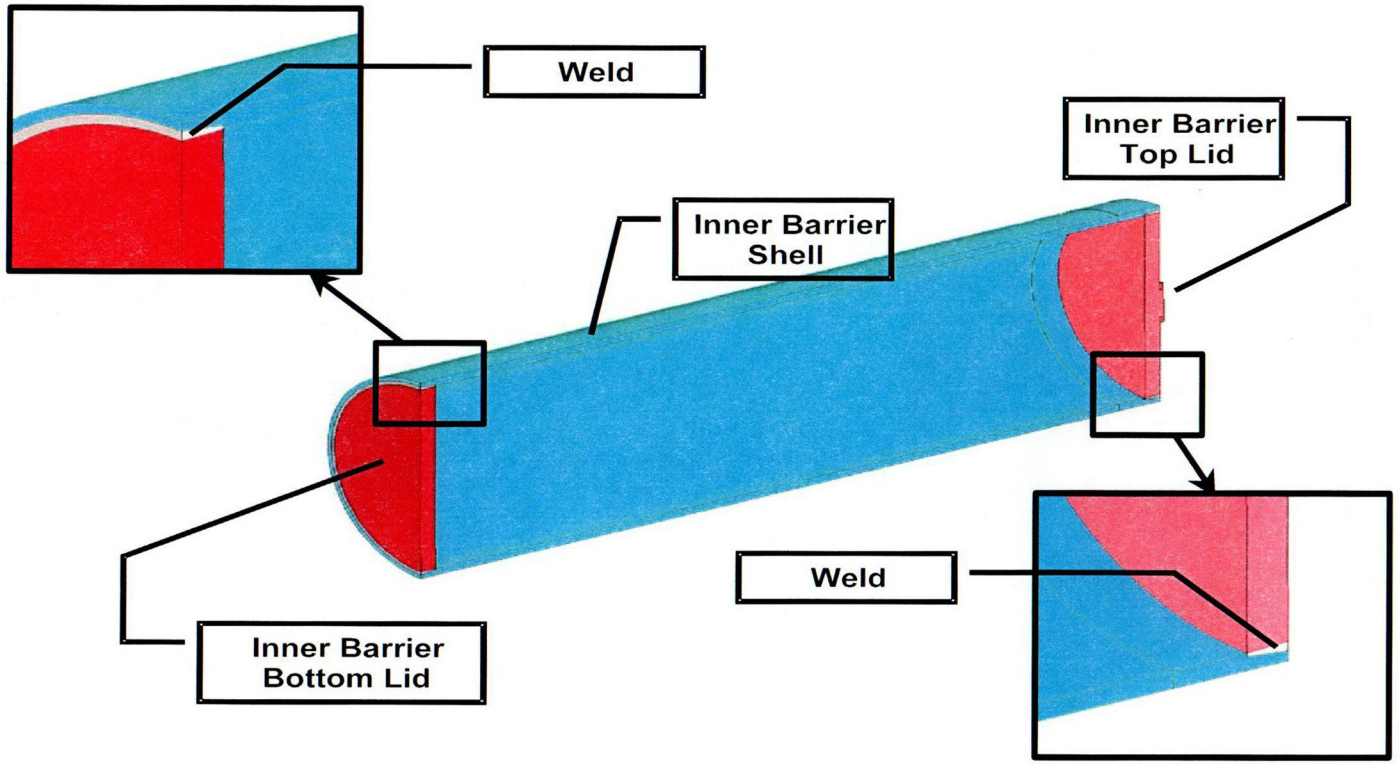

Figure 6-3. Waste Package Inner Barrier Components

C16

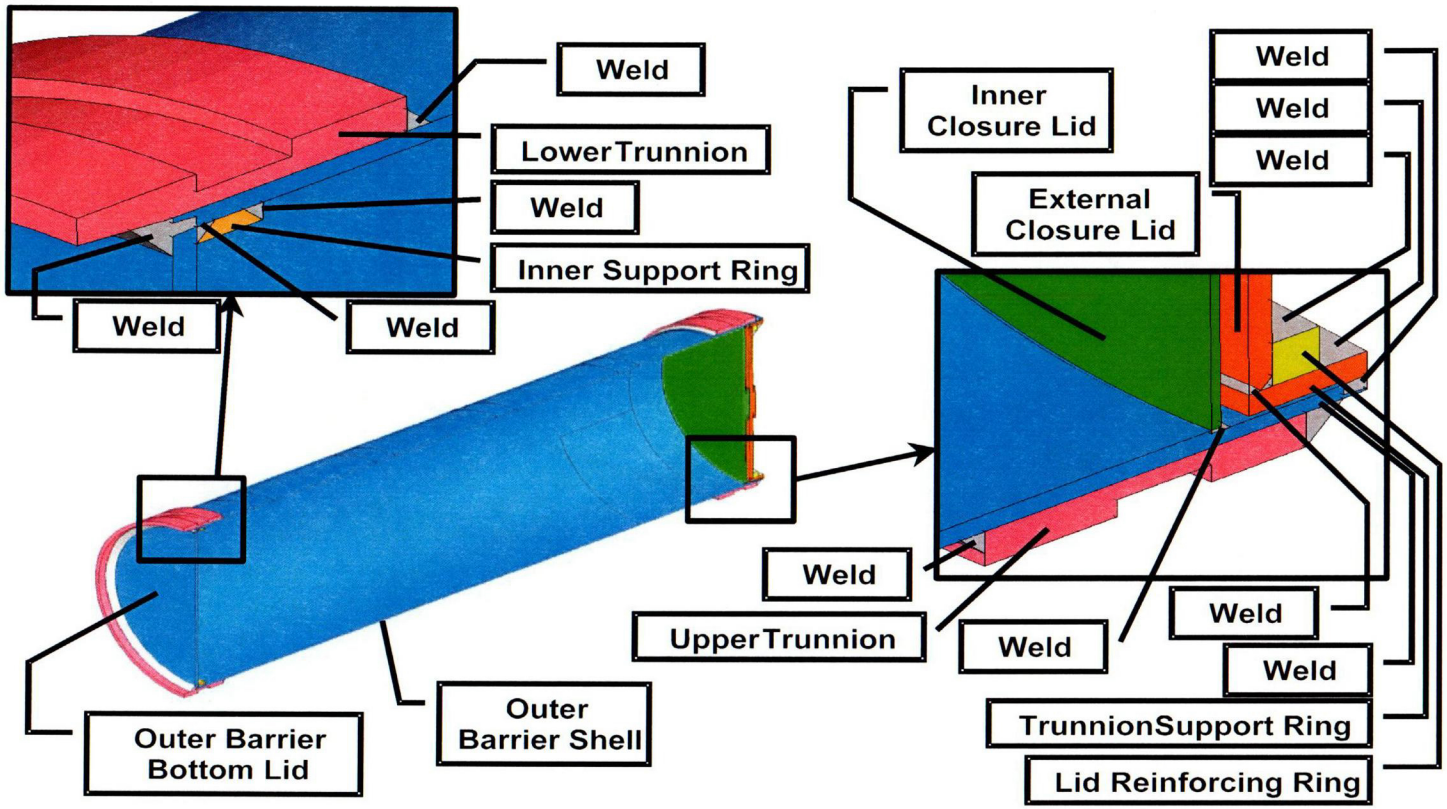

Figure 6-4. Waste Package Outer Barrier Components

C17

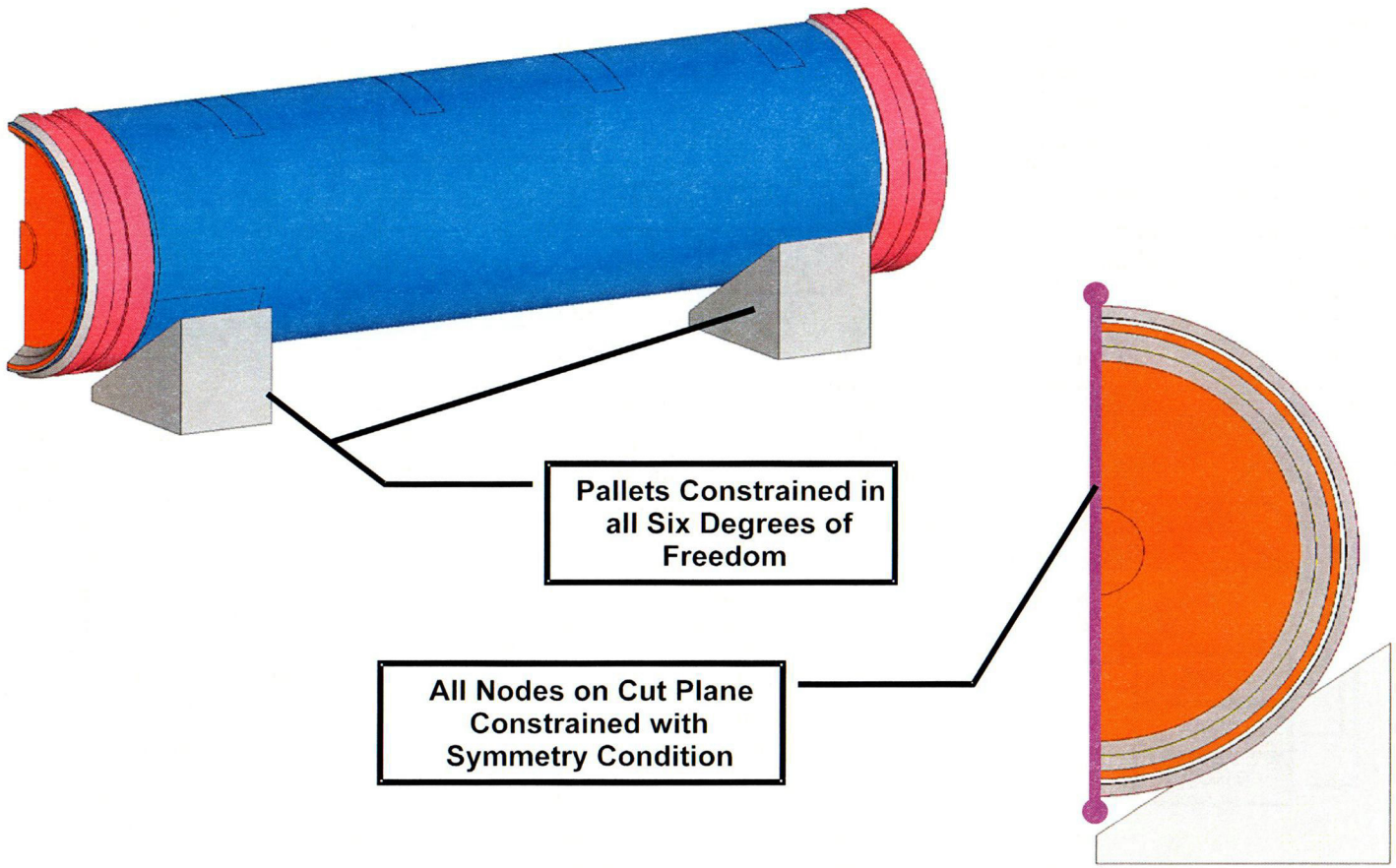

Figure 6-5. Waste Package and Drip Shield Interaction Model Boundary Conditions

C18

6.1.2 Finite Element Model Boundary Conditions

6.1.2.1 Loads

The only loads acting on the waste package are gravity and the static rockfall loads transferred through the drip shield bulkheads. The vertically oriented static rockfall loads are applied to the reference nodes of the rigid surfaces that represent the five drip shield bulkheads in contact with the waste package.

6.1.2.2 Kinematic Constraints

Each of the six waste package and drip shield interaction model components are free to translate and interact in reaction to the simulated load conditions. A single plane of symmetry is the only major model simplification. Each component of the model interacts with its neighbor through contact surface interaction definitions.

The outer barrier rests on the pallet with localized contact pairs defined for each "V"-notch member of the pallet. Both the pallet and waste package are modeled as deformable bodies. The model also includes five bulkheads in contact with the waste package, each evenly spaced approximately 1 m [3.28 ft] apart along the length of the waste package. The bulkhead surfaces are modeled as rigid bodies. As was pointed out previously, the yield stress of the Titanium Grade 24 bulkhead is substantially greater than the yield stress of Alloy 22, and the cross section of the bulkhead has a relatively high area moment of inertia (i.e., the bulkhead has a relatively high geometric bending stiffness). Although a post-buckling analysis of the drip shield under accumulated static rockfall conditions was not performed, the bulkhead is not expected to sustain significant distortions of its basic shape (recall that buckling of the drip shield is controlled primarily by the column loading of the support beam). Therefore, the bulkhead has been modeled using the same geometric dimensions that it had prior to loading.

The inner surface of the outer barrier can interact with the outer surface of the inner barrier along the entire length of the waste package. These surfaces are modeled using standard contact definitions for two deformable bodies.

The basket is spot welded to the inner surface of the inner barrier. The finite element model simply ties the coarse basket mesh to the inner barrier elements by equivalencing the nodes of the two components that are collocated (see Figure 6-2).

Each of the fuel assemblies has three contact interaction definitions with the basket (i.e., the bottom and sides of each basket cell). These surface interactions are modeled using standard contact definitions for two deformable bodies.

Finally, tied contacts are used at several locations to provide a transition between regions of coarse and fine mesh discretizations.

6.2 Summary of Analysis Results

This work has yet to be completed.

6.3 Data Abstraction for MECHFAIL

This work has yet to be completed.